Cloudy with a Chance of Water:
Investigating hot Jupiter exoplanet atmospheres through observation and analysis

A thesis submitted by
Hannah Ruth Wakeford
to The University of Exeter

for the degree of Doctor of Philosophy
in the subject of Physics
March 2015

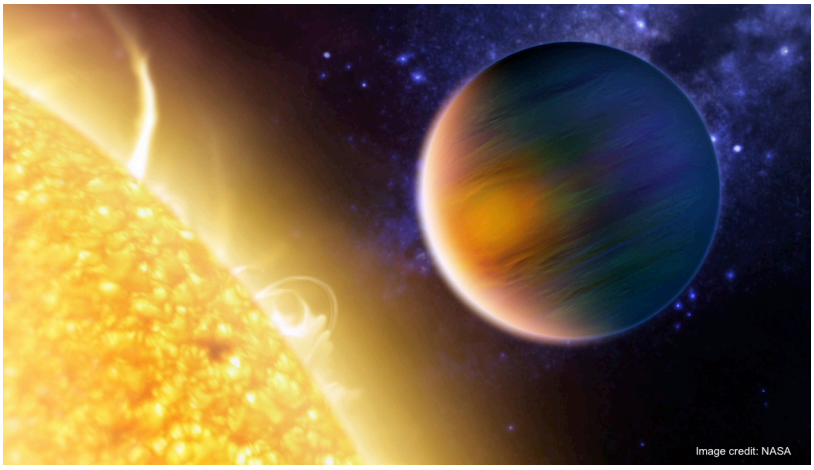

Hannah Ruth Wakeford

University of Exeter,
Stocker Road,
Exeter, Devon,
EX4 4QL

Thesis advisor: Dr. David K. Sing Hannah Ruth Wakeford

Cloudy with a Chance of Water: Investigating hot Jupiter exoplanet atmospheres through observation and analysis

Abstract

Since the discovery of the first exoplanet orbiting a sun-like star in 1995, the fundamental questions as to the formation of our Solar System have met a paradigm shift. The presence of hot Jupiter exoplanets, Jupiter sized worlds rapidly orbiting their host stars, was unlike anything previously seen or predicted. The later discovery of these strange new worlds transiting their stars opened up a new realm of studies into their atmospheres using transit spectroscopy to separate the signals between the star and planetary atmosphere. This thesis investigates the transmission spectral properties of hot Jupiter exoplanets through observations and theoretical analysis from the search for H_2O in the near-IR to the signatures of cloud condensates in the IR.

Hubble Space Telescope (HST) Wide Field Camera 3 (WFC3) observations of transiting hot Jupiters were used to investigate the atmospheric composition over water bands in the near infrared. We put forward a new analysis method to treat the varying systematics seen across transit datasets in a consistent and robust way, in which we marginalise over a grid of possible systematic models used to correct the lightcurves, with each model contributing to the extracted spectrum based on its statistical likelihood. We apply this new method to five previously studied hot Jupiter exoplanet transmission spectra and make direct comparisons between the planetary atmospheres. An apparent dichotomy emerges between two possible sub-classes of hot Jupiter atmospheres with clouds and hazes playing a key role. WFC3 appears to cover a critical wavelength range in exoplanet atmospheres where clouds and hazes potentially obscure the expected molecular signatures in systems where they are found to be obscured in the optical.

Using analytical models following Mie theory, we explore the potential atmospheric

transmission spectral signatures that would be caused by a variety of cloud condensates in hot Jupiter atmospheres. We find that the observed optical slope representing Rayleigh scattering at high altitudes can constrain the cloud condensate particle size and can be used as a diagnostic for potential condensate features in the IR where almost all condensate absorption features occur. We find that the major transmission spectral absorption features are generated by the vibrational modes of the major diatomic bond pair in each condensate species, which is often seen in the IR at 5–25 µm, and explore the potential for future JWST investigations using MIRI.

Contents

Listing of figures

List of Tables

Well, I suppose now is the time for me to say
something profound... nothing comes to mind.
GENERAL JACK O'NEILL
Stargate SG-1

Acknowledgments

None of this would have been possible without the financial support of the UK Science & Technology Facilities Council (STFC). The research leading to these results has also received funding from the European Research Council under the European Union's Seventh Framework Programme (FP7/2007-2013) / ERC grant agreement n° 336792.

Okay, now that we have the formalities out of the way it is time for the juicy bits. I have so many people to thank for their support throughout this doctoral endeavour so I shall attempt to do so here. This is for the people who will likely not read any further, save scanning the witty quotes marring each new chapter. Yet, for all of you I am still profoundly grateful.

To all who have ever shared an office with me, sorry, but I do believe that I warned each and every one of you in advance. I am especially thankful to Emily who stopped me from freaking myself out by allowing me to worry about her. Also, to Paul, the time vampire that he is, Tom Evans and Tiffany whose knowledge and patience far exceed that of my own.

To all the goofballs in the Astrophysics group who for some reason allowed me to take over and dictate their lives for a few nights a month/week. It has been a fantastic few years and for the most part it kept a smile on my face.

To Alex Pettitt, Moncho, and Simon who aided in my productive procrastination and helped me shout science to the world, I am definitely going to miss it. I am also

thankful to Matthew Bate who gave me the confidence and belief that I could get away with it in the first place.

To Andrew for enabling the crazy, Jon for joining in with the crazy, and Tom Wilson for embracing the crazy, I am sure he is still trying to convince himself that he knew what he was getting into. To David Amundsen who has been there through it all and even had to live with me to boot, I (and my family) cannot thank you enough so I will just say 'Well done sir, well done'.

My penultimate thanks goes to my supervisor David Sing. The freedom and genuine support that you have given me over the last few years taught me how to be a scientist and for that I cannot repay you, I only hope to one day pass it on down the line.

Finally, to my family who always encouraged me to do whatever the hell I wanted, within reason of course, and never wavered in their support and pride. That, and our shared love of Stargate, could not have done this without Stargate.

I tend to go with what you know. Until something better turns up.

COMMANDER WILLIAM ADAMA
Battlestar Galactica

1 Introduction

EXOPLANETS, planets that orbit stars other than the sun, have always been the work of science fiction, from Voltaire, to Roddenberry, Adams, and Clarke. The authors depicting worlds millions of times larger than the Earth inhabited by creatures 20,000 ft high[1], subterranean ocean worlds, desert planets, and utopian Earth-like havens. For millennia human beings have looked to the sky for the answers to the biggest questions, "*How did we get here?*", "*Is our solar system unique?*", and "*Are there any other planets with life out there?*". We may have not answered these questions yet, but every decade of scientific exploration brings us leaps and bounds closer. Confirming the existence of exoplanets in our Galaxy has opened up a whole realm of strange new worlds to explore, sparking a new branch of astrophysics. Now the exploration of their physical properties and atmospheres is well underway.

[1] Micronégas is a short story written by Voltaire in 1752 and is championed as the first ever science fiction literature.

1.1 Exoplanet discoveries

The first search for planets orbiting stars other than our sun was postulated by Christiaan Huygens in his book, Cosmotheoros, published posthumously in 1698. He questioned the ability to observe a planet passing in front of its star blocking out some of its light, as observed when the moons of Jupiter shadow the planet, or when Venus transits the sun. At the time the vast distances to the stars was not known and the amount of light that would be blocked by a "transiting" planet was greatly overestimated.

However, there are a number of different ways in which a planet can affect its host star, and in 1995 science fiction became fact when the first exoplanet was discovered orbiting another star much like our own Sun (Mayor & Queloz 1995). The Jupiter-mass planet discovered by Mayor and Queloz was indirectly measured using the Radial Velocity (RV) technique, which measures the induced variations in a star's spectrum due to the presence of an orbiting massive object pulling on the star as it orbits the centre of mass of the system. The gravitational pull of the planet causes the star to change velocity along the line of sight of the observer. The RV of the star shifts from the blue, when the star moves towards the observer as it orbits the center of mass of the planet-star system, and to the red, when the star is moving away. The observed changes in the RV signal depend on the companion's mass and the inclination angle between the planets orbital plane and the line of sight. As the inclination of the system cannot be disentangled from the RV signal alone, the measurements only yield the minimum mass of the companion. Mayor & Queloz (1995) measured a minimum mass of $M \sin i = 0.48 \pm 0.02\,\mathrm{M}_J$ for a planet in a 4.23 day orbit around the star 51 Pegasi, introducing us to a whole new type of planet never contemplated before: the 'hot Jupiter'. Hot Jupiters are defined as being roughly the same mass as Jupiter (1.89×10^{27} kg, $\sim$317 M_E), but orbiting their host star within 0.1 AU, $\sim$8 times closer to their stars than Mercury is to the Sun. Although this still remains a vague definition as we do not fully understand their formation and migration histories (Yaqoob 2011).

Since the first hot Jupiter observations using RV measurements, hundreds more have been observed. Figure 1.1.1[2] shows all the confirmed exoplanets as a function of mass and semi-major axis, which clearly shows the separation of the hot Jupiter class planets in the top left corner from the rest of the planet population. Also highlighted

[2]This research has made use of the Exoplanet Orbit Database and the Exoplanet Data Explorer at exoplanets.org.

for each planet is the measured radius of the planet, shown in the size and colour of the points on the plot. The radius of the planet can be measured using the transit technique suggested by Huygens, where the planet passes between the host star and the observer, blocking out a small portion of the light. By measuring the reduction in light over time the flux can be accurately measured to calculate the planet-to-star radius ratio over the course of the transit. Notably there are also three high mass planets in the top right corner of Fig. 1.1.1. These are three of the four directly imaged planets orbiting the young star HR 8799 (Marois et al. 2008, 2010). Direct imaging of exoplanets involves masking out the host star and observing the light directly emitted by the planet in combination with the reflected light from the host star. This makes the technique particularly sensitive to young, hot planets at large orbital distances from their stars.

In this thesis we focus on the observation and analysis of transiting exoplanets, particularly hot Jupiters, where a wide range of system parameters and planetary properties can be measured simultaneously.

1.2 Transiting exoplanets

While only a small portion of exoplanetary systems have favourable alignment to observe the transit of the planet as it passes in front of its host star, they offer us fundamental information about a plethora of system parameters. With a vast number of ground- and space-based transit detection surveys, observations of transiting exoplanets have rapidly increased in the last decade. Now over half of all confirmed exoplanets in our Galaxy have been observed through their transit, with thousands more still waiting to be confirmed. Ground-based surveys like HATsouth and WASP have provided multiple targets orbiting bright stars (V mag $\sim$7–11.5) suitable for follow-up observations (Pollacco et al. 2006). The Kepler space-based mission has produced statistics on the abundance of different worlds in our Galaxy, the presence of multi-planet systems, and the common system parameters across exoplanets and their host stars (e.g. Borucki et al. 2011; Kane et al. 2012; McQuillan et al. 2013; Batalha 2014).

The first exoplanet to be discovered transiting its host star, HD 209458, was a hot Jupiter (Charbonneau et al. 2000). HD 209458b is one of two hot Jupiter exoplanets found to orbit very bright stars, V magnitude < 8. Similar to RV measurements, the larger the planet and the shorter the orbit the easier they are to detect in transit.

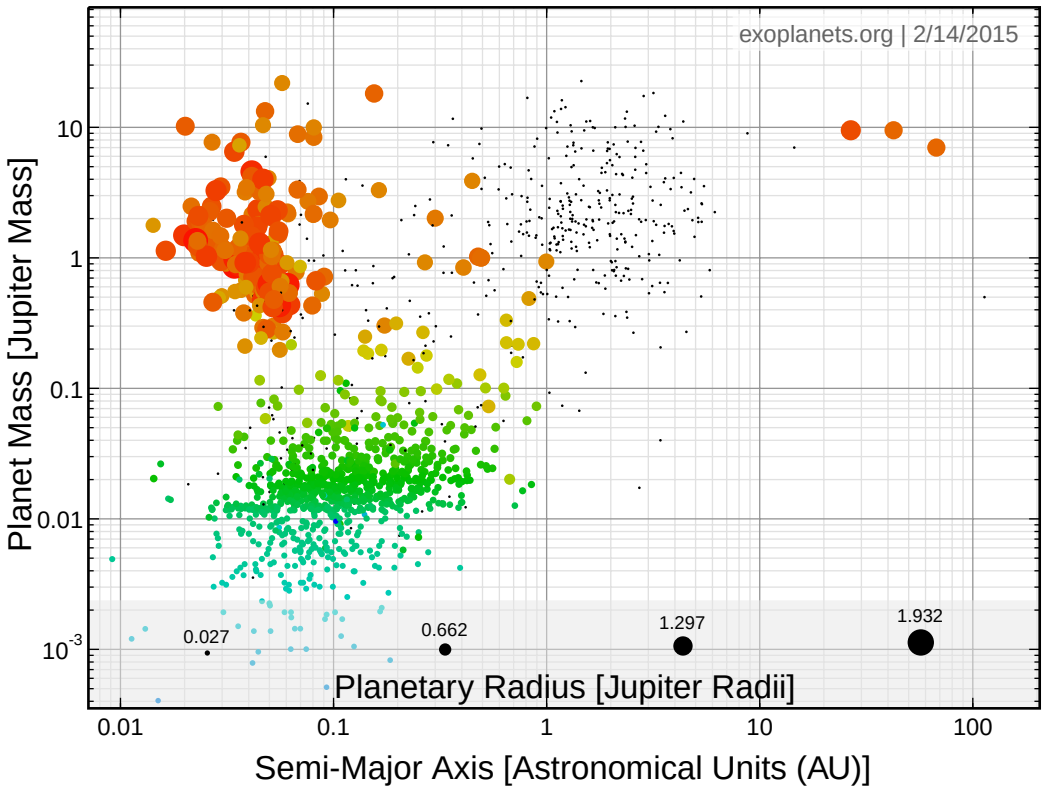

Figure 1.1.1: Mass vs. semi-major axis of all known exoplanets (Han et al. 2014). Each of the points is coloured on a scale from blue to red to indicate the increasing planetary radius additionally the point size is scaled in terms of increasing planetary radius (as indicated above the x-axis).

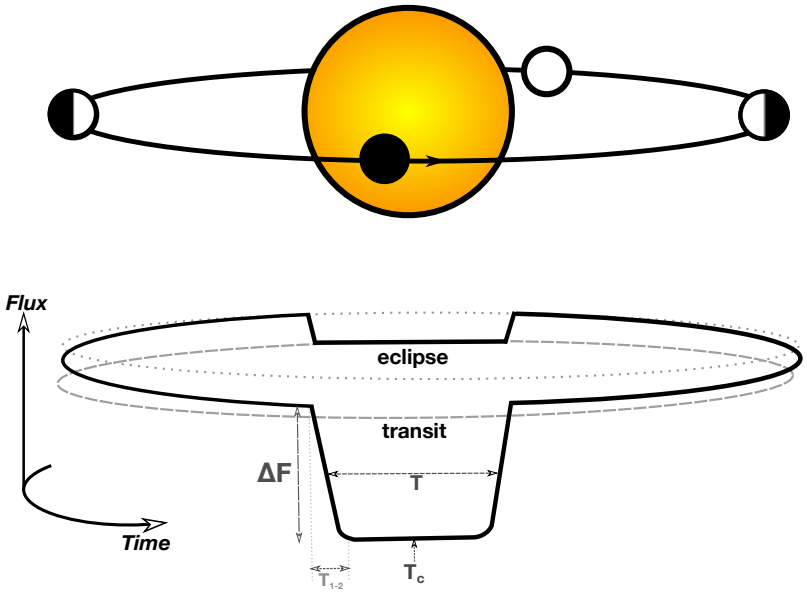

Figure 1.2.1: Schematic diagram of a planetary transit and eclipse showing the planetary orbit and the day/night contrast as the planet orbits the star. The bottom of the figure shows the flux measured over time as the planet orbits, and indicates the different transit parameters we are interested in.

Transiting planets allow for a precise measurement of both the star's mass and radius, as well as constraining the planet's spin-orbit alignment, bulk composition, temperature, albedo, and the atmospheric composition, structure, and dynamics. Transiting exoplanets have been responsible for an array of firsts in exoplanet studies, including the first detection of an exoplanet atmosphere (Charbonneau et al. 2002), first observation of direct light from an exoplanet (Deming et al. 2005), first emission spectrum (Grillmair et al. 2007), temperature map (Knutson et al. 2007b), and transmission spectra (e.g. Sing et al. 2008; Pont et al. 2008; Redfield et al. 2008; Sing et al. 2011a; Sing et al. 2013).

Figure 1.2.1 shows a schematic diagram of a planetary transit depicting the primary transit and secondary eclipse of a system. During the transit the observed flux of the system drops as the opaque planet blocks out a portion of the starlight. This is measured as the change in relative flux (δ) of the system,

$$\delta = \frac{\Delta F}{F} = \left(\frac{R_P}{R_*}\right)^2, \tag{1.1}$$

where F is the measured flux of the system, ΔF is the change in flux of the system, R_P is the radius of the planet, and R_* is the radius of the star, assuming negligible

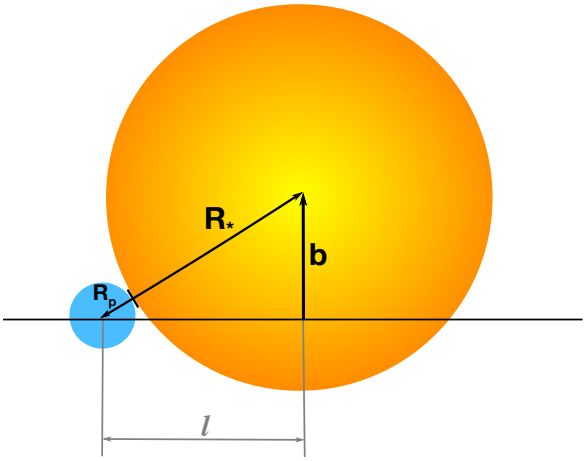

Figure 1.2.2: Schematic of the transit impact parameter and geometry of the systems transit time.

flux directly from the planet. As the planet orbits the star, revealing more and more of the dayside hemisphere, the flux increases, due to the thermal and reflected emission of the planet itself. Just prior to the planet passing behind the star in secondary eclipse, both the dayside planet flux and stellar flux are observed. When the planet is eclipsed completely, only the stellar spectrum is observed, which is subtracted from combined flux measurement to leave just the planetary flux.

The duration of the transit across the face of the star is determined by the projected path taken by the planet across the stellar disk (see Fig. 1.2.2). This path is defined by an impact parameter b which is the shortest distance from the planet to the centre of the star,

$$b = a \cos i, \tag{1.2}$$

where a is the semi-major axis, and i is the inclination of the planetary orbital plane with the vertical.

Using this we can derive the exact general expression for the transit duration T. Figure 1.2.2 shows the geometry of the transit with the planet placed at 1st contact just prior to the planet disc entering the stellar disc, making a right angled triangle with $R_p + R_*$ as the hypotenuse, and the impact parameter as the vertical. The distance covered by the transit is then equal to $2l$, where

$$l = \sqrt{(R_p + R_*)^2 - b^2}. \tag{1.3}$$

Assuming a circular orbit, the planet will move through an angle α as it proceeds from 1st to 4th contact just after the planet disc has passed out of the stellar disc.

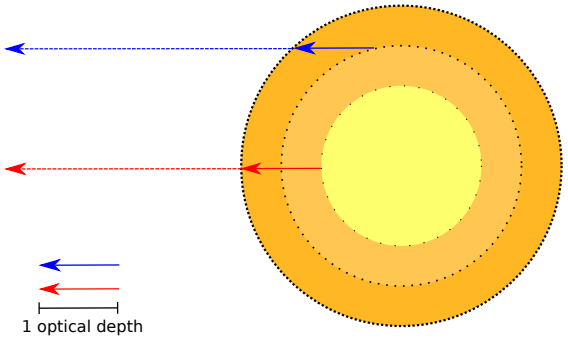

Figure 1.2.3: Figure showing limb-darkening in terms of the optical depth of the stellar atmosphere being observed. The observed light is emerging from the same optical depth in the stellar atmosphere, but at different temperature regions in the star.

From this $\sin(\alpha/2) = l/a$, giving a total transit time of

$$T = \frac{P}{\pi}\sin^{-1}(l/a), \tag{1.4}$$

where P is the planet's orbital period.

1.2.1 Limb-darkening

Limb-darkening (LD) is the effect observed on the stellar disc where the star appears brighter in the centre, and progressively dimmer and redder towards the limb (see Figs. 1.2.1, 1.2.2). This is due to the change in depth of the atmosphere being observed. At the limb of the star the region of the atmosphere being observed at slant geometry is at higher altitudes in the stellar atmosphere and thus lower temperatures, compared to the deeper atmosphere observed at the centre of the star where it is hotter (see Fig. 1.2.3). LD is strongest in the blue and weakest in the red, making the stellar disk appears progressively darker towards the limb. This means that when the planet is in front of the centre of the star, it will be blocking out a higher amount of stellar flux than when it is at the limb. This causes the light curve to be rounded at the edges of the transit, rather than appearing as a sharp square dip. Knutson et al. (2007a) found that limb-darkened curves for HD 209458 are similar to those of the Sun at longer wavelengths, but exhibit greater centre-to-limb variation at short wavelengths. Taking into account the effects of limb darkening on the light curve is required for accurate estimates of the radius and orbital inclination of an exoplanet.

The most commonly used LD laws in the analysis of exoplanet transit lightcurves are the quadratic law,

$$\frac{I(\mu)}{I(1)} = 1 - c_1(1-\mu) - c_2(1-\mu)^2, \tag{1.5}$$

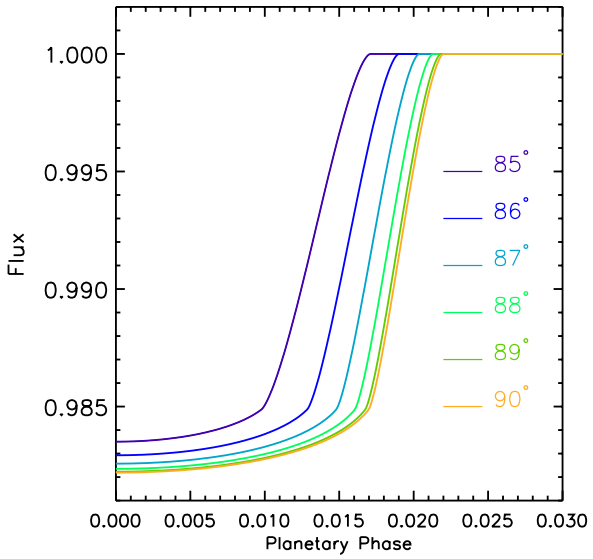

Figure 1.2.4: Figure showing the change in the shape of a planetary transit when the inclination of the system is changed, and therefore the portion of the stellar atmosphere obscured by the planet.

and the non-linear limb darkening law,

$$\frac{I(\mu)}{I(1)} = 1 - c_1(1-\mu^{1/2}) - c_2(1-\mu) - c_3(1-\mu^{3/2}) - c_4(1-\mu^2), \tag{1.6}$$

where $I(1)$ is the intensity at the centre of the stellar disk, $\mu = \cos\theta$, with θ defined as the angle between the normal from the surface of the star and the direction of the observer, and c_{1-4} are the coefficients of limb darkening (Claret 2000).

The LD coefficients depend on the specific stellar atmosphere and therefore vary from star to star. Stellar models are used to compute the LD coefficients where the temperature and metallicity of the star inform the change in flux observed across the stellar disk. These are then used in conjunction with a transit model such as that from Mandel & Agol (2002) which is an analytic transit model used to compute the observed lightcurve for a transiting exoplanet system. The shape of the lightcurve is also highly dependent on the inclination of the planet's orbit relative to the observer, i.e. where on the stellar disk the planet transits. Figure 1.2.4 shows the egress of a planetary transit and how the lightcurve changes with inclination, where a planetary phase of 0.0 is the centre of the transit.

1.3 Transmission spectroscopy

Transiting planets offer a unique opportunity to study their atmospheres through a method called transmission spectroscopy. The understanding of planetary at-

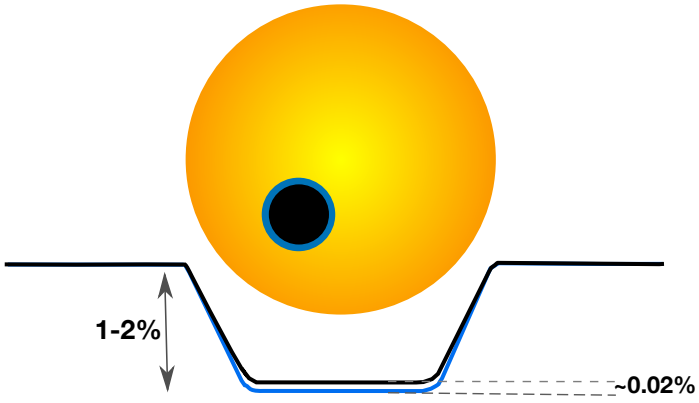

Figure 1.3.1: Schematic diagram of a planetary transit, where the planet has a large extended atmosphere. The average change in the amount of flux observed during the transit of a planet with an extended atmosphere is shown in the bottom of the figure, indicating the expected depth difference caused by an extended atmosphere.

mospheres has improved considerably in the last decade, thanks in part to multi-wavelength observations of transiting exoplanets. It is expected that a large fraction of the planets currently observed transiting their stars will have extended atmospheres. As the planet passes in front of its star a small portion of the starlight will pass through this atmosphere before reaching us. As the starlight passes through their upper atmospheres, characteristic spectral signatures are superimposed on the light as it is absorbed or scattered. The absorption and optical depth of the atmosphere is dependent on wavelength, as is the altitude at which the planet is opaque to starlight. These atmospheric signatures in the lightcurve are often on the order of $\sim$0.02% for the largest exoplanets observed (see Fig. 1.3.1). A transmission spectrum is constructed from the measured planet-to-star radius ratio (R_p/R_*) across a series of wavelengths. Absorption features manifest as larger R_p/R_* values where more starlight is being absorbed by the atmosphere. Features observed in the transmission spectrum place strong constraints on the possible species in the atmosphere (e.g. Seager & Sasselov 2000; Charbonneau et al. 2002).

The transmission spectrum of an exoplanet atmosphere is most easily observed for large, low density planets, in close-in orbits around bright stars where a large number of photons can pass through the atmosphere before reaching the observer. This places hot Jupiters in a vital parameter space for follow-up atmospheric studies through their transmission spectra, as they are expected to have rich H/He atmospheres. Figure 1.3.2[3] shows the Mass-Radius plot for all transiting exoplanets. The trend following the black points shows the estimated mass for a number of the Kepler planets, with the hot Jupiters occupying the top-right distribution of points. Highlighted on this diagram are the hot Jupiter exoplanets focused on in this thesis. Due to the proximity

[3]This research has made use of the Exoplanet Orbit Database and the Exoplanet Data Explorer at exoplanets.org.

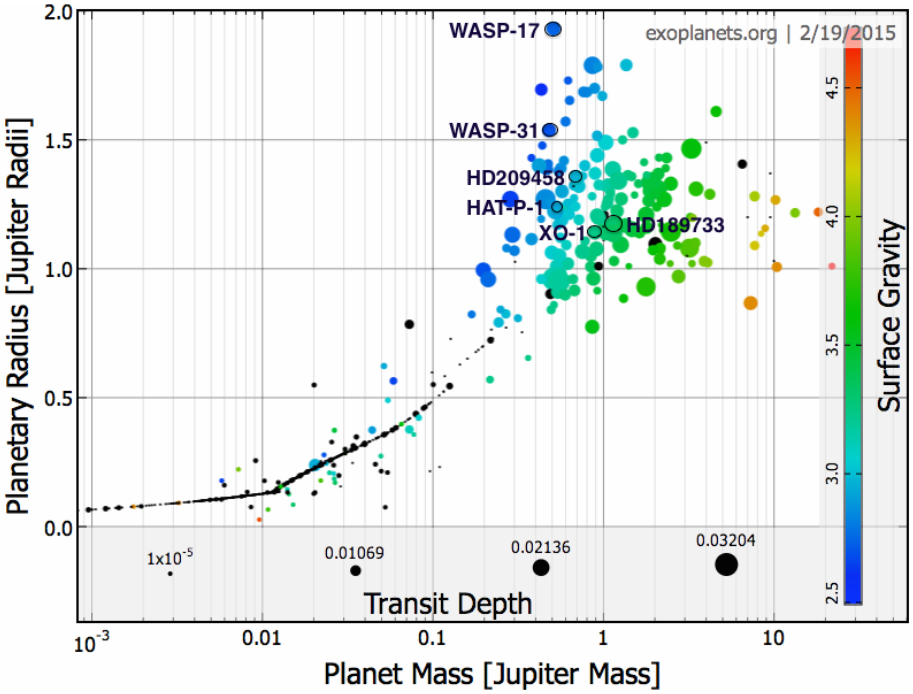

Figure 1.3.2: Mass-Radius diagram for all transiting exoplanets (Han et al. 2014). The size of each point shown in the scale along the bottom indicates the transit signal observed for that planet. The colour scale is then use to show the measured surface gravity of the planet. The hot Jupiters analysed in this thesis are highlighted and labelled.

to their host stars, hot Jupiters occupy a high temperature regime, ~800 to 3000 K. High temperatures combined with low surface gravity produces a large atmospheric scale height H. This describes the altitude range where the atmosphere pressure decreases by a factor e, such that

$$H = \frac{k_B T}{\mu_m g}, \tag{1.7}$$

where k_B is the Boltzmann constant, T is the estimated atmospheric temperature, μ_m is the mean molecular weight of the atmosphere, and g is the surface gravity. The larger the planetary scale height, the larger the expected atmospheric signal, and therefore the greater the change in measured planetary radius relative to the star, $\Delta R_p/R_*$.

The absorption and scattering properties of an atmosphere differ significantly when viewed at a *slant* geometry than normal geometry to the planet's atmosphere (see Fig. 1.3.3). It follows that in transmission spectra, where the planet's atmosphere is

observed at a slant, minor condensates, with low optical depths when viewed normal to the planet can become very significant (Fortney 2005). The formulae outlined in Fortney (2005) and Lecavelier des Etangs et al. (2008) can be used to derive the basic properties obtained from transmission spectral measurements observed at these geometries. When the density over the slant geometry is integrated and compared to that observed normal to the atmosphere the difference in absorption and scattering properties of the atmosphere can be measured. For the Earth the ratio of density at slant geometry compared to normal geometry is ∼75, and ∼128 for Jupiter, with ∼35-90 for hot Jupiter exoplanets (Fortney 2005). The optical depth (τ) at slant geometry is then

$$\tau(\lambda, z) \approx \sigma(\lambda) n(z) \sqrt{2\pi R_p H}, \tag{1.8}$$

where $n(z)$ is the volume density of the atmosphere at altitude z for the main absorbing species with an absorbing cross-section $\sigma(\lambda)$. At the low pressures observed in transmission it is reasonable to assume that the temperature of the atmosphere is constant to within a few hundred degrees. Assuming that the atmosphere is in hydrostatic equilibrium with constant mean molecular weight and gravity, the density profile at slant geometry can be calculated. The effective altitude of a planetary atmosphere z can then be calculated following the determination of the optical depth at a given wavelength λ,

$$z(\lambda) = H \ln \left(\frac{\xi_{abs} P_{(z=0)} \sigma_{abs}(\lambda)}{\tau_{eq}} \times \sqrt{\frac{2\pi R_p}{k_B T \mu_m g}} \right), \tag{1.9}$$

where ξ_{abs} and σ_{abs} are the abundance and cross-section of the absorbing species, $P_{(z=0)}$ is the pressure where $z = 0$, and τ_{eq} is the optical thickness at the effective altitude radius $z(\lambda)$. Lecavelier des Etangs et al. (2008) show that for a range of atmospheric scale heights, providing R_p/H is roughly between $30-3000$, $\tau_{eq} \approx 0.56$, which can be assumed for most hot Jupiter exoplanet atmospheres probed with transmission spectroscopy. In chapters 4 and 5 we apply this to the atmosphere of the hot Jupiter HD 189733b to calculate the effective altitude of condensate clouds that will potentially form.

1.3.1 Spectral features

The presence of specific spectral features in the atmospheric transmission spectra of close-in giant planets was first analysed in Seager & Sasselov (2000). The chemistry

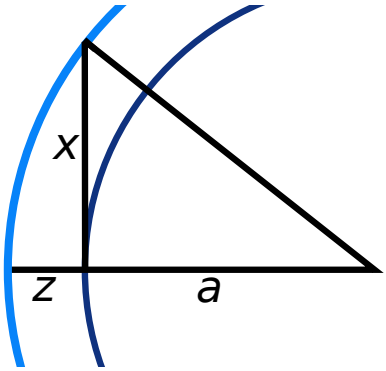

Figure 1.3.3: Diagram of the normal geometry of a planetary atmosphere viewed along z compared to that viewed at a slant angel along x reaching the same pressure depth and height in the planetary atmosphere. Where a is the radius of the planetary body at the greatest pressure depth.

of an atmosphere is determined by the elemental abundance and the temperature and pressure of the atmosphere. Figure 1.3.4 shows the chemistry expected in exoplanet atmospheres at slant geometries during transit, assuming equilibrium chemistry and constant temperature and gravity throughout the atmosphere (Fortney et al. 2010).

Using chemical equilibrium models and assuming solar abundances, Seager & Sasselov (2000) determined the differentiating features between the observed stellar spectrum and that of the planet's atmosphere superimposed on the light. Similar to brown dwarf atmospheres, the alkali metal lines of Sodium (Na) and Potassium (K) were predicted to have very strong absorption signatures in the optical. Detections of these atomic absorption features are unambiguous as they are the only absorbers at their specific wavelength ranges (Charbonneau et al. 2002). In addition to the presence of the atomic alkali metal lines, the transmission spectrum is expected to be dominated by molecular vibro-rotational bands from H_2O, and carbon dominant molecules such as CO for hot atmospheres and CH_4 for cooler atmospheres (see Fig. 1.3.4). These molecular bands are mostly found in the IR and produce broad absorption features that can span several microns. For very hot exoplanet atmospheres, greater than 2000 K, the highly absorbing species TiO and VO are expected to be present at high altitudes with a broad absorption peak in the optical spanning $\sim 0.3 - 0.9\,\mu$m (see Fig. 1.3.4).

The first transmission spectral observation of an exoplanet atmosphere was conducted on HD 209458b by Charbonneau et al. (2002) centred on the Na resonant doublet using the Hubble Space Telescope (HST) Space Telescope Imaging Spectrograph (STIS) medium resolution spectrograph. They find that, while Na absorption is detected at the predicted wavelength, less absorption is observed than assumed by models at solar abundances. This could suggest that the Na is depleted by condensation or ionization (Sing et al. 2008). Following this detection, Na absorption

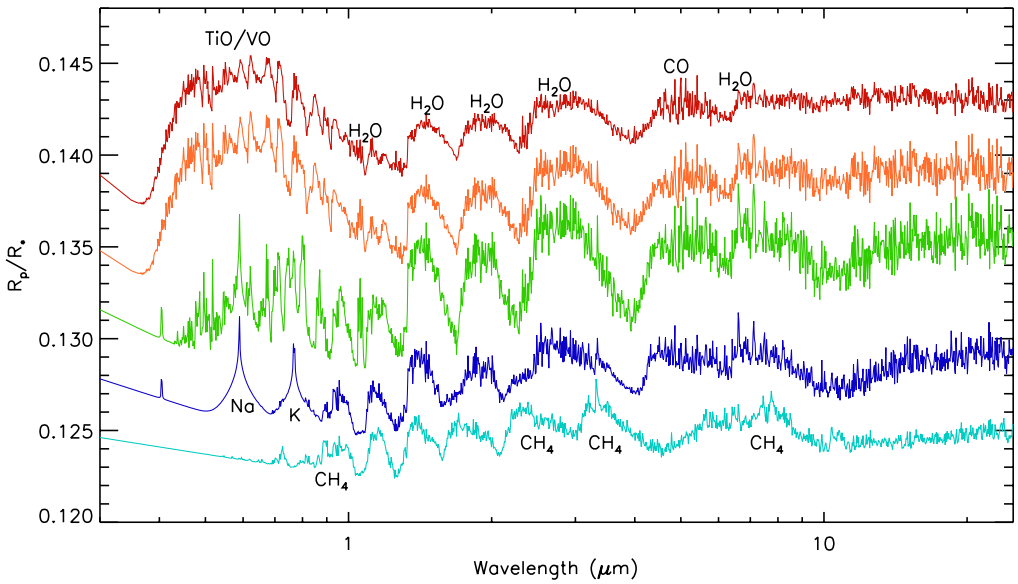

Figure 1.3.4: Model transmission spectra for isothermal atmospheres with a gravitational acceleration of 25 ms^{-2} based on Fortney et al. (2010) calculations. Models are $T = 2500$, 2000, 1500, 1000, 500 K from top to bottom and assume chemical equilibrium. The labels indicate prominent absorption features expected in the transmission spectra.

has been observed in the atmosphere of HD 189733b (Redfield et al. 2008), XO-2b (Sing et al. 2011a), WASP-17b (Wood et al. 2011; Zhou & Bayliss 2012), HAT-P-1b (Nikolov et al. 2014), and confirmed in the atmosphere of HD 209458b from ground based observations by Snellen et al. (2008). For a majority of exoplanet models it is assumed that the elemental composition is similar to solar. When heated above 1000 K the spectrum will be dominated by H_2O, and depending on the metallicity will also include CO and/or CH_4 (Seager & Deming 2010). Table 1.3.1 lists all of the observed atomic and molecular absorption features seen in the lower atmospheres, through transmission of exoplanet atmospheres listing the instrument, wavelength range, and reference for each detection.

The major species that have been detected in the atmospheres are not unexpected; however, the strength of each feature relative to that predicted by models is often not consistent with model predictions, this may indicate variations in the abundance of different atoms from solar. The use of specific filters and instruments in the optical have aided in the detection of the Na and K doublets at high resolutions from the ground. However, the majority of the spectroscopic observations of transiting planets in recent years have been conducted using HST/STIS, Near Infrared Camera and

Table 1.3.1: Table of published transmission spectral features detected listing the instrument, wavelength, and reference for each planet with a detected feature (atomic species, molecule, cloud/haze) in its atmosphere. This is a condensed and updated version of Tables 6 and 7 found in Bailey (2014).

Planet	Instrument	Wavelengths (µm)	Features	Reference
GJ 1214b	HST/WFC3	1.1–1.7	clouds	Kreidberg et al. (2014b)
HAT-P-1b	HST/WFC3	1.1–1.7	H_2O	Wakeford et al. (2013)
	HST/STIS	0.589 (3.0 nm)	Na	Nikolov et al. (2014)
HAT-P-12b	HST/WFC3	1.1–1.7	clouds	Line et al. (2013)
HD 189733b	HST/NICMOS	1.4–2.5	H_2O, CH_4	Swain et al. (2008)
	HST/ACS	0.55–1.05	haze	Pont et al. (2008)
	HET/HRS	0.589 (1.2 nm)	Na	Redfield et al. (2008), Jensen et al. (2011)
	HST/NICMOS	1.66–1.87	haze, no H_2O	Sing et al. (2009)
	HST/STIS	0.29–0.57	haze	Sing et al. (2011b)
	HST/STIS	0.589 (0.5 nm)	Na	Huitson et al. (2013)
	HST/WFC3	1.1–1.7	H_2O	McCullough et al. (2014)
HD 209458b	HST/STIS	0.589 (1.2 nm)	Na	Charbonneau et al. (2002)
	HST/STIS	0.3–1.0	H_2O	Knutson et al. (2007a), Barman (2007)
	Subaru/HDS	0.589 (0.3 nm)	Na	Snellen et al. (2008)
	HST/STIS	0.589 (0.44 nm)	Na	Sing et al. (2008)
	HET/HRS	0.589 (1.2 nm)	Na	Jensen et al. (2011)
	HST/WFC3	1.1–1.7	H_2O	Deming et al. (2013)
WASP-6b	HST/STIS, Spitzer/IRAC	0.29–4.5	K, clouds/haze	Nikolov et al. (2015)
WASP-12b	HST/STIS+WFC3	0.3–1.7	haze, aerosols	Sing et al. (2013)
WASP-17b	VLT/GIRAFFE	0.589 (0.15 nm)	Na	Wood et al. (2011)
	Magellan/MIKE	0.589 (0.15 nm)	Na	Zhou & Bayliss (2012)
WASP-19b	HST/STIS+WFC3	0.3–1.7	H_2O, no TiO	Huitson et al. (2013)
WASP-31b	HST/STIS+WFC3	0.3–1.7	K, no H_2O, clouds	Sing et al. (2015)
WASP-43b	HST/WFC3	1.1–1.7	H_2O	Kreidberg et al. (2014a)
XO-1b	HST/NICMOS	1.2–1.8	H_2O, CH_4, CO_2	Tinetti et al. (2010)
	HST/WFC3	1.1–1.7	H_2O	Deming et al. (2013)
XO-2b	GTC/OSIRIS	0.589 (5.0 nm)	Na	Sing et al. (2011a)
	GTC/OSIRIS	0.766 (5.0 nm)	K	Sing et al. (2011a)

Multi-Object Spectrometer (NICMOS), and Wide Field Camera 3 (WFC3), which are all low to medium resolution instruments not specifically designed for the purpose of transmission spectroscopy. The most extensively studied exoplanet atmospheres to date have been HD 209458b and HD 189733b, which orbit nearby bright stars allowing for superior photon collection. To explore the extent of transmission spectral features observed in hot Jupiter exoplanet atmospheres, Fig. 1.3.5 shows the published transmission spectra of five example hot Jupiter exoplanet atmospheres displaying the diversity of observed absorption features.

The transmission spectrum of HD 209458b has been observed multiple times with a wide number of instruments from ground- and space-based observations, ranging from the ultraviolet (UV) to the infrared (IR), which have been able to probe both the lower and extended upper atmosphere (e.g. Vidal-Madjar et al. 2003, Vidal-Madjar et al. 2004; Narita et al. 2005; Knutson et al. 2007a; Snellen et al. 2008; Linsky et al. 2010). Figure 1.3.5 shows the combined data from HST/STIS (Sing et al. 2008) and WFC3 from the optical to near-IR (Deming et al. 2013). The transmission spectrum shows broadband absorption features in the the NUV and at the Na absorption wavelengths, with a resolved Na line core, but no K absorption. In the near-IR a low amplitude H_2O feature is reported, the interpretation of which is still open for debate with a high altitude obscuring haze stretching into the IR wavelength range or potentially either a low primordial water abundance in the system which would lower the altitude at which H_2O is observed allowing other molecules to become obscuring at those wavelengths.

HD 189733b has an almost featureless atmospheric transmission spectrum below 1 µm with strong Rayleigh scattering slope and no indication of the expected alkali metal lines (Pont et al. 2008). This is interpreted as a haze of condensate grains extending over at least five atmospheric scale heights across the optical wavelength regime (Pont et al. 2013). Additionally, McCullough et al. (2014) report the detection of two water vapour features in the near-IR with WFC3, and interpret the Rayleigh scattering between 0.5 – 1.0 µm to potentially be caused by the presence of un-occulted starspots on the host star, which is known to be active. The detection of the Rayleigh scattering haze in HD 189733b's atmosphere provides a vast amount of information about the atmospheric pressure structure when combined with near-IR spectra, and we discuss in chapter 5 how the slope of the scattering haze in the optical can be used to infer the presence of specific cloud condensates observable in the mid-IR with JWST.

HAT-P-1b's transmission spectrum displays multiple spectral absorption features

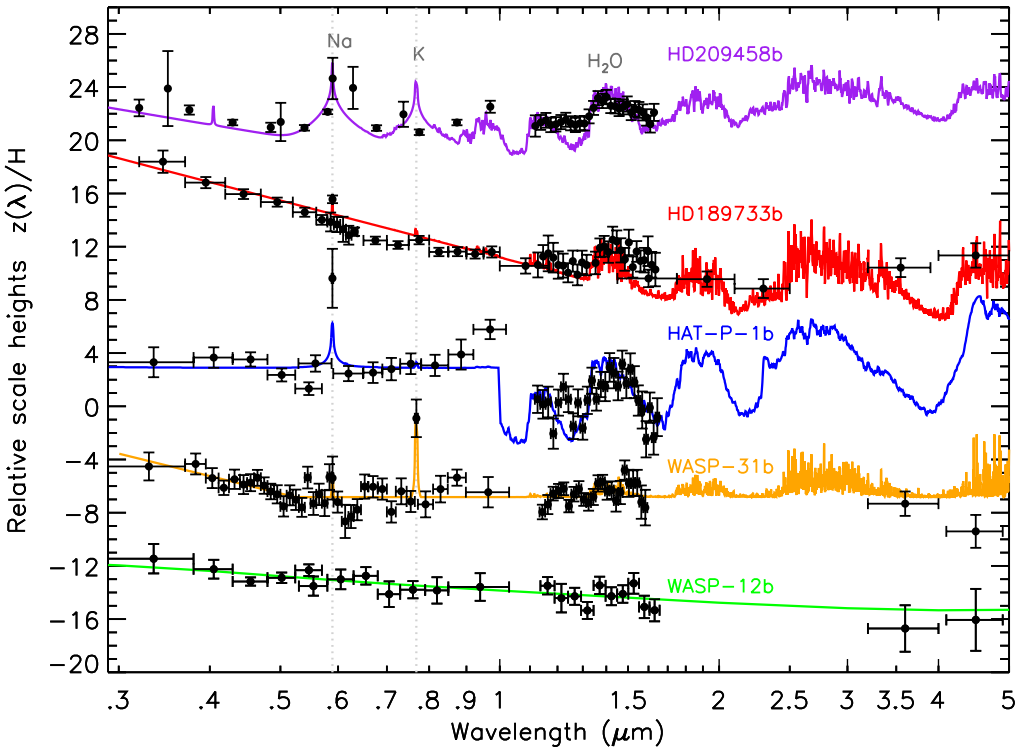

Figure 1.3.5: Published transmission spectra of six hot Jupiter atmospheres from HST and *Spitzer* observations: HD 209458b, HD 189733b, HAT-P-1b, WASP-31b, and WASP-12b (see the text for references). The spectra are displayed on a common scale for comparison.

with strong Na absorption measured at 3.3σ and H_2O detected with greater than 4σ significance (Nikolov et al. 2014; Wakeford et al. 2013). The optical STIS and near-IR WFC3 observations, however, differ significantly in the measured absolute radius values by multiple scale heights, which cannot be explained by a single atmospheric model. The model shown in Fig. 1.3.5 is an isothermal model by Burrows et al. (2010) with an 'extra absorber' at altitudes with an opacity of $0.03\,\mathrm{cm^2 g^{-1}}$ from $0.4-1.0\,\mu\mathrm{m}$. However, efforts continue to be made to explain these observations based on physical sources in the planet's atmosphere.

The WASP-31b transmission spectrum is dominated by a cloud deck producing a flat spectrum from the optical into the IR (Sing et al. 2015). The strong K feature and lack of Na feature is the first indication of a sub-solar Na/K abundance ratio, which can potentially be explained by Na condensation on the nightside of the planet. The cloud deck continues into the near-IR, obscuring the expected H_2O features and suggesting high altitude, clouds of micron sized particles below a sub-micron sized particle haze which causes the Rayleigh scattering observed in the optical.

The transmission spectrum of WASP-12b displays no spectral absorption features from atomic or molecular species in the optical and near-IR bands shown in Fig. 1.3.5. UV observations of the system hint at the presence of an extended atmosphere with potential metallic pollution between the planet and the star (Fossati et al. 2010; Haswell et al. 2012). As a potentially very hot atmosphere, $\gtrsim 2200\,\mathrm{K}$, the highly absorbing species TiO and VO were expected to be present as either a broad feature or through individual bandheads. Sing et al. (2013) find that the spectrum is most likely explained by high altitude aerosols including Rayleigh scattering, Mie scattering, tholin hazes, and dust opacities, which are able to fully obscure specific absorption signatures.

Thus far there has been no observational evidence in transmission of the expected high temperature absorbers TiO and VO in the terminator of even the hottest exoplanets (e.g. Huitson et al. 2013; Sing et al. 2013). The presence or absence of hazes and clouds in hot Jupiter atmospheres appears to be a major distinguishing feature, with roughly half the observed atmospheres showing one or the other general characteristic. Observationally constraining the presence of absorption features in the transmission spectra across all available wavelengths aids in the constraint of cloud and haze formation, where transmission spectra are highly sensitive to obscuring particles.

1.4 Emission spectroscopy

As the planet passes behind the star during secondary eclipse the thermal emission from the dayside of the planet is occulted, which produces a small change in the overall flux observed of the system ΔF_{SE} (see Fig. 1.2.1). This change in flux represents the emission from the dayside of the planet. If we assume that the planet radiates as a black body then the effective temperature T_{eff} can be used to approximate the flux at any wavelength λ per unit surface area. The observed flux is then

$$\frac{\Delta F_{SE}}{F} \approx \left[\frac{(1-P)(1-A)}{2a^2}\right]^{1/4} \frac{R_P^2}{R_*^{3/2}}, \tag{1.10}$$

where ΔF_{SE} is the change in flux observed at secondary eclipse, F is the total flux of the system, A is the bond albedo, and P is the fraction of the absorbed energy that is transported to the night side of the planet. As the planet proceeds along its orbit the dayside will steadily rotate out of view. This causes a very small change in the amount of flux observed over the course of the orbit as the amount of emission observed directly from the planet changes, producing a phase curve.

Emission spectroscopy in the IR is an extremely powerful way to characterise exoplanet atmospheres during secondary eclipse. *Spitzer* secondary eclipse observations using the photometric IR channels have been key to detecting planetary emission from hot Jupiters down to super-Earths (e.g. Deming et al. 2005; Charbonneau et al. 2005; Knutson et al. 2007b, Knutson et al. 2012; Stevenson et al. 2014c). From spectroscopic measurements of the planet's dayside emission, the planet's effective temperature, heat-redistribution, geometric albedo, molecular abundances (though none have been measured yet), and atmospheric temperature profile can be retrieved.

The first secondary eclipse detection was conducted by Deming et al. (2005) on HD 209458 using *Spitzer*'s 24 µm band. Since then *Spitzer* has been used to observe the secondary eclipse of nearly 40 exoplanets (Bailey 2014). The primary source of secondary eclipse observations are the IRAC 3.6 and 4.5 µm photometric bands, which are part of the still active warm *Spitzer* campaign, with the addition of the 5.8 and 8.0 µm photometric bands, which were available until 2009 when the coolant ran out limiting the instrument response. For the brightest systems it is possible to obtain not just photometric measurements of their dayside temperatures, but also spectroscopic measurements. Thus far only eight exoplanets have had their atmospheres investigated spectroscopically through their emission during secondary eclipse, with less than a handful showing strong evidence for spectroscopic emission features (e.g.

Crouzet et al. 2014; Kreidberg et al. 2014a; Stevenson et al. 2014c).

Atmospheric retrieval techniques are being applied to emission spectra from both *Spitzer* and HST secondary eclipse measurements in a effort to constrain multiple atmospheric parameters, from composition to temperature structure. A major limitation for this is the unresolved nature of molecular features in the observed spectra where isothermal atmospheres will hide any features that may be present. With additional degeneracies between models, it is often not possible to resolve specific molecular features in the spectra (e.g. Madhusudhan & Seager 2010; Benneke & Seager 2012; Barstow et al. 2014).

Spectroscopic observations of HD 189733b conducted with *Spitzer* IRS during ten secondary eclipse events reveal evidence for strong H_2O emission at 6 µm (Grillmair et al. 2008). This result was later validated by Todorov et al. (2014) in a re-analysis of all archival HD 189733 *Spitzer* datasets. However, they note that broad wavelength coverage and high spectral resolution observations are needed for such studies since rejection of isothermal and grey atmospheric models is based on only a few of the ∼60 secondary eclipse measurements made of the planet. With this in mind, the spectral retrieval of several molecular species from photometric emission spectra across the four *Spitzer* IRAC channels needs to be carefully analysed.

1.4.1 Phase curves

Detection of molecular features through emission in secondary eclipse and phase curve observations have been attempted on a handful of planets (e.g. Machalek et al. 2008; Knutson et al. 2008; Charbonneau et al. 2008; Grillmair et al. 2008; Swain et al. 2009b; Rogers et al. 2009; Waldmann et al. 2012; Todorov et al. 2014). Figure 1.4.1 shows the phase curve observed over three planetary orbits of WASP-43b from HST/WFC3 (Stevenson et al. 2014c). The initial dip in the lightcurve at an orbital phase of 0.0 is caused by the planetary transit where the nightside is facing towards the observer, followed by a smooth increase in the flux leading up to the secondary eclipse, seen as a small decrease in the overall flux of the system, which then smoothly decreases as the planet proceeds towards the primary transit. It is clear in the phase curve that the maximum flux of the system occurs just prior to the secondary eclipse of the planet behind the star, where it would be expected to peak. This indicates the presence of eastward advection potentially in the form of a jet carrying the heat away from the sub-stellar point. Observations by Knutson et al. (2012), using *Spitzer* IRAC at 3.8 and 4.5 µm, in addition to 8.0 and 24 µm observations (Knutson et al. 2007b),

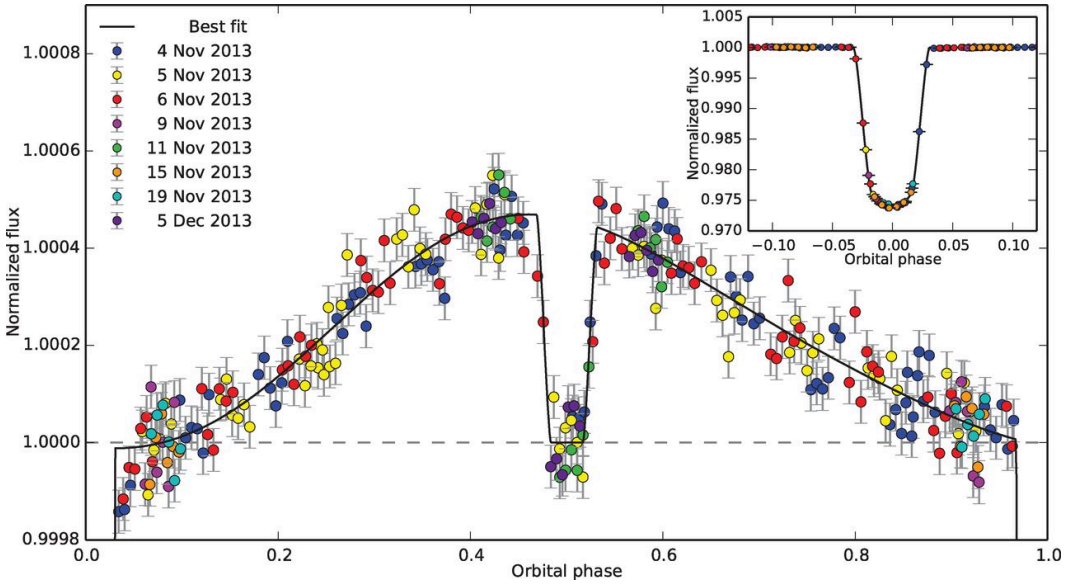

Figure 1.4.1: Band integrated phase curve of WASP-43b taken from Stevenson et al. (2014c). The systematic-corrected flux values are binned in time, normalised to stellar flux and have 1σ errorbars. Each colour represents the different HST visits used to acquire the data from WFC3, with the black line representing the best model fit to the data.

also found that the peak in maximum flux of the HD 189733b system was shifted, providing evidence for eastward advection of gas by a super-rotating jet shifting the planet's atmospheric hot spot from the sub-stellar point as heat is transported away. Broad super-rotating jets have been predicted to occur in the atmospheres of close-in planets by atmospheric circulation models, transporting energy from the dayside to the nightside of the planet (e.g. Showman et al. 2009; Showman & Polvani 2011). The day-to-night contrast and wind speeds of the planet's atmosphere can vary dramatically depending on a range of planetary system and atmospheric properties (e.g. Lewis et al. 2010; Rauscher & Menou 2012; Kataria et al. 2015). The shifted hot spot on the dayside informs the altitude and opacity dependence of the balance between advective and radiative timescales. However, with few planets observed in emission through their phase curve (Stevenson et al. 2014c), the global wind patterns in hot Jupiter atmospheres, and their dependence on particular parameters, remain unconstrained.

1.4.2 Albedo

Atmospheric circulation partly controls the surface temperatures and drives large scale cloud structures (and hence the albedo) for terrestrial planets (Seager & Deming 2010). The fact that exoplanets emit strongly in the IR suggests that they efficiently absorb the incident stellar irradiation on the atmosphere. Searches for the reflected component of their energy budget have indicated that the planets must be very dark in visible light, with geometric albedos less than about 0.2 (Rowe et al. 2008) and likely much lower. Cloud condensation in the atmospheres of hot Jupiters can also loft small particles into the upper atmosphere reflecting more light, raising the albedo considerably (Marley & McKay 1999, Sudarsky et al. 2000).

Evans et al. (2013) measured the geometric albedo of HD 189733b in the optical with HST/STIS finding that the albedo decreases towards longer wavelengths. This can be interpreted as evidence for optically thick reflective clouds on the dayside hemisphere, resulting in a deep blue colour in the visible wavelength regime. A recent study of the Kepler planets through their secondary eclipse depth confirms the general trend of relatively low albedos for most of the hot Jupiters (Angerhausen et al. 2014). Though their data seem to show a division between high albedos (above 0.12) and low albedos (below 0.08), no correlation is found with any system parameters within these groups.

1.5 Temperature structure

The global temperature structure of hot Jupiters is largely governed by the efficiency at which heat is transported from the permanent heated dayside of the planet to the colder nightside. The response of the planet's atmosphere to stellar irradiation depends on the ratio of radiative timescales, the time between absorption of stellar irradiation by the atmosphere and the emission as IR radiation, to advection timescales, the time taken to transport energy from the dayside to the nightside of the planet (e.g. Seager et al. 2005; Showman et al. 2008). If the radiative timescale is much longer than the advection timescle then the heat will be effectively transported to the nightside of the planet, essentially homogenising the atmosphere. However, if the radiative timescales are shorter than that of advection then the hot dayside will re-radiate the energy before being transported to the nightside, producing a large temperature contrast between the two hemispheres.

Knutson et al. (2007b) constructed the first temperature 'map' of an exoplanet atmosphere from phase curve observations of the hot Jupiter HD 189733b using the

Spitzer IRAC 8.0 µm channel. From observations starting just before transit to just after secondary eclipse, they were able to estimate the brightness temperature for 12 longitudinal strips on the surface of the planet, and find an offset in the atmospheric hot-spot eastward from the sub-stellar point by 30°, with a temperature difference of ∼350 K compared to that of the coldest slice. The observed temperature structure of HD 189733b suggests that the radiative timescale slightly exceeds that of advective timescales at the observed altitudes. This likely indicates the presence of winds in the atmosphere transporting the heat and effectively offsetting the hot-spot.

Recent phase curve observations of the hot Jupiter WASP-43b (Stevenson et al. 2014c, see Fig. 1.4.1) find that the planet's atmosphere efficiently redistributes heat from the dayside to the nightside of the planet. Perez-Becker & Showman (2013) predict that heat transport in hot Jupiter atmospheres is governed by wave-like processes similar to that observed in Earth's atmosphere. Following this, the atmosphere of WASP-43b displays characteristics that imply a radiative timescale shorter than that of the dynamical timescale at the altitudes probed by this measurement, which would effectively transport heat away from the hotspot of the planet before being re-radiated out of the atmosphere. Spectroscopic measurements of the phase curve reveal an atmosphere dominated by H_2O emission (Kreidberg et al. 2014a).

Absorbers in the upper atmospheres of highly irradiated exoplanets can have a significant effect on the temperature-pressure (T–P) profile, where the presence of some species, such as TiO and VO are likely to cause strong temperature inversions in the atmosphere. These molecules, which can be inferred by absorption in the optical, will trap heat in the atmosphere at high altitudes impacting the planets T–P structure. Photometric measurements across the IR with *Spitzer* IRAC have been used to infer the presence of thermal inversions in the atmospheres of hot Jupiter exoplanets when the change in flux measured in the 4.5µm band exceeds that measured in the 3.6µm bandpass (Knutson et al. 2007b).

A thermal inversion occurs when the opacity of the atmosphere in the UV and optical exceeds that in the IR. This causes radiation to be absorbed at high altitudes without being re-radiated out, heating a region in the upper atmosphere to higher temperatures than deeper down (Madhusudhan & Seager 2010). One of the first *Spitzer* secondary eclipse observations conducted on HD 209458b suggested the presence of a thermal inversion in the planets atmosphere, where models invoked a thermal inversion layer to fit the data (Knutson et al. 2008; Burrows et al. 2007; Madhusudhan & Seager 2009). However, a recent re-analysis of this data was conducted by Diamond-Lowe et al. (2014) showing that there is no need to invoke a thermal

inversion in the atmosphere to explain the data. In addition to this analysis, the evidence for thermal inversions invoked from IRAC photometric data has been put to debate for some time. For example, the evidence for a thermal inversion in the atmosphere of XO-1b (Machalek et al. 2008) is potentially explained by a super-solar C/O ratio (Madhusudhan 2012), and the two hot Jupiters TrES-2b and TrES-4b were thought to host thermal inversions (Knutson et al. 2010) yet were later found to be more consistent with models without thermal inversions (Madhusudhan & Seager 2010).

Ultimately, to resolve the issues encountered when comparing observational data to models, higher resolution spectroscopic data across multiple wavelength regimes are needed. Current observations with HST/WFC3, and future observations with the eagerly awaited James Webb Space Telescope (JWST), will likely help with disentangling the degeneracies encountered thus far.

1.6 C/O ratio

Out of all molecular species expected in hot Jupiter atmospheres H_2O is by far the most spectroscopically dominant species, and is a key molecule for constraining hot Jupiter atmospheres. In most lower atmosphere models of hot Jupiters, H_2O is well mixed throughout the atmosphere, and most of the features between 0.7 and 2.5 µm come from the H_2O vibration-rotation bands (Brown 2001). Planetary atmospheres dominated by molecular hydrogen are also expected to have CO or CH_4 as the primary carbon carrier at the high temperatures observed for hot Jupiters, unless the planet has a very high metallicity (Lodders & Fegley 2002).

It is predicted that the C/O ratio plays a pivotal role in the relative abundances of H_2O and the other spectroscopically important molecules (CH_4, CO, CO_2, C_2H_4, and HCN) in the atmospheres of close-in giant planets (e.g. Seager & Sasselov 2000; Madhusudhan 2012). Moses et al. (2013a) have analysed transit and eclipse observations of a number of transiting hot Jupiters, finding that some extrasolar giant planets could have unexpectedly low abundance of H_2O due to high C/O ratios. Atmospheres with solar elemental abundances in thermochemical equilibrium are expected to have abundant water vapour, and disequilibrium processes like photochemistry are not able to deplete water sufficiently in the infrared photosphere of these planets to explain the observations (see Moses et al. 2013a and references there in). Extinction from clouds and hazes could also significantly mask absorption signatures of water; however, this would also mask other molecular species making emission spectra appear more like

a blackbody (Fortney 2005; Pont et al. 2013). It is therefore predicted that in hot planetary atmospheres with a C/O abundance of less than one, H_2O and CO become increasingly significant, while CH_4, HCN, and C_2H_4 gain significantly in abundance when the C/O ratio is greater than one.

The C/O ratio can constrain the physical properties of the protoplanetary disk in which the planet formed, and the planet's location within the disk. The measured abundance of H_2O in the planet's atmosphere is therefore vitally important to constrain not only the overall chemistry of the atmosphere, but also the planet's formation history.

H_2O features are very difficult to measure with ground-based telescopes due to confusion with water vapour signatures from the Earth's atmosphere. Space-based observations are therefore essential to probe such spectral regions in exoplanetary atmospheric studies. A variety of exoplanet investigations have been conducted at IR wavelengths, probing the CO, H_2O and CH_4 absorption bands (Brown 2001). HST/WFC3 IR observations at 1.1–1.7 µm probe primarily the H_2O absorption band at 1.4 µm. This region can also show if optical features such as Rayleigh-type scattering due to haze in the upper atmosphere continue into the IR region (Gibson et al. 2012). Water vapour has been reported from a transmission spectrum of HD 189733b at 1.9 µm by Swain et al. (2008) using HST/NICMOS, WFC3's predecessor, corroborating a previously resolved feature from *Spitzer* IRAC (Infrared Array Camera) by Tinetti et al. (2007). Subsequent observations with NICMOS, WFC3, and *Spitzer*, however, have failed to reproduce these results (Sing et al. 2009; Désert et al. 2009; Gibson et al. 2012). There are strong wavelength-dependent intra-pixel and pixel-to-pixel variations in the NICMOS data, causing systematic errors in the light curves as the spectra move on the detector during transit observations. Re-analysis of NICMOS data by Gibson et al. (2011), Crouzet et al. (2012), and Waldmann et al. (2013) show larger errors than previously reported with a strong dependence on the data analysis methods and underlying assumptions used, showing that extracting planetary spectra from high signal-to-noise transit observations is at the limit of NICMOS' capability.

HST/WFC3 has since provided low resolution transmission spectra for a wide range of exoplanets over the 1.4 µm H_2O absorption feature (e.g. Deming et al. 2013; Mandell et al. 2013; Wakeford et al. 2013; McCullough et al. 2014). Recent observations from HST/WFC3 by Kreidberg et al. (2014a) compare the measured the relative H_2O abundance in the atmosphere of WASP-43b, deriving consistent measurements from both transmission and emission spectra. They compare the measured H_2O abundance with the solar system giant planets using the metallicity expected for

a 'broadly' solar case, indicating that the trend observed in the metal abundance of the solar system giant planet atmospheres, i.e. decreasing metal enhancement with increasing mass, extends out to exoplanet atmospheres.

The emission spectra can potentially provide vital information on the C/O ratio of planetary atmospheres, differentiating between CO and CH_4 emission. Madhusudhan et al. (2011) find $C/O \geq 1$ for WASP-12b for an atmosphere abundant in CO, and depleted in H_2O and CH_4. A majority of reductions of exoplanet atmospheres use solar abundance models, $C/O = 0.56$, limiting the parameter space available for comparative interpretations. Sing et al. (2013) have since found that the atmosphere of WASP-12b is dominated by small particle clouds. This compromises the cloud-free retrieval analysis and could be responsible for the low IR H_2O abundances.

The transmission and emission spectra therefore need to be used in combination to infer the chemistry and composition of the atmosphere. Features observed or obscured in transmission lend clues as to the presence of clouds or hazes informing the retrieval of relative abundances and temperatures from the emission spectra.

1.7 Clouds

Clouds are notoriously difficult to model in atmospheres as they introduce a vast number of free variables to the model parameters, as well as additional scattering by cloud particles which complicates the radiative transfer solutions. The presence or absence of clouds in the atmosphere can have strong implications on the total energy budget of the the planet, as they can have a large effect on the absorption properties of the observed photosphere (Sánchez-Lavega et al. 2004). Cloud formation is assumed to occur whenever the partial pressure of the atmosphere exceeds the saturation vapour pressure.

Clouds and hazes in exoplanetary atmospheres can have a strong effect on the emerging spectra. As a principal source of irradiative scattering, their presence increases the reflected flux in the visible and near-infrared regions of the spectrum (Sudarsky et al. 2003). In addition, significant absorption features can be present (Morley et al. 2014). In principle, clouds and hazes can be the result of condensation chemistry or be photochemically produced. The solar system giant planets are likely dominated by photochemical stratospheric hydrocarbon hazes (Nixon et al. 2010) produced in a similar way to tholins in the atmosphere of Titan (Khare et al. 1984). The strong UV flux on the upper atmosphere of hot Jupiter exoplanets may generally enhance photochemically generated hydrocarbon species. However, studies

by Liang et al. (2004) have found that the abundance of hydrocarbons in close-in giant planet atmospheres may be significantly less than found in Jupiter and Saturn, where the high abundance of hydrocarbon aerosols results in strong absorption features shortwards of 600 nm. The presence of non-equilibrium photochemical species with absorption in the blue gives their atmosphere a characteristic red colour (Zahnle et al. 2009). The planetary albedo, for instance the observed blue albedo measurement of HD 189733b (Evans et al. 2013), could help differentiate between strong Rayleigh scattering dust and red tholin-like species.

Due to the high temperature of hot Jupiter atmospheres, it is predicted that high temperature condensates such as iron and silicates will be present (Seager 2010). The location and composition of clouds observed in planetary atmospheres can be estimated by observing the point at which the condensation curve of a particular species crosses the cloud-free model T–P profile of the atmosphere. Figure 1.7.1 shows the condensation curves of different species expected in the atmospheres of hot Jupiter exoplanets against the modelled T–P profile of HAT-P-1b. From this it can be seen that while we would not expect the colder species condensates to form clouds in an atmosphere such as HAT-P-1b's, we would expect clouds of the hotter species, such as $MgSiO_3$ or Fe, to form. Silicate condensates are expected to dominate in hotter atmospheres, like those observed for cool brown dwarfs, while in cooler atmospheres Na_2S is expected to play a significant role in the condensation chemistry (Morley et al. 2012).

Cloud composition and formation modelling for exoplanet and brown dwarf atmospheres show a number of different approaches to seed particle growth and transport. Models from Helling et al. (eg. Helling 2007; Helling 2009a; Helling 2009b) primarily use the top-down approach, which follows seed particle growth as it drops through the atmosphere accumulating condensates and accounts for the micro-physics of the grain growth. Ackerman & Marley (2001) models consider the implications of downward transport of particles by sedimentation, balanced by upward mixing of vapour and condensates, in turn describing a mean global cloud in one dimension. As a result, these two different approaches predict different cloud compositions for exoplanet atmospheres; only with more comparative studies and observations can differentiation between such models be performed.

Recent studies of hot Jupiters have revealed that many of the exoplanets observed in transmission have cloudy or hazy properties, with their spectra dominated by strong optical Rayleigh and / or Mie scattering from high-altitude aerosol particles

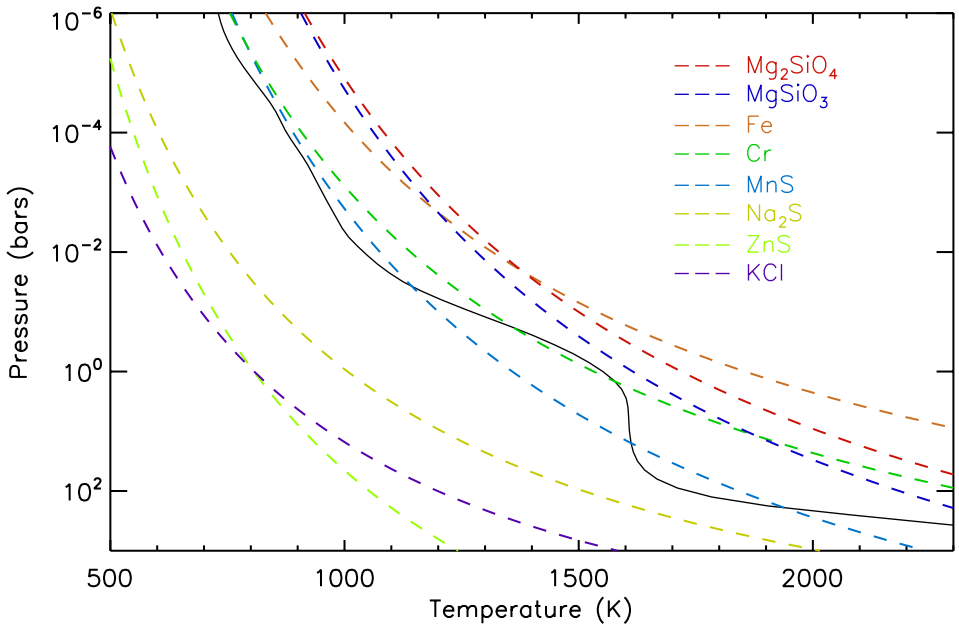

Figure 1.7.1: Condensation curves computed following the equations outlined in Visscher et al. (2010) and Morley et al. (2012) for a series of condensates expected to form clouds in exoplanet atmospheres. A planetary-averaged T–P model profile of HAT-P-1b (Fortney et al. 2010) is overplotted to show the condensate clouds expected to form at different pressures in the atmosphere.

(Pont et al. 2007; Sing et al. 2009; Sing et al. 2011b Pont et al. 2013; Sing et al. 2013; Gibson et al. 2013). Clouds and hazes in the optical range effectively obscure any features from the deeper atmosphere, including pressure-broadened Na and K lines and, in some cases, mute or completely cover expected water absorption features in the near infrared. Broadband transmission spectra of exoplanets, such as WASP-12b and HD 189733b, show strong scattering in the optical to near-infrared region of the spectrum (Redfield et al. 2008; Huitson et al. 2012). HD 189733b is one of the most extensively studied exoplanets to date, and in transmission the atmosphere is dominated by Rayleigh scattering over the whole visible range well into the infrared (Pont et al. 2013). We later use this planet as an example atmosphere to investigate the role of cloud condensates in the observed transmission spectral properties of hot Jupiter exoplanets.

1.8 Chapter overview

This thesis is in two parts. In Chapter 2 we outline a new method for observational analysis of HST near-IR transit lightcurves to obtain atmospheric transmission spectra for hot Jupiter exoplanets. We then apply this new method in Chapter 3 to five already studied hot Jupiter exoplanet atmospheres using the available HST/WFC3 transit data and perform a comparative study of the features present in the different transmission spectra. We also perform a range of tests on WFC3 data to investigate the robust nature of the observations and analysis.

In Chapters 4 and 5 we discuss the impact of clouds in the atmospheres of hot Jupiter exoplanets, extending the observable transmission spectrum into the infrared, where JWST will make new observations in the coming decade. These chapters follow a theoretical study of the different condensates expected to form clouds in these atmospheres and use Mie theory to compute synthetic transmission spectra for the well-studied hot Jupiter HD 189733b.

We then end in Chapter 6 with conclusions drawn from both observational and theoretical studies, and discuss plans for future work in Chapter 7.

1.9 Statement of contribution to publications

Some of results presented in this thesis have been previously published in peer reviewed journals where I have either been lead- or co-author. At the top of each chapter we present a statement of content identifying the published work relevant to

the chapter that follows. We also outline these here for completeness.

Sections of Chapter 2 and 3 have been previously published by MNRAS as part of publications containing analysis of HST Large Programme GO 12473, P.I. Sing WFC3 G141 IR observations. One of these papers, Wakeford et al. 2013, is led by the author of this thesis, analysing the near infrared transmission spectrum of HAT-P-1b. Additional results and analysis are presented from Sing et al. (2015) where I acted as the second author conducting the analysis of WASP-31b transmission spectral extraction and analysis. Other work in Chapter 3 on the analysis of WASP-17b has not yet been published; however, it will likely appear in an article lead by G. Ballester in the near future.

Chapters 4 and 5 are based on the published work of Wakeford & Sing (2015), of which I was the lead author, where I conducted the full analysis and write-up with support of my PhD supervisor D. Sing.

You know what the issue is with this world? Everyone wants some magical solution for their problems and everyone refuses to believe in magic.

JEFFERSON / MAD HATTER
Once Upon a Time

2

WFC3 Spectroscopic Analysis

Sections of this chapter have been previously published by MNRAS as part of publications containing analysis of HST Large Programme GO 12473, P.I. Sing WFC3 G141 IR observations Wakeford et al. (2013), and Sing et al. (2015).

Wide Field Camera 3 (WFC3) is a fourth generation imaging instrument that was installed on the Hubble Space Telescope (HST) by the crew of STS-125 as part of the Fourth Servicing Mission (SM4) in 2009. WFC3 has both photometric and spectroscopic capabilities from the UV to near-IR.

We use WFC3's IR channel to observe the stellar spectrum of exoplanet host stars during a single transit to measure the transmission spectrum of different hot Jupiter atmospheres. Using the IR G141 grism, which has a wavelength range from 1.1 to 1.7 µm, we detect the presence of water in hot Jupiter atmospheres, where H_2O vibro-rotational bands produce absorption signatures centred at 1.4 µm.

In this chapter we outline the method used to analyse our target star spectra across the different observing modes available with HST. Previous publications of WFC3 transit datasets have used a wide range of reduction and analysis methods, making comparisons between datasets and planetary atmospheres difficult (e.g. Gibson et al. 2012; Berta et al. 2012; Swain et al. 2013; Mandell et al. 2013; Wakeford et al.

2013; Stevenson et al. 2014a; Kreidberg et al. 2014b). Here we develop and discuss an analysis pipeline, which is applied to a number of datasets allowing for a true comparative study of WFC3 exoplanet transmission spectra across the expected water band.

2.1 WFC3 IR channel

The IR channel of WFC3 replaced some of the capabilities of the Near-Infrared Camera and Multi-Object Spectrometer (NICMOS) cameras. Although the standard WFC3 configuration is not particularly efficient for high S/N time series data, as buffer dumps are long and the PSF covers very few pixels (low S/N per exposure), the instrumental systematics are noticeably lower than for NICMOS as WFC3 does not suffer from strong intra-pixel sensitivities. WFC3 also has a factor of two improvement in sensitivity over NICMOS with a much higher throughput and lower read noise (e.g. WFC3 Instrument Handbook).

The WFC3 IR channel consists of a 1024×1024 pixel Teledyne HgCdTe detector that can be paired with any of 15 filters or two low-resolution grisms (Dressel et al. 2010). The infrared channel has a field of view of 136×123 arcseconds with a pixel scale of 0.13 arscec/pixel and a wavelength range from 0.8–1.7 µm. Each exposure is compiled from a number of samples (NSAMP) of non-destructive reads from either the full array or a subarray.

We use the G141 grism, or stepped prism, to measure our target spectra from 1.1 to 1.7 µm over the period of a single planetary transit. The grism produces the zeroth, 1st, and 2nd order spectrum of the target star, which can be restricted on the detector by using smaller subarray fields. Here we outline the different observing modes that can be used, list the methods currently used to analyse and de-trend WFC3 transit datasets, and put forward a new analysis pipeline to be used for a true comparative study between observations.

2.2 Observing modes

WFC3 has two observing modes that are commonly used for transiting exoplanet spectra: stare mode and spatial scanning mode (see Fig. 2.2.1). Stare mode maintains a constant pointing of the telescope throughout the observation, maintaining the same pixel position on the detector. Stare mode is used for a majority of HST observations and is useful when observing dimmer target stars where the photon

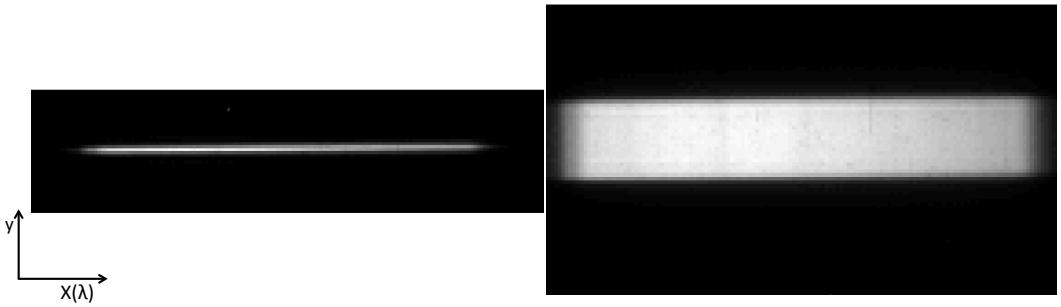

Figure 2.2.1: Left: Stare mode exposure of WASP-17 with an exposure time of 12.795 seconds and a peak pixel count of ∼64,000. Right: Spatial scan mode exposure of WASP-31 with an exposure time of 134.35 seconds with a peak pixel count of ∼38,000. Spatial scan mode allows for 10× the number of photons to be collected per exposure without being limited by the detectors non-linear regime at high count/pixel levels. The axis indicate the cross-dispersion direction (y) and the dispersion direction (x) which is measured in terms of wavelength.

counts/pixel/second is low; observing brighter targets in this mode leads to saturation. Spatial scanning mode was made available on WFC3 in Cycle 19 (2012) and is now implemented as the main mode of observations for transiting exoplanets, as targets observed for atmospheric follow-up with such instruments often orbit brighter target stars (V magnitudes brighter than 11). WFC3 spatial scanning involves nodding the telescope during an exposure to spread the light along the cross-dispersion axis, y, resulting in a higher number of photons by a factor of ten per exposure while considerably reducing overheads. This also increases the time of saturation of the brightest pixels, which allows for longer exposure times (McCullough 2011).

Spatial scanned data can be acquired using a number of different methods. A recent method that is being used for WFC3 observations involves both forward and reverse scan exposures. The spectrum is spread in the forward direction (bottom to top) for the odd exposures and spread in the reverse direction (top to bottom) for the even exposures, removing the need to reset the observation to the original position. Forward/reverse scan observations slightly increase the duty cycle; however, they also result in an offset in the count rate for each direction of the scan, which is suggested to be caused by the order in which the columns are read out from the detector (Knutson et al. 2014).

The original spatial scan technique used in WFC3 observations applied only forward scanning, which results from slewing the telescope during the course of the exposure in the forward direction, resetting the position to the start and repeating the forward slew from bottom to top for the subsequent exposures. In this thesis we discuss the use of forward-scan-only observations and discuss the techniques used to

extract and analyse each exposure spectrum.

2.3 Spectral extraction

For each of the exposures, a spectral extraction box is cropped out of the original image covering an extended region in the x-direction either side of the spectral trace and an approximately equal extended region above and below the exposed target spectrum (see Fig. 2.2.2). To extract the target spectrum from each of the exposure images we developed a custom *IDL* routine, similar to *IRAF*'s *APALL* function, to sum all of the counts across the exposed pixels. The routine, *spextract*, uses a computed centring profile and optimised aperture size to determine the exposure window for each individual target spectrum.

2.3.1 Centring profile

For stare mode observations, the centering profile is calculated using a simple Gaussian fit over the target spectral trace in the cross-dispersion direction for each pixel column of the exposure image. The central peak of the Gaussian fit is used as the centre point of the spectrum for that pixel column and placed in an array. Spatially scanned exposure images, however, do not follow a Gaussian profile. For these datasets we set a hard limit on the edge of the spectral trace in the form of a count value in the cross-dispersion direction, ∼100–200 e^-/s. The centre is defined as the central pixel between the top- and bottom-most pixel in the image cross-dispersion direction with this count value.

The central trace often reveals sub-pixel variations in the cross-dispersion direction of the spectrum (see Fig. 2.2.2). These small changes have negligible effect on the resultant spectral extraction and a fixed central pixel position is used for further analysis. However, if larger position offsets are traced where multiple pixel shifts are observed across the spectrum, the centring profile is used in each pixel column for the subsequent aperture determination.

2.3.2 Aperture determination

To determine the optimum number of pixels in the cross-dispersion direction to include as part of our exposed target spectrum, we determine the best-fitting aperture size across all exposures. Using an array of 11 different aperture sizes around the central profile, we sum up the total counts in the cross-dispersion direction for each pixel

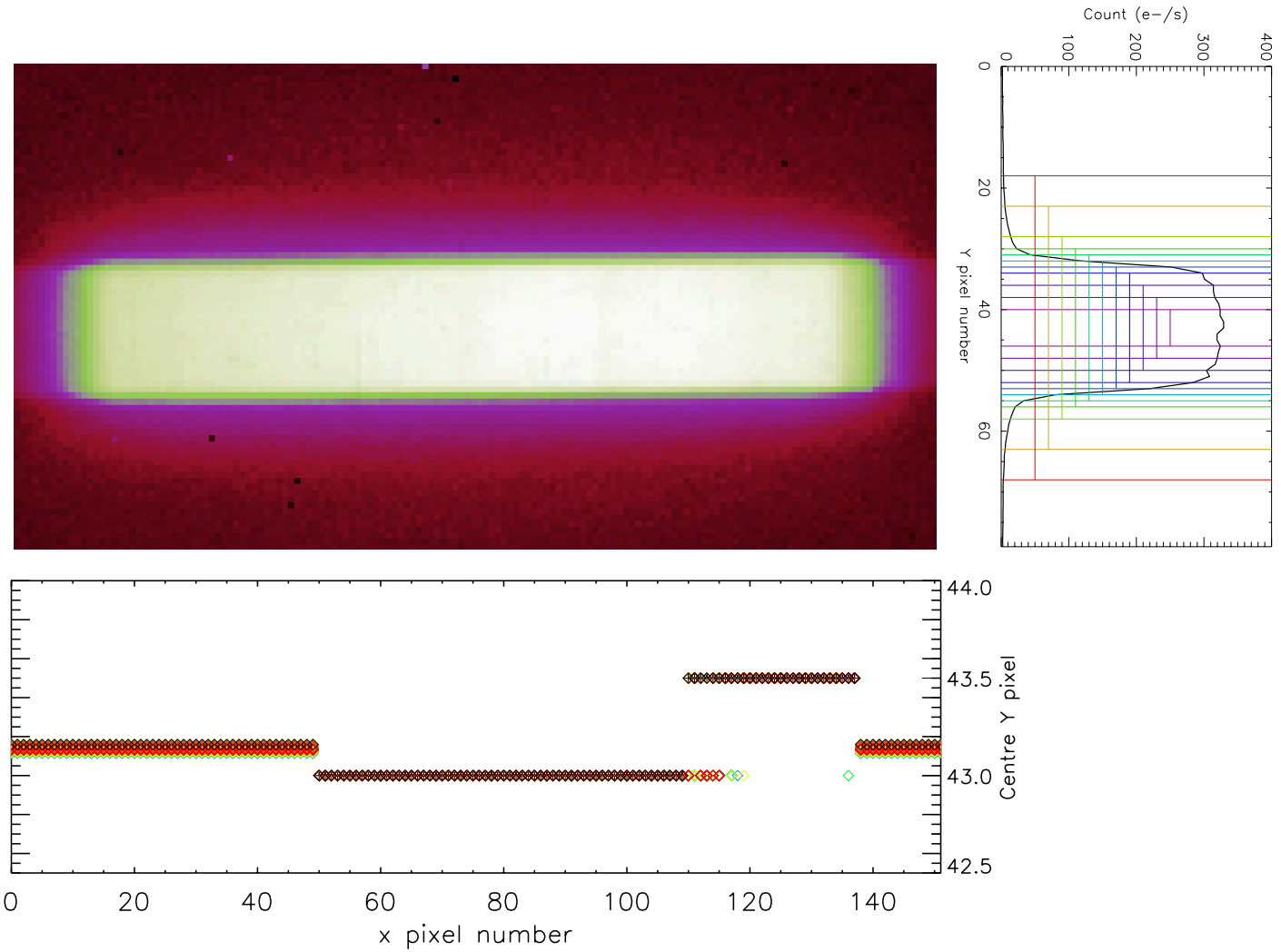

Figure 2.2.2: Top left: Example exposure in spatial scan mode of WASP-31. Right: A series of aperture sizes tested across the spectral trace in the cross-dispersion direction. Bottom: The centring profile determined by the mid-point between fixed count values on the exposure image.

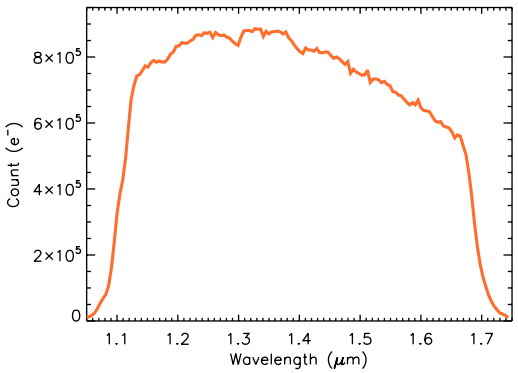

Figure 2.3.1: Stellar spectrum of WASP-31 extracted from HST WFC3 spatial scan exposure. Background correction is applied using a clean region of the detector offset in the cross-dispersion direction from the target spectral trace (see § 3.2.2).

column in the array. An example of the apertures used is shown in Fig. 2.2.2. We then have an array of target spectra at each of the 11 aperture sizes for each exposure image.

To determine the optimum aperture covering our target spectrum across all exposures in the observation, we minimise the standard deviation of the residuals across the whole observation after removing the transit. This is done by summing up the total counts across the aperture spectrum for each exposure in the timeseries. We divide this by a standard transit model to produce an array of residuals. For each of the apertures that are being tested on the dataset we calculate the standard deviation of the residual array and select the aperture size that minimises the scatter. The optimum aperture is often slightly wider than the apparent spread of the spectrum on the detector, which often also accounts for any sub-pixel deviations in the centring profile, ensuring that all available target photons are used in the analysis.

Once the spectra have been extracted at the optimum aperture, they need to be corrected for the background count so that only the target remains.

2.3.3 Background correction

To correct for any background counts on the detector not from our target star, we extract a clean region of the original WFC3 subarray exposure image to measure the count level. We attempt to use a background region over the same wavelength pixels as the target spectral trace and offset in the cross-dispersion direction. Using the same aperture size optimised for our target spectra we sum the background count over the same range in our clean background region.

For spatially scanned images where the spectral trace covers over half of the subarray field (see § 3.2.4), it is not possible to use a background region occupying the

same wavelength space on the detector as the spectral image. The background is computed using the edges of the spectral trace and fit with a linear function to obtain an average background count level across the whole spectrum.

2.3.4 Wavelength calibration

Wavelength calibration is conducted for each WFC3 dataset using a filter image of the target star obtained either before or after the spectral observations of the planetary transit are conducted. Calibration images for WFC3's IR channel are conducted using a F139M narrow band filter to obtain the absolute reference position of the target star on the detector ($X_{\rm ref}$, $Y_{\rm ref}$). The filter choice for the calibration image is not important, as it is used only to determine the position of the undispersed stellar image on the detector for the wavelength solution. To calculate the wavelength corresponding to each pixel along the x-direction, we applied a linear fit to the wavelength solution. The wavelength solution is a function of the $X_{\rm ref}$ and $Y_{\rm ref}$ position given by $\lambda(x) = a0 + a1 \times X_{\rm ref}$ and,

$$\lambda(pixel) = \lambda(x) \; + \; (Y_{\rm ref\_dispersion} \times X_{\rm Pixel}) \tag{2.1}$$

where $\lambda(x)$ is the wavelength of the spectra along the x-axis, $X_{\rm ref}$ is taken from the filter image, $a0$ and $a1$ are taken from Table 5 in Kuntschner et al. (2009), and $Y_{\rm ref\_dispersion}$ is found in Figure 6 of Kuntschner et al. (2009) using the $Y_{\rm ref}$ position from the filter image.

We assume that all of the pixels in the same column have the same effective wavelength. However, the position of the spectrum in the wavelength direction on the detector does change over the course of the observations, often at the sub-pixel level. To account for this shift we cross-correlate all of our spectra and calculate the shift needed to align all of the spectra. This shift in wavelength is also later used to correct for any correlated systematic trends in the data related to the change in position on the detector. In § 3.1.1 we discuss the correlation between wavelength shift and systematics in the observations for each of the five planet datasets analysed in this thesis, and their effects on the calculated transmission spectra.

2.4 White lightcurve

Prior to evaluating the transmission spectrum (from transit lightcurves in small spectral bins), we analyse the light curves summed over the entire wavelength range.

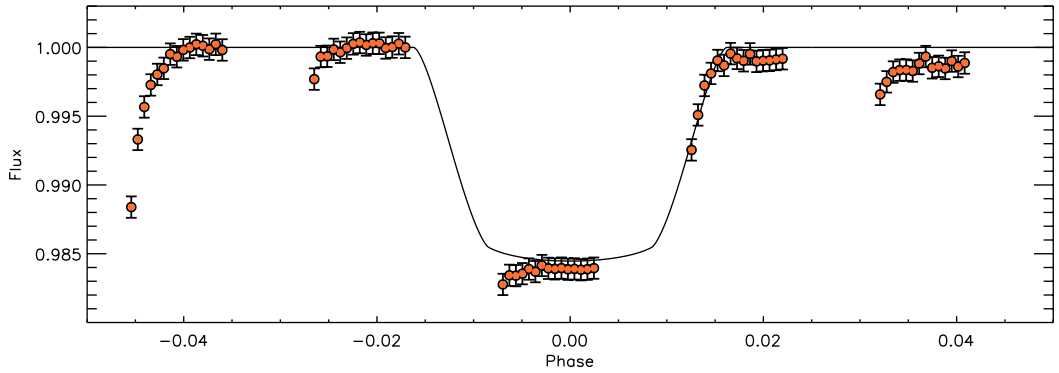

Figure 2.4.1: The white lightcurve of WASP-31 during a single transit observed over 5 HST orbits. It can be seen that the first orbit of HST observations after target acquisition is subject to non-repeated systematics in the subsequent orbits.

The white lightcurve is often used to improve the general system parameters and quantitatively investigate any instrumental systematics.

We calculate the white lightcurve by summing up the total flux of each exposure spectrum across the entire wavelength range. Figure 2.4.1 is an example white lightcurve of WASP-31 observed with HST WFC3 during a single transit of the orbiting hot Jupiter exoplanet WASP-31b. Noticeably there are significant gaps in the data; due to HST orbiting behind the Earth once every orbit. This results in ∼45 minute periods of observation and ∼45 minute gaps in each HST orbit. To fully cover the transit of most hot Jupiter exoplanets with HST, 4–5 orbits of data are required. This also gives a substantial observing window either side of the planetary transit to obtain an accurate baseline flux measurement of the star. The first orbit of HST observations after initial acquisition of the target is subject to non-repeated systematics in the subsequent orbits and is often excluded from further analysis (e.g. Brown et al. 2001; Sing et al. 2011b).

For our datasets we used the white lightcurve to obtain the planet-to-star radius ratio (R_p/R_*) and centre of transit time prior to evaluating individual spectroscopic lightcurve channels by fitting a Mandel & Agol (2002) transit model created with non-linear limb-darkening parameters to our data using the *IDL* code *MPFIT* (see §2.4.1). Due to the limited phase coverage of the HST transit observations, when fitting the white lightcurve for R_p/R_* we fix the system parameters such as inclination and a/R_* using previously published results as further constraints cannot be placed with these datasets.

The white lightcurves also display systematics from the instrument, which show

wavelength independent and/or time and position dependent parameters. Currently a variety of systematic models are being applied to WFC3 transit data to account for these systematics, making comparison between planetary spectra difficult. In § 2.5 we discuss each of the current models used, with each of the programs and publications associated with them listed in Table 2.5.1.

To evaluate the systematics we observe in our data we put forward a new method of marginalisation to determine the best-fitting systematic model in each dataset and evaluate the effects on the resultant desired system parameters (see § 2.6).

2.4.1 Transit model

A transit lightcurve consists of N stellar flux measurements observed at time t, collectively referred to as the data D or the lightcurve. To model each of the lightcurves we calculate a Mandel & Agol (2002) transit model following a non-linear limb-darkening law (see §2.4.2) with an initial planet-to-star radius ratio, inclination, and a/R$_*$ defined by previously published values. The model is then fit to the data by allowing the baseline flux, planet-to-star radius ratio, and centre of transit time to vary, while fixing the other planetary system parameters. We use the IDL routine MPFIT, which operates a Levenberg-Marquardt least-squares minimisation algorithm (L-M), to determine the best-fitting parameters for each dataset.

2.4.2 Limb-darkening

To accurately model the transit light curves, stellar limb darkening has to be carefully considered. In an effort to keep the comparative analysis as consistent as possible we fit the Mandel & Agol (2002) transit model to the individual transit datasets using the non-linear limb-darkening coefficients calculated using 1D Kurucz stellar models, even where more complete 3D limb-darkening models are available (e.g. HD 209458 from Hayek et al. 2012). The coefficients were calculated following Sing (2010) using a non-linear limb-darkening law given by

$$\frac{I(\mu)}{I(1)} = 1 - \sum_{n=1}^{4} c_n (1 - \mu^{\frac{n}{2}}), \tag{2.2}$$

where $I(1)$ is the intensity at the centre of the stellar disk, $\mu = cos(\theta)$ is the angle between the line of sight and the emergent intensity, and c_n are the limb-darkening coefficients. The Kurucz stellar models are additionally dependent on the stellar metallicity and stellar effective temperature.

2.5 Systematic model correction

One of the issues encountered when analysing observational datasets is determining the impact that instrumental systematics have on the resultant measurements. Since the advent of WFC3's application to transiting exoplanets, a number of systematic models have been used to reduce G141 spectroscopic data, which are listed in Table 2.5.1.

Figure 2.5.1 shows three examples of systematic trends observed in WFC3 transit lightcurves: "HST breathing" effects, visit-long slopes, and the 'hook' effect. The "HST breathing" effect shown in Fig. 2.5.1a displays a periodic systematic across each orbit of data. This is attributed to the known thermal variations which occur during the orbit of HST as it passes into and out of the Earth's shadow causing expansion and contraction of HST. This can be most easily seen in the middle panel in relation to the HST orbital phase. The "HST breathing" effect systematic has been noted and corrected for in multiple datasets with a variety of parametrised models (e.g. Wakeford et al. 2013; Line et al. 2013; Stevenson et al. 2014a) which remove systematics based on functions of the HST orbital time period and phase.

Many groups have also reported a visit-long trend in WFC3 lightcurves. This can be seen clearly in the raw white lightcurve of HD 209458 shown in Fig. 2.5.1b, which displays a significant slope across the entire observation period. This systematic trend has not been correlated with any other physical parameter of WFC3 observations. However, it has been shown to significantly affect the resultant system parameters obtained from the lightcurve and is thus used as a correction in each systematic model shown in Table 2.5.1.

In addition to orbital phase trends, both in planetary and HST space, a number of lightcurves have been dominated by a systematic increase in the intensity during each group of exposures obtained between buffer dumps referred to as the 'hook' effect (e.g. Berta et al. 2012; Mandell et al. 2013). The dataset in Fig. 2.5.1c clearly displays this effect in a number of datasets, and the bottom residual plot in terms of exposure number shows the highly repeatable aspect of the systematic. This is thought to be caused by charge trapping on the detector and it has been found that the 'hook' is, on average, zero when the count rate is less than about 30,000 electrons per pixel (Deming et al. 2013). In our analysis only one of our lightcurves displays this 'hook' systematic and we discuss the process used to correct for it in § 2.5.2, and again with specific reference to the planetary dataset in § 3.3.1.

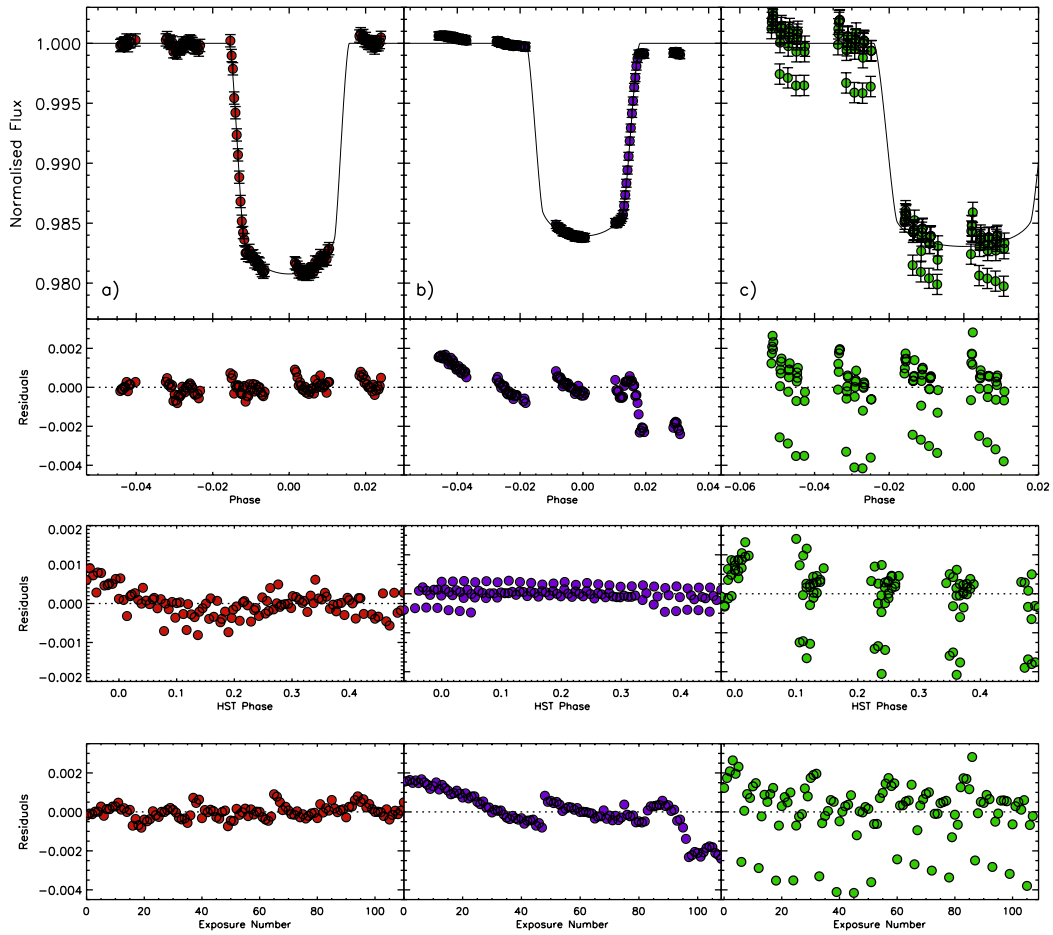

Figure 2.5.1: Three of the main systematic effects observed in HST WFC3 transit datasets: a) "HST breathing" effect caused by the temperature variations in the orbital period of HST. b) Visit-long Slope, a linear trend observed across the entire observing period for all transit lightcurves observed with HST WFC3. c) The 'hook' effect which is thought to be caused by charge trapping between buffer dumps. Lower panels show the residuals of each dataset with respect to different timeseries parameters. Top: residuals in terms of planetary phase. Middle: residuals in terms of HST orbital phase, where each HST orbit of data is overplotted on subsequent orbits. Bottom: residuals in terms of exposure number.

A combination of these systematics has been observed in all WFC3 transit datasets. We outline the main systematic models used to correct for these effects, with the full list of published systematic correction models presently used outlined in Table 2.5.1.

2.5.1 Exponential model ramp

The exponential model-ramp systematic correction was first put forward by Berta et al. (2012) as an analytical model whose parameters represent the physical processes of the instrument. The exponential models apply an exponential ramp over sets of exposures, and corrects for orbit-long and visit-long slopes. Line et al. (2013) show the exponential model-ramp in the form of the equation

$$\frac{F_{orb}}{F_{cor}} = (C + V\theta + B\phi)(1 - Re^{\psi/\tau}), \tag{2.3}$$

where F_{orb}/F_{cor} are the lightcurve residuals, θ is the planetary phase, ϕ is the HST orbital phase, and ψ is the phase over which the ramp feature occurs which accounts for the visit-long slope V, the orbit-long slope B, and a vertical offset C applied to the whole lightcurve. The exponential model for the ramp has an additional two parameters: the ramp amplitude R, and the ramp timescale τ. This is displayed as "$\theta + e^{\psi/\tau} + \phi$" in Table 2.5.1. This method is used by a number of groups when a ramp is observed in the raw white lightcurve (Kreidberg et al. 2014b; Kreidberg et al. 2014a; Knutson et al. 2014).

In cases where the orbital timescale matches the phase over which the ramp occurs a simplification of the ramp-model can be used, as seen in Stevenson et al. (2014a),

$$model = [1 + r_0\theta + r_1\theta^2] \times [1 - e^{r_2\phi + r_3} + r_4\phi], \tag{2.4}$$

where r_{0-4} are free parameters and the phase ψ over which the ramp feature occurs is now equal to the HST orbital phase ϕ. This is displayed as "$\theta + e^{\phi} + \phi$" in Table 2.5.1. Fraine et al. (2014) find that a simple linear visit-long correction and a single exponential ramp in HST phase can correct for the systematics observed in the transit lightcurve of the hot Neptune HAT-P-11 without the need for a squared term in time.

Both of these methods rely on the timescales of each ramp to be the same in each orbit and for each orbit to have the same repeating systematic. This therefore depends heavily on the scheduling of each exposure within a HST orbit, which some of our datasets do not meet.

Table 2.5.1: Table of exoplanets observed using WFC3 G141 grism, mode the data is observed in, the systematic model used to de-trend the data, author, HST program, and year of observation.

HST program	PI	Cycle	Planet	Year	Mode	Model	Paper
GO 11740	F. Pont	Cycle 17	HD 189733	2010	stare	$\mathcal{GP}$	Gibson et al. (2012)
GO 12181	D. Deming	Cycle 18	WASP-17	2011	stare	$\theta + doot + \lambda$	Mandell et al. (2013)
			HD 209458	2012	scan	θ	Deming et al. (2013)
			XO-1	2011	scan	θ	Deming et al. (2013)
			HAT-P-12	2011	stare	$\theta + e^{\psi/\tau} + \phi$	Line et al. (2013)
			WASP-19	2011	stare	$\theta + doot$	Huitson et al. (2013)
						$\theta + doot + \lambda$	Mandell et al. (2013)
			WASP-4	2010	stare	$doot$	Ranjan et al. (2014)
			TrES-2	2010	stare	$doot$	Ranjan et al. (2014)
			TrES-4	2010	stare	$\theta + doot$	Ranjan et al. (2014)
			CoRoT-1	2012	stare	$\theta + doot$	Ranjan et al. (2014)
GO 12230	M. Swain	Cycle 18	WASP-12	2011	stare	θ	Swain et al. (2013)
						$\theta + doot + \lambda$	Mandell et al. (2013)
						$\theta + \phi^N$	Sing et al. (2013)
						$\theta + e^{\psi/\tau} + \phi$	Stevenson et al. (2014c)
GO 12251	Z. Berta	Cycle 18	GJ 1214	2010	stare	$doot$	Berta et al. (2012)
GO 12449	D. Deming	Cycle 19	HAT-P-11	2012	scan	$\theta + e^{\phi}$	Fraine et al. (2014)
GO 12473	D. Sing	Cycle 19	WASP-31	2012	scan	$\theta + \phi^N + \lambda^N$	Sing et al. (2015)
			HAT-P-1	2012	scan	$\theta + \phi^N$	Wakeford et al. (2013)
GO 12881	P. McCullough	Cycle 20	HD 189733	2013	scan	θ	McCullough et al. (2014)
GO 13021	J. Bean	Cycle 20	GJ 1214		scan	$\theta + e^{\psi/\tau} + \phi$	Kreidberg et al. (2014b)
GO 13064	D. Ehrenreich	Cycle 19	GJ 3470	2013	stare	doot	Ehrenreich et al. (2014)
GO 13338	K. Stevenson	Cycle 21	GJ 436	2013	scan	$\theta^2 + e^{\phi} + \phi$	Stevenson et al. (2014a)
GO 13467	J. Bean	Cycle 21	WASP-43	2013	scan	$\theta + e^{\psi/\tau} + \phi$	Kreidberg et al. (2014a)
GO 13501	H. Knutson	Cycle 20	HD 97658	2014	scan	$\theta + e^{\psi/\tau}$	Knutson et al. (2014)

$\mathcal{GP}$ - Gaussian Process; *doot* - Divide-oot; θ - Visit-long slope; ϕ - HST phase; λ - wavelength shift; $e^{\psi/\tau}$ - model ramp

2.5.2 Divide-oot method

Berta et al. (2012) suggested an additional method, called divide-oot, for correcting the systematic 'ramp' or 'hook' observed in a number of datasets. The divide out-of-transit method (divide-oot) relies on the hook systematic being "extremely" repeatable between orbits in a visit.

Divide-oot uses the out-of-transit orbits to compute a weighted average of the flux evaluated at each exposure within an orbit and divides the in-transit orbits by the template created. This requires each of the in-transit exposures to be equally spaced in time with the out-of-transit exposures being used to correct them, such that each corresponding image has the same HST phase and that additional systematic effects are not introduced. While this does not rely on knowing the relationship between measured photometry and the physical state of the camera it does require there to be an even number of exposures equally spaced from orbit to orbit where the exposures occupy the same HST phase space. This is so that the systematics induced by the known "HST breathing" trend caused by temperature variations in its orbit can be effectively eliminated. This is listed as '*doot*' in Table 2.5.1.

The divide-oot method relies on the cancellation of common-mode, wavelength independent, systematic errors by operating only on the data themselves using simple linear procedures, relying on trends to be similar in the time domain over a number of orbits. A somewhat similar technique was adopted by Deming et al. (2013) and Mandell et al. (2013) for their analysis of WFC3 data relying on common trends in the wavelength domain, we discuss this further in § 3.2.4.

2.5.3 Parametrised model

In Wakeford et al. (2013) we discuss an additional parametrisation method to correct for "HST breathing" effects in the data, which assumes that they fit a high order polynomial function rather than being exponential in nature. This method also seeks to remove the visit-long slope observed in each WFC3 transit dataset using a linear time trend in planetary phase in addition to the HST phase corrections,

$$model = T_1\,\theta + \sum_{i=1}^{n} p_i \phi^i \tag{2.5}$$

where θ is a function of planetary phase representing a linear slope over the whole visit, ϕ is a function of HST phase accounting for "HST breathing" effects, and T_1 and p_{1-n} are either free parameters or fixed to zero to fit the model to the data.

In addition to "HST breathing" trends Sing et al. (2013) found that additional functions in wavelength shift on the detector were needed to correct for systematics seen in the lightcurve of WASP-12. The systematic model then takes the form,

$$model = T_1\,\theta + \sum_{i=1}^{n} p_i \phi^i + \sum_{j=1}^{n} l_j \lambda^j \tag{2.6}$$

where λ is a function of the shift in the x-direction on the detector over the visit, and l_{1-n} are fixed to zero or free parameters, similar to that used for the "HST breathing" correction. We limit the order of the polynomial functions to a maximum of the fourth order for all further parametrised models.

This model does not require each of the orbits to have the same number of exposures, or consistent repeating systematics in each orbit or between each buffer-dump making it a robust method to apply to any transit dataset from WFC3. However, due to the large number of potential free parameters in each systematic model, and the potential to go to even higher orders of polynomial for each systematic, using this method can potentially introduce additional systematics if the correct model is not initially chosen.

2.5.4 Motivation for a new method

Determining the parameters of a transiting planet via time series observations is dependent on robustly removing any systematic effects from the telescope and detector. Each of the models used in the literature attempt to correct the array of systematics observed independently in each dataset. Studies of multiple WFC3 datasets have been conducted across multiple programs and observation modes. These have attempted to define a common de-trending technique to apply to all datasets (Deming et al. 2013; Mandell et al. 2013; Ranjan et al. 2014; Kreidberg et al. 2014b, Kreidberg et al. 2014a). However, not all datasets display the same combination of systematics, which appear to be highly dependent on the observational mode and set-up.

Mandell et al. (2013) conducted the first reanalysis test of WFC3 data for WASP-19b and WASP-12b, with the addition of the first analysis of WASP-17b. The reanalysis incorporated a new wavelength dependent systematic correction over the previous methods used (see Table 2.5.1). While this study produced almost photon-limited results in individual spectral bins, the spectral features observed in the transmission spectra were degenerate with various models of temperature and compositions making interpretation difficult. Ranjan et al. (2014) conducted a study of four stare

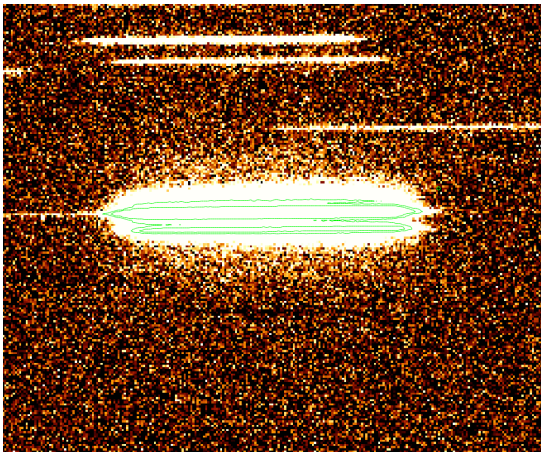

Figure 2.5.2: WFC3 ima exposure image of WASP-12, observed in stare mode. The contours indicate the peak exposure of the two overlapping spectral traces of the target star, WASP-12, and the binary companion M-dwarfs in the system.

mode WFC3 transit lightcurves from the large HST program, GO 12181. However, they were unable to resolve any features in the transmission spectrum for three of the planetary atmospheres, and were unable to extract a robust transmission spectrum for one of the datasets as different treatments to the data gave slightly different results.

Additionally, the analysis of the very hot Jupiter WASP-12b which was observed as part of GO 12230, P.I. M.Swain is a good example of differences caused from analysis techniques. WASP-12 was observed in stare mode using WFC3 G141 slitless grism which contained the spectrum of both the target planetary host star and the M-dwarf binary companions to WASP-12, which overlapped in the spectral response on the detector (see Fig. 2.5.2). The most recent reanalysis of these data explores the effect of systematic model correction on the absolute transit level measured for the atmospheric transmission spectrum (see Fig. 13 in Stevenson et al. 2014b for a direct comparison). The dependence on the systematic model used, as seen here, suggests that a new method is needed to determine the best systematic treatment of each dataset which simultaneously allows for a direct comparison to be made between multiple datasets.

Here we introduce a new method to not only incorporate the analysis of multiple systematic treatments on the lightcurve but also to be applicable to multiple datasets allowing for a cross-comparison between different transmission spectra.

2.6 Marginalisation

Thus far it is not clear which of the systematic models that have been employed to correct WFC3 transit lightcurves is the best for each individual dataset. We attempt to rectify this by performing a marginalisation over a grid of systematic models which incorporate corrections for the different systematics observed across the exoplanet transit datasets discussed earlier in this chapter.

Use of the Bayesian Information Criterion (BIC) to select between different systematic models, which takes Occam's Razor into effect by penalising models with increasing complexity, has been previously used for WFC3 observations (e.g. Wakeford et al. 2013; Sing et al. 2013; Sing et al. 2015), and has been applied to a range of datasets (e.g. Huitson et al. 2013; Crossfield et al. 2013; Nikolov et al. 2014). Here we take this one step further by outlining a method, following the formula in Gibson (2014), to marginalise over all applied models to calculate robust transit parameters. Under this approach, we effectively average the results obtained from a suite of systematics models in a principled manner. In doing so, we marginalise over our uncertainty as to which model is actually the "correct" model. Marginalisation over models allows us to quantify the degeneracy between our physical parameters of interest and our choice of systematics model. In this case we want to determine the value and associated uncertainty for R_p/R_* for each of our lightcurves after correcting for the systematics inherent in the data. For each systematic model used to correct the data we calculate the evidence of fit, defined as the probability that the data would be produced given the systematic model, which is then used to apply a weight to the parameter of interest measured using that model. A weighted average of R_p/R_* is then calculated which takes into account the individual weights of each fit and statistical likelihood of each model. This ensures that a variety of systematic models are taken into account when measuring the R_p/R_* without having to choose between models. This is especially important when several models have equally well fitting systematic models, as is often the case.

Before marginalisation, the overall systematic models that are going to contribute to the final weighting must be decided upon. For this we use a grid of 49 parametrised models which incorporate all known identified systematic trends in the data (see Table 2.6.1), with the addition of the two exponential models outlined by Stevenson et al. (2014a) and discussed in § 2.5.1, and the weighting assigned to the uncorrected lightcurve. All 52 models are then placed into an array of varying free parameters to

Table 2.6.1: Table of all parametrised systematic models applied to the lightcurves showing the combination of visit-long trends as a function of planetary phase (θ), functions of HST orbital phase (ϕ), and functions dependent on wavelength shifts (λ) in the data. In addition to these models we apply the two exponential orbital phase models outlined in Stevenson et al. (2014a) which can be seen in § 2.5.1.

No.	θ	ϕ	ϕ^2	ϕ^3	ϕ^4	λ	λ^2	λ^3	λ^4	No.	θ	ϕ	ϕ^2	ϕ^3	ϕ^4	λ	λ^2	λ^3	λ^4
0										25	√								
1						√				26	√					√			
2						√	√			27	√					√	√		
3						√	√	√		28	√					√	√	√	
4						√	√	√	√	29	√					√	√	√	√
5		√								30	√	√							
6		√				√				31	√	√				√			
7		√				√	√			32	√	√				√	√		
8		√				√	√	√		33	√	√				√	√	√	
9		√				√	√	√	√	34	√	√				√	√	√	√
10		√	√							35	√	√	√						
11		√	√			√				36	√	√	√			√			
12		√	√			√	√			37	√	√	√			√	√		
13		√	√			√	√	√		38	√	√	√			√	√	√	
14		√	√			√	√	√	√	39	√	√	√			√	√	√	√
15		√	√	√						40	√	√	√	√					
16		√	√	√		√				41	√	√	√	√		√			
17		√	√	√		√	√			42	√	√	√	√		√	√		
18		√	√	√		√	√	√		43	√	√	√	√		√	√	√	
19		√	√	√		√	√	√	√	44	√	√	√	√		√	√	√	√
20		√	√	√	√					45	√	√	√	√	√				
21		√	√	√	√	√				46	√	√	√	√	√	√			
22		√	√	√	√	√	√			47	√	√	√	√	√	√	√		
23		√	√	√	√	√	√	√		48	√	√	√	√	√	√	√	√	
24		√	√	√	√	√	√	√	√	49	√	√	√	√	√	√	√	√	√
50	$\theta \times(1 - e^{\phi}) + \phi$									51	$(\theta + \theta^2) \times (1 - e^{\phi}) + \phi$								

be fit or fixed in turn and looped over for each lightcurve fit to calculate the weighting assigned to each in turn.

It is also important to note that marginalisation relies on the fact that at least one of the models being marginalised over is a good representation of the systematics in the data. Our grid of parametrised models includes all combinations of factors up to the fourth order in both HST phase, to correct for "HST breathing" effects, and up to the fourth order in wavelength shift, in addition to the visit-long linear trend noted by all groups. By also incorporating the Stevenson et al. (2014a) exponential HST phase models, with a linear and squared planetary phase trend, we make the assumption that this condition of marginalisation is satisfied.

2.6.1 Evidence and weight

To calculate the weighting assigned to each of the systematic models and subsequently the final marginalised parameter for the planet-to-star radius ratio for each planetary transit, we first have to determine the evidence that each systematic model has when fit to the data. The evidence of fit assigned to each systematic model is given by the probability of the data D given the model q and is often referred to as the marginal likelihood. In the absence of accurate priors on which to place a likelihood, we use the approximate form of the evidence (Gibson 2014),

$$\ln E_q = \mathcal{P}(D|S_q) \approx -\frac{1}{2}\mathrm{BIC} = \ln[\mathcal{P}(D|\alpha_*)] - \frac{1}{2}M \ln N, \tag{2.7}$$

where the BIC is the Bayesian Information Criterion, which is equated to the logarithmic probability of the data given the parameter and systematic model ($\ln[\mathcal{P}(D|\alpha_*)]$) minus the number of free parameters M multiplied by the log number of data points being fit N.

Alternatively to the BIC, the lesser used Akaike Information Criterion (AIC) can be calculated, which does not penalise the model as strongly for added complexity given a large number of data points,

$$\ln E_q = \mathcal{P}(D|S_q) \approx -\frac{1}{2}\mathrm{AIC} = \ln[\mathcal{P}(D|\alpha_*)] - M. \tag{2.8}$$

As the number of data points in each dataset greatly exceeds that of the number of free parameters in our most complex model we choose to minimise the AIC to give our best-fitting model with the largest evidence. This is also favoured in Gibson (2014) as it provides a more thorough inclusion of models into the likelihood.

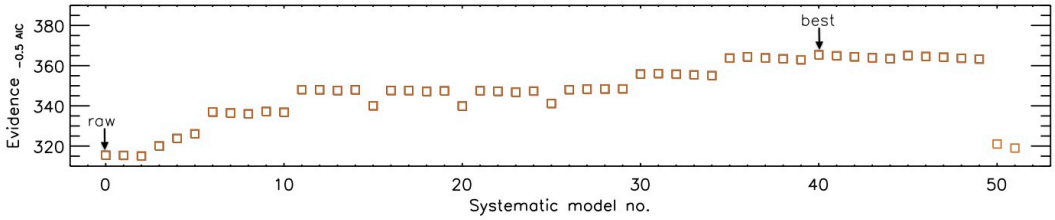

Figure 2.6.1: The evidence based on the AIC plotted against the systematic model number corresponding to Table 2.6.1. This is an example of the evidence computed for WASP-31 where the best-fitting systematic model and the raw lightcurve evidence are indicated with arrows.

The assigned evidence parameter for each model additionally relies upon the uncertainty placed on the data (σ), which is dominated by photon noise in spectral extraction pipelines. To ensure appropriate uncertainties, we start by running our systematics models with *MPFIT* and use the residual scatter to inflate our errorbars for each data point prior to marginalisation. Typically this rescales the errors by a factor of $\sim$1.1 to $\sim$1.2 times the theoretical photon noise limit of WFC3. Once we have applied this inflation to our errorbars the approximated evidence is modified to incorporate the likelihood function.

To apply this to our dataset we expand the above likelihood function,

$$\ln[\mathcal{P}(D|\alpha_*)] = \ln\left[\prod_{i=1}^{N} \frac{1}{\sigma\sqrt{2\pi}} e^{-\frac{r_i^2}{\sigma^2}}\right] \tag{2.9}$$

where σ is the uncertainty on the data, and r_i represents the model residual for the ith datapoint.

$$= \sum_{i=1}^{N} \ln\left[\frac{1}{\sigma\sqrt{2\pi}} e^{-\frac{r_i^2}{2\sigma^2}}\right] \tag{2.10}$$

$$= \sum_{i=1}^{N} \ln\left[\frac{1}{\sigma\sqrt{2\pi}}\right] - \frac{1}{2}\left(\frac{r_i}{\sigma}\right)^2 \tag{2.11}$$

$$= -N \ln\left(\sigma(2\pi)^{\frac{1}{2}}\right) - \frac{1}{2}\chi^2 \tag{2.12}$$

$$= -N \ln\sigma - \frac{N}{2}\ln 2\pi - \frac{1}{2}\chi^2 \ . \tag{2.13}$$

Substituting Eq 2.13 into Eq 2.8, we arrive at,

$$\ln E_q = -N \ln \sigma - \frac{1}{2} N \ln 2\pi - \frac{1}{2}\chi^2 - M \tag{2.14}$$

This gives us the final form of the evidence function for each of our systematic models applied to the data. This now needs to be transformed into a weighting so that each of the systematic models (S_q) is assigned a percentage of the overall probability and, when normalised, $\sum_q \mathcal{P}(S_q|D) = 1$.

The individual weight (W_q) for each systematic model is calculated by

$$W_q = \mathcal{P}(S_q|D) = E_q \,/\, \sum_{q=0}^{N_q} E_q. \tag{2.15}$$

Where N_q is the number of models fit, α_m is the marginalised parameter, and α_q is the measured parameter for each model. The weighting assigned to each model due to the evidence parameter can then be used to calculate the weighted mean of all the parameters (α) of interest

$$\alpha_m = \sum_{q=0}^{N_q} (W_q + \alpha_q), \tag{2.16}$$

and the uncertainty (σ_α) on that parameter can be determined from σ_{α_q} i.e. the uncertainty on the parameter α determined from the qth model,

$$\sigma(\alpha) = \sqrt{\sum_{q=0}^{N} (W_q[(\alpha_q - \alpha_m)^2 + \sigma_{\alpha_q}^2])}. \tag{2.17}$$

From the marginalisation over all 52 systematic models on the white lightcurve, the best-fitting model can reveal the dominant contributing systematics to each dataset. Figure 2.6.1 shows the calculated evidence based on the AIC approximation for all 52 models when fit to an example dataset, where the systematic model with the highest overall weighting for the marginalisation is indicated by an arrow along with the raw lightcurve fit. This clearly shows the sample of systematic models that are favoured when correcting this dataset and emphasises the need for through systematic model analysis. It is sometimes the case that a number of models will have a strong weighting on the white lightcurve, where their weight $> 10\%$, often these models correct for the same combination of systematic trends assigning a different order to the polynomial

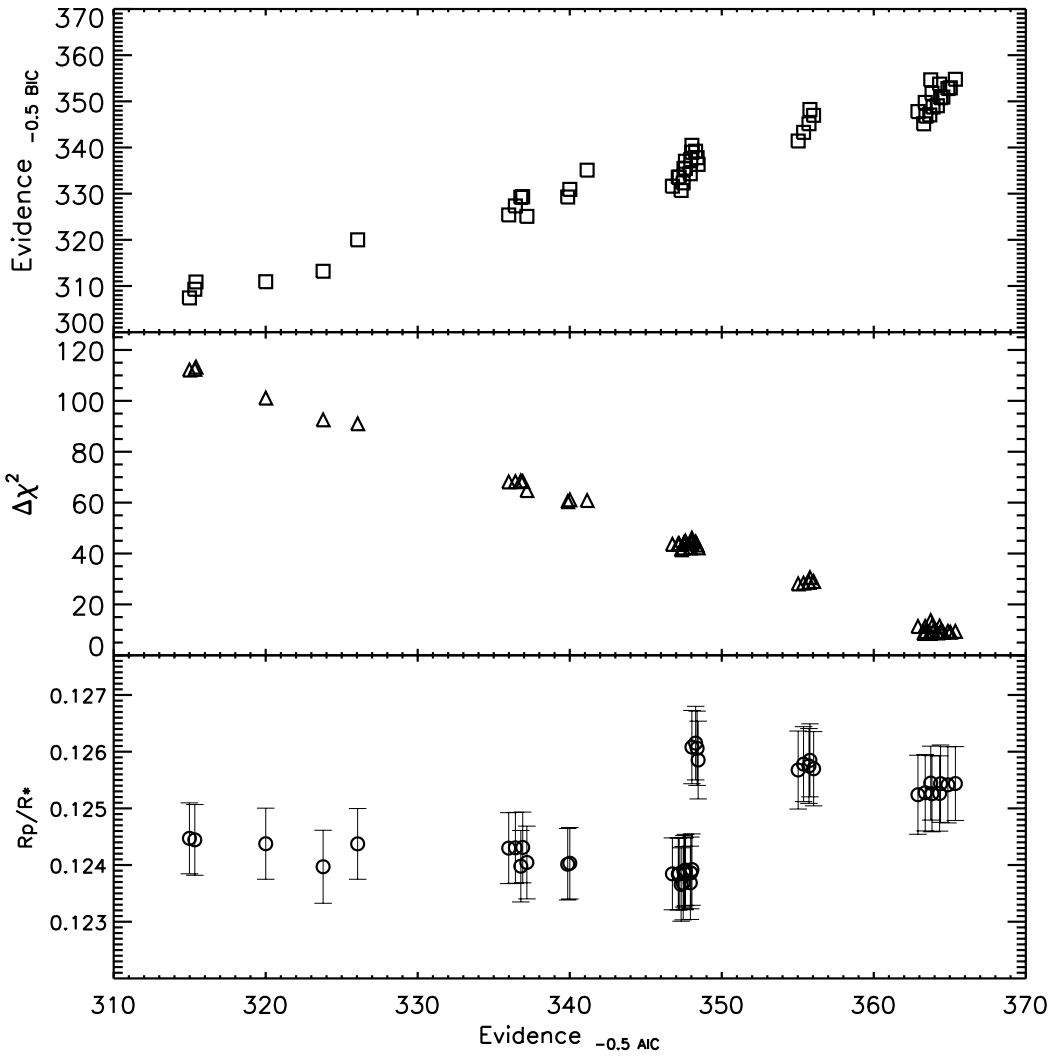

Figure 2.6.2: The evidence based on the AIC plotted against the evidence based on the BIC (top-squares), the χ^2 (middle-triangles), the R_p/R_* (bottom-circles). The best-fitting model is that with the highest AIC evidence parameter, which corresponds to minimising the χ^2.

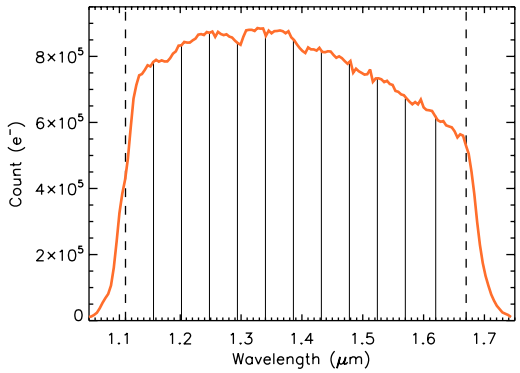

Figure 2.7.1: Stellar spectrum of WASP-31 extracted from HST WFC3 spatial scan exposure divided into wavelength bins of 10 pixels across the spectrum.

used for correction to within 1. We discuss the implications of this for each of our datasets in § 3.2. In Fig. 2.6.2 we demonstrate the statistical correlation between different factors used to select models, comparing the evidence based on the AIC approximation to that of the evidence based on the BIC approximation, and to the $\Delta\chi^2$. We additionally show the difference in the measured R_p/R_* computed for each model relative to the weight applied to that fit, again demonstrating the importance of using the correct systematic model when correcting transit data.

2.7 Spectroscopic lightcurves

We compute the spectroscopic lightcurves by binning the extracted spectra into a number of different wavelength channels (see Fig. 2.7.1). For our spectroscopic lightcurve fits we adopt the marginalised centre of transit time from our white lightcurve as a fixed parameter, and use the marginalised white lightcurve R_p/R_* as a starting parameter for each spectroscopic bin.

Each spectroscopic lightcurve is calculated by summing up the flux of each exposure spectra across the wavelength range of each bin. These spectroscopic lightcurves will likely be subject to the same systematics as observed in the white lightcurve, which shows the sum of the systematics across all wavelength bands. However, the spectroscopic lightcurves may also be affected by wavelength dependent systematics which would not be accounted for. Here we outline the method used to analyse the spectroscopic lightcurves given the white lightcurve calculations, and discuss the results for each dataset in § 3.2.

2.7.1 Sigma clipping

Prior to running spectroscopic analysis on each wavelength bin we perform a sigma clipping routine to remove any wavelength dependent outliers in the data. This process is performed using the best-fitting white lightcurve systematic model applied to each wavelength channel. From this we calculate the spectroscopic lightcurve residuals, where the transit model is removed from the data. We then remove any exposures where the normalised flux value is greater than 4σ from the standard deviation of the residual flux.

Using this we are able to remove additional effects from bad and/or hot pixels that have been missed in the prior reduction. We do not expect a significant number of spectroscopic lightcurves where a large number of exposures are removed from the analysis. This analysis will not affect the evidence, and therefore the R_p/R_* determined for each spectroscopic bin, as the weighting calculated for each bin will be computed for the same number of data points. The number of exposures in each individual wavelength bin has no effect in the subsequent bins as systematic evidence is not passed between wavelength bins.

2.7.2 Common mode removal

It is expected that a number of the systematics observed in the white lightcurves are common-mode, meaning that they are not dependent on the wavelength of the spectral bin but affect each of the columns on the detector equally for each of the individual exposures. To remove these common-mode systematics in each of the wavelength channels we use the raw white lightcurve residuals, where the white lightcurve has been fit with a model that only allows the radius ratio, centre of transit time, and baseline flux to vary.

This common mode removal method has been applied to spectroscopic lightcurve analysis by a large number of groups (e.g. Deming et al. 2013; Wakeford et al. 2013; Line et al. 2013; Kreidberg et al. 2014b). However, using this method alone assumes that the visit long linear trend, the ramp timescale, and the orbit long linear trends are independent of wavelength. We find that this is not completely the case for a number of our datasets and therefore employ an additional decorrelation with our best fit systematic model determined by our white lightcurve.

2.7.3 Systematic model

By using the best-fitting systematic model from the white lightcurve we assume that the same combination of systematics is affecting our spectroscopic lightcurves, and that while the degree to which each is contributing to the data in each wavelength dependent channel may vary, the overall model remains the same. To determine whether this assumption is valid we conduct tests on each of our transit datasets, performing the marginalisation technique for each spectroscopic lightcurve. We then compare the marginalised transmission spectrum to that computed using just the best fit white lightcurve systematic model. We discuss the results of a number of test cases in § 3.3 in the following chapter.

2.8 Application of method

In the following chapter we apply the methods outlined above to five different hot Jupiter transit observations from HST WFC3 G141 slitless spectroscopic grism. We also outline and discuss a series of tests that have been applied to the datasets to examine the robust nature of observed transmission spectral features.

If nothing else works, then a total pig-headed unwillingness to look facts in the face will see us through.

GENERAL MELCHETT
Blackadder Goes Forth

3

WFC3 hot Jupiter comparison study

Sections of this chapter have been previously published by MNRAS as part of publications containing analysis of HST Large Programme GO 12473, P.I. Sing WFC3 G141 IR observations Wakeford et al. (2013), and Sing et al. (2015).

In this chapter we present the transmission spectrum of five hot Jupiter exoplanets observed using WFC3 IR G141 spectroscopic grism. For this study we adopted a standard reduction pipeline following the steps outlined in Chapter 2, with the individual observations and results described in § 3.1 and § 3.2. Each of these exoplanet transmission spectra has been previously analysed and published: HAT-P-1b (Wakeford et al. 2013), WASP-31b (Sing et al. 2015), XO-1b (Deming et al. 2013), HD 209458b (Deming et al. 2013), and WASP-17b (Mandell et al. 2013). Across these five exoplanet transmission spectra there are a variety of measured features over the expected H_2O absorption bands, from full amplitude features extending several scale heights in the atmosphere, to muted and absent features. The study here is intended as the most uniform analysis and comparison to date, such that differences between spectra can be more easily tied to the planets themselves and differences from a different reduction techniques can be minimised. In § 3.3 we use HAT-P-1 and WASP-17 as a test example for different analysis methods, including the use of a reference star

Table 3.1.1: Table of the observation parameters for the five planetary transits measured with WFC3.

	HAT-P-1	WASP-31	XO-1	HD 209458	WASP-17
GO Program	12473	12473	12181	12181	12181
Date	2012–07–05	2012–05–13	2011–09–30	2012–09–25	2011–07–08
Mode	Scan	Scan	Scan	Scan	Stare
NSAMP	4	8	9	5	16
Subarray size	512	256	128	256	512
Exposure Time (s)	46.695	134.35	50.382	22.317	12.795
No. Exposures	111	74	128	125	131
Scan Rate (pix/s)	1.07	0.15	0.43	7.43	-

as a differential source and divide-oot as a systematic removal technique. We then compare the features observed in each planetary transmission spectrum and interpret the results given the best-fitting atmospheric models in § 3.4.

3.1 Observations

Our observations span two HST large programs and two observation modes, acquired between 2011–2012 over 25 HST orbits. Table 3.1.1 outlines the observational parameters for each of the exoplanet hot Jupiters studied here: HAT-P-1b, WASP-31b, XO-1b, HD 209458b, and WASP-17b.

We use the "*ima*" outputs from WFC3's *Calwf3* pipeline. For each exposure, *Calwf3* conducts the following processes: bad pixel flagging, reference pixel subtraction, zero-read subtraction, dark current subtraction, non-linearity correction, flat-field correction, and gain and photometric calibration. The resultant images are in units of electrons per second.

Following the spectral extraction method outlined in § 2.3 we determine the best-fitting aperture for each of the datasets. As the NSAMP varies across each of the datasets we do not follow the method used by Swain et al. (2013) and Deming et al. (2013) to produce differential spectra in an effort to keep the analysis as consistent as possible without introducing additional uncertainty to the results.

3.1.1 Wavelength shifts

The spectra are then wavelength calibrated and cross-correlated to determine the shift in the wavelength direction from exposure to exposure. Figure 3.1.1 shows the trends in wavelength across all exposures for each of the lightcurves analysed in this chapter. It can clearly be seen that this shift in wavelength on the detector is not consistent

from observation to observation. HD 209458 shows near pixel scale changes across the course of an observation period, while WASP-31 and XO-1 show variation ∼100 times smaller.

To determine the impact of the physical shift on the detector on the lightcurve, we compare the wavelength shift to the raw flux residuals computed from the white lightcurve, and calculate the correlation coefficient for each dataset as measured by the linear Pearson correlation coefficient. Figure 3.1.2 shows that there is no generic correlation between the shift in wavelength on the detector and the systematics observed in the white lightcurve for almost all datasets considered. These figures highlight the need to investigate the correlation between wavelength shift on the detector and the systematics present in the white lightcurve, as the effect could be significant in order to detrend the data. The strong correlation measured for HD 209458, which was also noted by Deming et al. (2013), suggests that wavelength dependent systematics dominate the raw data in these observations, which we discuss later in § 3.2.4.

Deming et al. (2013) also noted evidence of undersampling of the grism resolution by the pixel grid changing gradually and smoothly as a function of wavelength shift. To determine if our extracted spectra also contained similar undersampling, we compared a number of the spectral lines from the start and end of the observations (separated by over 3 hours) at a number of positions along the scanned spectra. Unlike the results found by Deming et al. (2013) we see no flattening of the strong Paschen-beta stellar line at 1.28 µm due to an undersampling effect. To help reduce the effects of any unidentified undersampling, we binned our spectra to the resolution limit of the detector (∼2 pixels), effectively smoothing out any undersampling inherent in our data.

3.2 Analysis and results

For each of the spectroscopic transit observations we compute the white lightcurve and transmission spectrum from 1.1–1.7 µm. Here we present the results from each of the hot Jupiter exoplanet transit lightcurves separately discussing the specifics of each dataset and analysis.

For each of our five exoplanetary transit datasets we extract each exposure spectrum with our custom *IDL* routine *spextract*, which optimises the aperture over which the target spectrum is exposed on each image. We then compute the white lightcurve

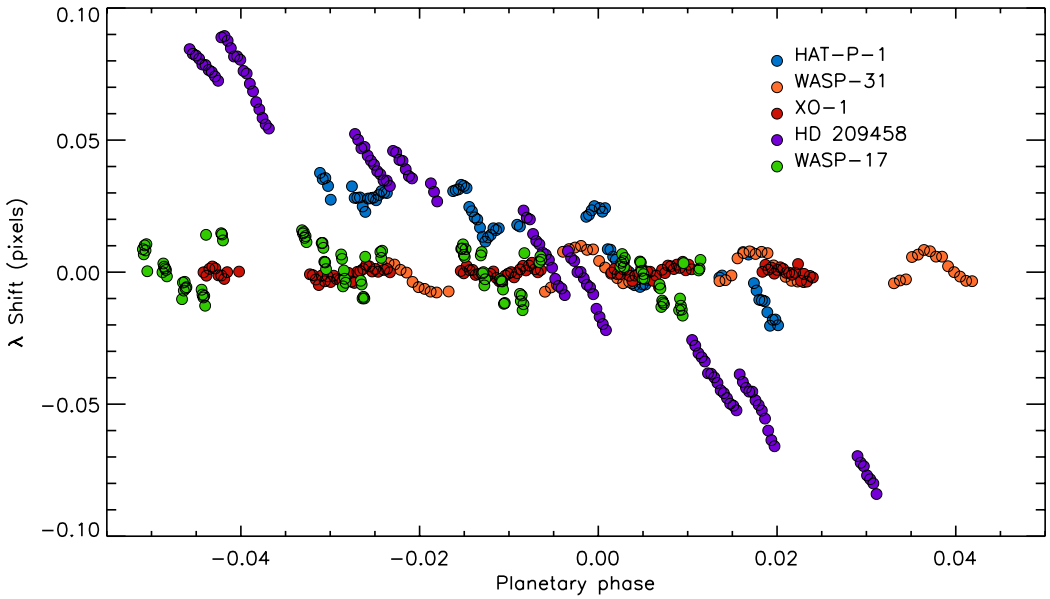

Figure 3.1.1: The observed spectral shift on the detector in the wavelength direction over the course of each planetary transit timeseries. Each planet dataset is plotted in terms of their individual observed planetary phase, where the λ shift in pixels is calculated by cross-correlating the extracted spectra.

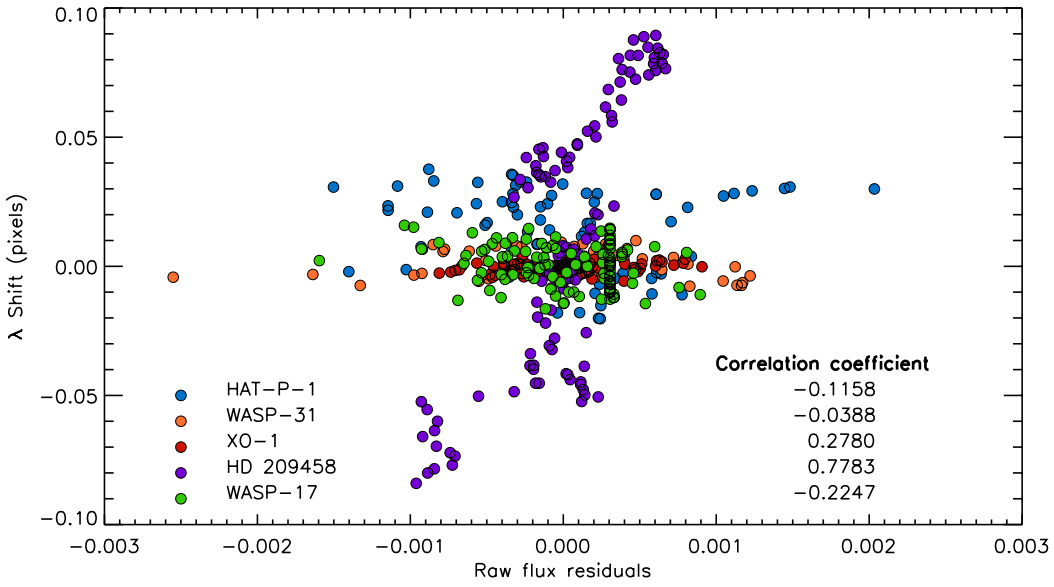

Figure 3.1.2: Trends in wavelength shift in correlation to the observed flux, where the transit is removed. The correlation coefficients show that while the shift in wavelength on the detector may be correlated, in some cases it is not the sole cause of the visit long trends seen in the lightcurves. In the case of WASP-17 we perform the divide-oot routine on the white lightcurve before obtaining the raw residuals (see § 3.2.5).

Table 3.2.1: Table of the planetary system parameters used in the analysis of the five hot Jupiters studied in this chapter. We also list the white light limb-darkening coefficients for each star and the derived R_p/R_* from the individual white lightcurves analyses.

Parameters	HAT-P-1[1]	WASP-31[2]	XO-1[3]	HD 209458[3]	WASP-17[4]
Rp (R_J)	1.319	1.55	1.209	1.38	1.932
Mp (M_J)	0.525	0.48	0.942	0.714	0.477
T_{eff} (K)	1322	1570	1210	1459	1755
Period (days)	4.46529976	3.405886001	3.94163	3.52474859	3.7354833692
Epoch (MJD)	56114.34028	56060.69042	55834.3419	56195.7595	55750.2973239
inclination (°)	85.634	84.670	88.92	86.59	86.917160
a/R*	9.91	8.19	11.24	8.859	7.03
T* (K)	5980	6250	5750	6117	6550
$[Fe/H]*$	0.130	-0.2	0.02	-0.02	-0.25
White Light Parameters					
c1	0.58115522	0.49271309	0.57505270	0.55407671	0.46913939
c2	0.08416305	0.32553801	0.07068500	0.15318674	0.38874433
c3	-0.1886652	-0.5299505	-0.1131334	-0.2741835	-0.6396845
c4	0.05957531	0.21191308	0.01649965	0.09583456	0.26591443
Rp/R*	0.11852±0.00073	0.12540±0.00067	0.13215±0.00040	0.12065±0.00031	0.12319±0.00122

[1]Wakeford et al. (2013), [2]Sing et al. (2015), [3]Deming et al. (2013), [4]Mandell et al. (2013)

by summing the flux over all exposed wavelengths to determine the general system parameters and nature of systematics impacting the spectra. The systematics for each transit dataset are determined using a grid of 52 systematic models using a combination of systematics in the parametrised model and the two different exponential models, which is outlined in § 2.6. We then perform a marginalisation on the computed planet-to-star radius ratio, and centre of transit time, and determine the best-fitting systematic model with the maximum weight from the white lightcurve.

We then compute the spectroscopic transmission spectrum by binning up each exposure spectrum into a number of wavelength bins (4, 7, and 10 pixels wide). We perform sigma clipping on each of the datasets using the best-fitting white lightcurve systematic model, as outlined in § 2.7.1, to remove wavelength dependent outliers that deviate from the residual scatter by greater than 4σ. For each spectroscopic lightcurve we divide through by the raw white lightcurve residuals to remove any common-mode trends in the data spanning all wavelength regimes. We then apply the best-fitting systematic model determined from the white lightcurve weighting to remove any further wavelength dependent systematics in each spectroscopic bin. The measured transmission spectrum are then fit with a suite of theoretical atmospheric transmission spectra from a grid of models formulated by Fortney et al. (2010) to constrain the atmospheric parameters and determine the significance of any observed absorption features.

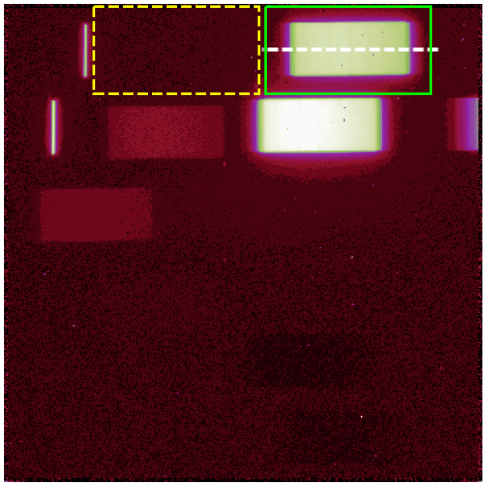

Figure 3.2.1: Single *ima* output exposure image of HAT-P-1's spectrum outlined in green. We highlight the centering profile trace as a white dashed line and outline the region used for background calibration in yellow. Each HAT-P-1 WFC3 subarray exposure also contains the zeroth order spectrum to the left of the background subtraction region, and the spectral trace from HAT-P-1's companion star below the target spectrum.

3.2.1 HAT-P-1b

HAT-P-1b is a low-density hot Jupiter orbiting a single member of a visual stellar binary (Bakos et al. 2007). HAT-P-1b orbits its host star with a period of 4.5 days at a distance of 0.055 AU. It has a radius similar to that of HD 209458b with a somewhat lower mean density and a mass of 0.54 M_J. Spitzer IRAC secondary eclipse measurements show that the atmosphere is best fit with a modest temperature inversion with a maximum dayside temperature of 1550 K, assuming zero albedo, a uniform temperature over the dayside hemisphere, and no transport to the nightside (Todorov et al. 2010). Ks-band secondary-eclipse observations have also been conducted by the GROUnd-based Secondary Eclipse (GROUSE) project with an estimated brightness temperature of 2136±150 K for an eclipse depth of 0.109±0.025%, although there are still visible systematics that remain in the fitted data (de Mooij et al. 2011).

Here we analyse a single transit of HAT-P-1b, which was observed with HST WFC3 on July 5th 2012, in forward spatial scan mode using the G141 spectroscopic grism as part of a large HST programme (HST GO 12473, P.I. Sing). Forward spatial scans were conducted at a rate of ∼1.07 pixels per second, with a final spatial scan covering ∼50 pixels in the cross-dispersion direction on the detector. We trimmed a 180×100 box around each spectral image and extracted the spectra with an aperture of ±25 pixels around the computed centring profile, which was found to be consistent across the spectrum with an error of 0.01 pixels. Background subtraction was applied using a clean region of the untrimmed image to the left of the spectral dispersion, as the regions above and below the spectra cannot be accessed due to the positioning on

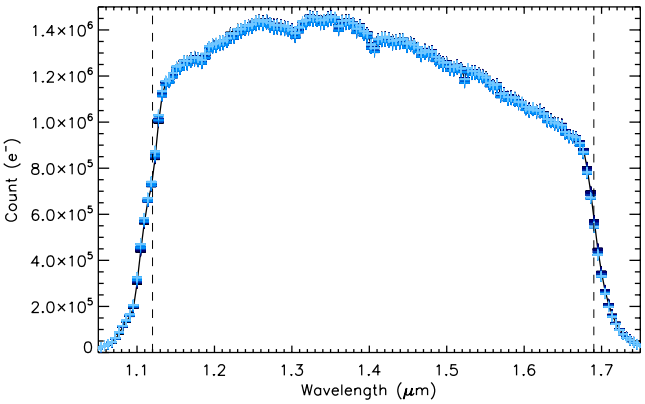

Figure 3.2.2: All exposed spectra of HAT-P-1 cross-correlated and overplotted on a scale of wavelength vs. count.

the subarray and the presence of the companion spectra (see Fig. 3.2.1). An average background count of $\sim$45 $e^{-}s^{-1}$ was found for each exposure with a maximum count rate of 25,000. Additional details of the observation can be found in Table 3.1.1.

The wavelength solution was calculated using an F139M filter image taken prior to the transit observation, giving a spectral range from 1.07–1.74 µm. Figure 3.2.2 shows all 111 spectral exposures over-plotted displaying the count rate per second for each pixel column, with the vertical lines indicating the restricted wavelength range used to compute the transmission spectrum. This excludes the strongly sloped edges of the grism response which produce unreliable radius ratio measurements.

White lightcurve

Before computing the white lightcurve, and subsequent transmission spectrum, we remove the first orbit and an additional nine exposures, which are found to have a total count greater than 4σ from our standard transit model, reducing our total exposure count to 77 exposures across four HST orbits. The raw white lightcurve is computed by summing the counts for each exposure across the entire wavelength range and computing the planetary phase from the time stamp of each exposure header and the planetary orbital period from Nikolov et al. (2014).

Figure 3.2.3 shows the normalised raw white lightcurve and the raw residuals computed fitting a standard Mandel & Agol (2002) transit model to the timeseries (black). We then fit the white lightcurve with a grid of parametrised systematic models, including two exponential models (with and without planetary phase squared), to the dataset and compute the evidence and weighting values following steps outlined in § 2.6.1.

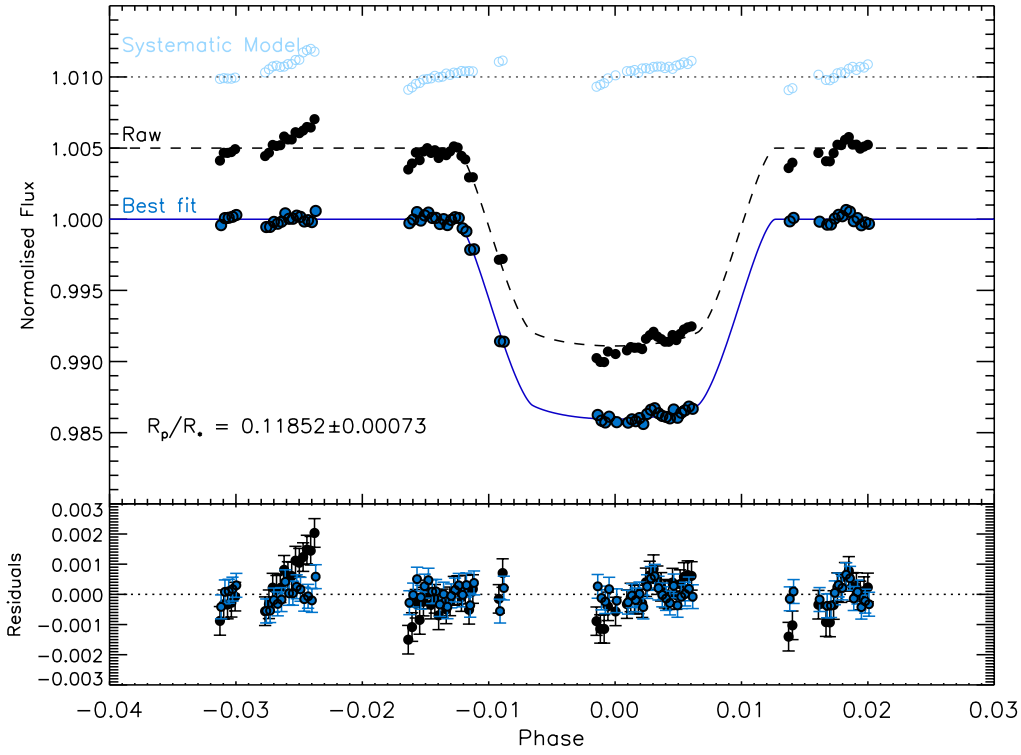

Figure 3.2.3: HAT-P-1 raw white lightcurve (black-middle) and corrected lightcurve (blue-bottom), corrected by dividing through with the best-fitting systematic model fit to our data (light blue-top). Each lightcurve is offset in flux for clarity. The bottom figure shows the residuals from each lightcurve overplotted to compare the systematics and uncertainties.

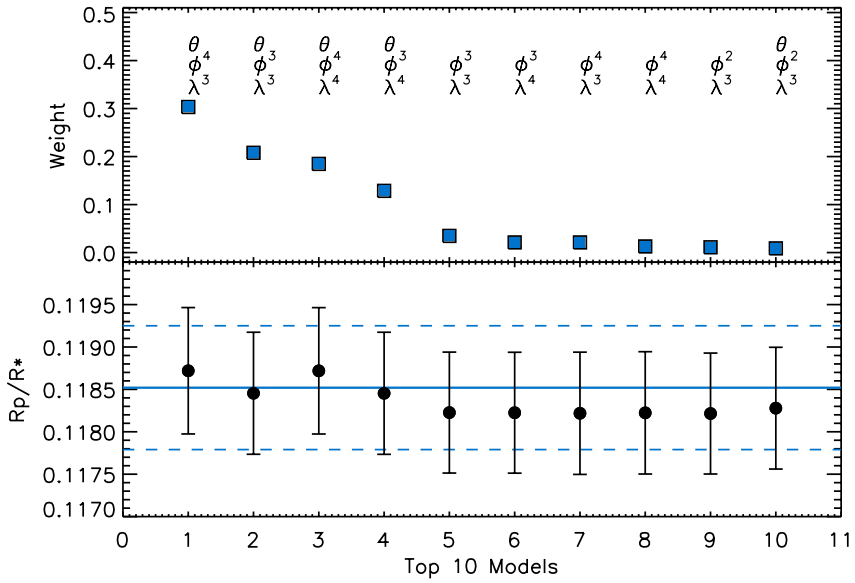

Figure 3.2.4: Top: Weighting for the top 10 models fit to the white lightcurve based on the AIC approximation. The model parameters are outlined below each model with best to worst from left to right. θ corrects a visit-long slope, ϕ^N the HST orbital phase, where N is the order of the polynomial used, and λ^N is the wavelength shift polynomial correction applied. Bottom: The computed R_p/R_* and uncertainty for each of the models as in the top plot. The solid horizontal line represents the final marginalised radius ratio with the dashed lines marking the uncertainty range.

We use the AIC approximation, which tends to favour more complex models, and find the most favoured systematic model fit to the white light data to be

$$systematics = T_1\theta + \sum_{i=1}^{4} p_i\phi^i + \sum_{j=1}^{3} l_j\lambda^j, \tag{3.1}$$

with "HST breathing" effects dominating the white lightcurve systematics and additional trends in wavelength that are fit with a third order polynomial, and planetary phase contributing to the observed systematics. The weighting of the top ten systematic models favoured by the fitting are shown in Fig. 3.2.4 with the corresponding R_p/R_* values and uncertainties determined from the white lightcurve. This shows more clearly the impact the different systematic models have on the resultant measurements of the desired transit parameters. When the weighting assigned to the systematic model used to reduce the data becomes negligible, the impact on the final values also reduces, meaning only the best models are relevant in any fit. In the case of this HAT-P-1 dataset there is a clear change in the goodness of fit between systematic models with and without a linear correction in planetary phase between

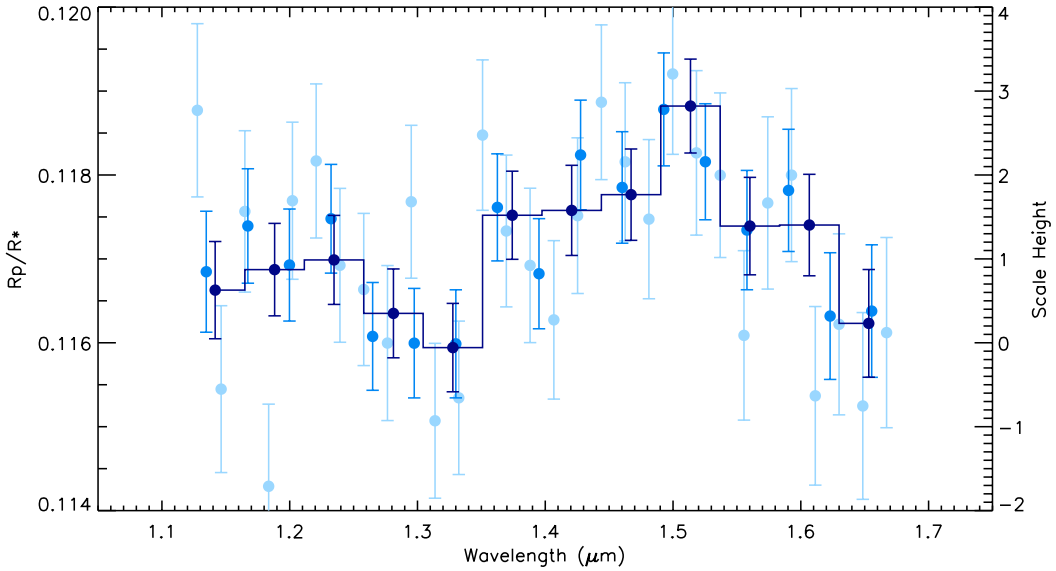

Figure 3.2.5: HAT-P-1b transmission spectrum measured at three different resolutions, where the flux is summed over 4 (light blue), 7 (blue), and 10 pixels (dark blue). The transmission spectrum measured for a bandwidth of ∼463 Å (10 pixels) is picked out with the dark blue histogram and used for further analysis.

the 4th and 5th best model, which is also evident in the corresponding R_p/R_* values.

It can be seen in Fig. 3.2.3 that the favoured systematic model is able to remove the systematic slope observed over each orbit, in combination with a general slope across the whole visit, while reducing the uncertainties on each exposure (blue points). Our final planet-to-star radius ratio is computed to be 0.11852±0.00073 when the result from all 52 models are taken into account and marginalised over, including the fit to the raw white lightcurve. A majority of the systematic models will contribute negligibly to the final R_p/R_* value, but by marginalising the uncertainties we can produce much more realistic errorbars for the desired parameters.

This newly computed white lightcurve depth is significantly different ($\sim 2\sigma$) from the previously published R_p/R_* value of 0.11709±0.00036. This is likely due to the use of single target photometry, whereas Wakeford et al. (2013) made use of HAT-P-1's companion star, which can also be extracted from the original spectroscopic images and used as a differential source. In § 3.3 we discuss the use of differential spectrophotometry on WFC3 data, and show the result of different analysis methods on the resultant transmission spectrum.

Table 3.2.2: Table of transmission spectral properties of HAT-P-1b with a bin width of $\Delta\lambda = 463$ Åisting the central wavelength, planet-to-star radius ratio, and uncertainty on the radius ratio, σ. Also listed are the four parameter non-linear limb-darkening law coefficients for each spectral bin.

Wavelength	Rp/R*	σ	c1	c2	c3	c4
1.1416	0.11662	0.00057	0.58691	-0.13716	0.24816	-0.14732
1.1881	0.11687	0.00055	0.57084	-0.06694	0.15524	-0.10808
1.2346	0.11698	0.00053	0.53952	-0.02055	0.12136	-0.09935
1.2811	0.11635	0.00052	0.48595	0.35512	-0.45193	0.15276
1.3276	0.11594	0.00052	0.52254	0.20072	-0.25522	0.06995
1.3741	0.11751	0.00052	0.52766	0.17533	-0.23096	0.06417
1.4206	0.11757	0.00053	0.45184	0.79842	-1.16000	0.47044
1.4671	0.11776	0.00054	0.56762	0.23555	-0.46342	0.18583
1.5136	0.11882	0.00055	0.60325	0.02323	-0.19071	0.07294
1.5601	0.11739	0.00058	0.68342	0.06590	-0.44529	0.21673
1.6066	0.11740	0.00060	0.68331	0.05243	-0.42363	0.20722
1.6531	0.11623	0.00064	0.72260	-0.01454	-0.44492	0.23470

Transmission spectrum

The transmission spectrum of HAT-P-1b is computed over a restricted wavelength range from 1.12 to 1.69 µm using the best-fitting systematic model determined from the white lightcurve analysis. Here we compute the transmission spectrum for a range of bins from 4 pixels, ∼185 Å, to 7 pixels, ∼324 Å, and 10 pixels, ∼463 Å. Figure 3.2.5 shows the transmission spectrum for HAT-P-1b over this range of binsizes, where the values of the planet-to-star radius ratio and limb-darkening parameters for a binsize of 0.463 µm (10 pixels) are picked out with the dark blue histogram and listed in Table 3.2.2. We use the $\Delta\lambda = 463$ Å transmission spectrum for further analysis to compare to the other four exoplanet transmission spectra calculated and discussed in this chapter. Figure 3.2.6 shows each of the individual spectroscopic lightcurves with a wavelength bandwidth of 463 Å, which is equivalent to ∼5 resolution elements on the detector.

Figure 3.2.7 shows the transmission spectrum at a bandwidth of 463 Å from our single target marginalisation analysis compared to the published transmission spectrum in Wakeford et al. (2013), which was computed using differential spectrophotometry using the companion spectrum, and a parametrised systematic model with a 7th order HST phase term. In addition, the previously published transmission spectrum

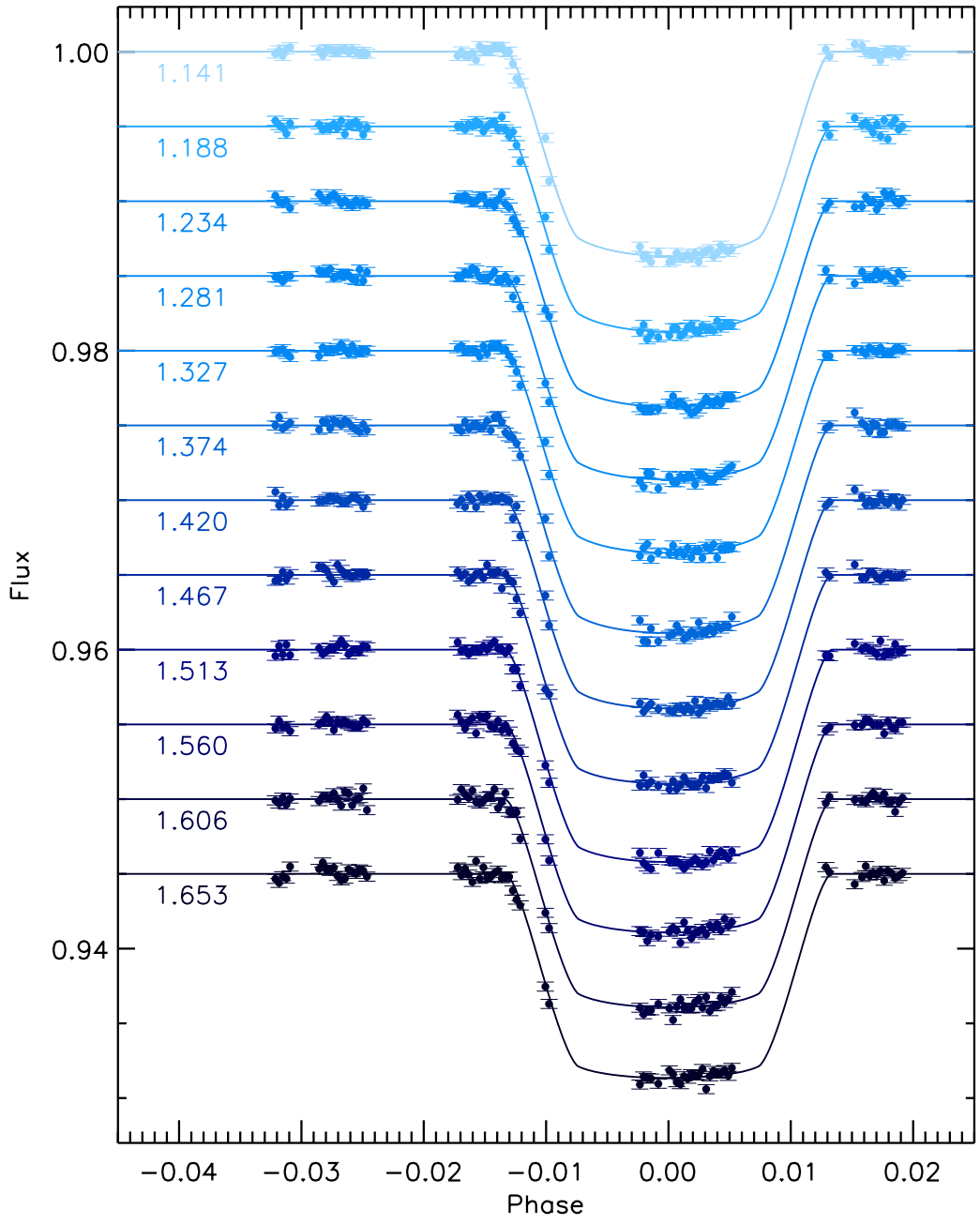

Figure 3.2.6: Spectroscopic lightcurves of HAT-P-1 for bins of 10 pixels (463 Å) from 1.12–1.69 µm. The lightcurves are offset in flux for clarity.

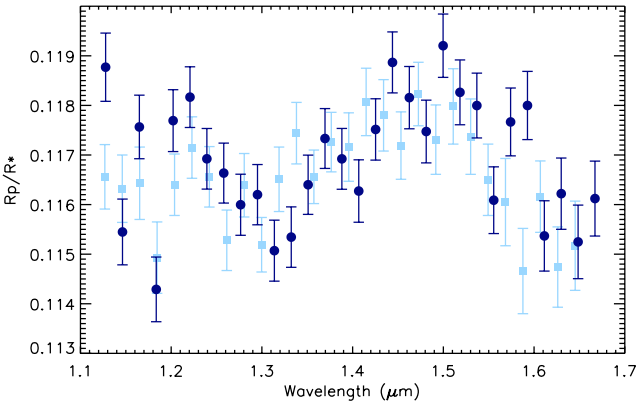

Figure 3.2.7: HAT-P-1b transmission spectrum with a bin width of 185 Å (dark circles) compared the previously published transmission spectrum of Wakeford et al. (2013) (light squares).

is computed using 3D limb-darkening tables from Hayek et al. (2012), compared to the non-linear limb-darkening law using the 1D ATLAS models followed in this analysis. Both methods reveal a clear water feature at 1.4 µm (see Fig. 1.3.4 and §1.6), with only small deviations in amplitude (see § 3.3).

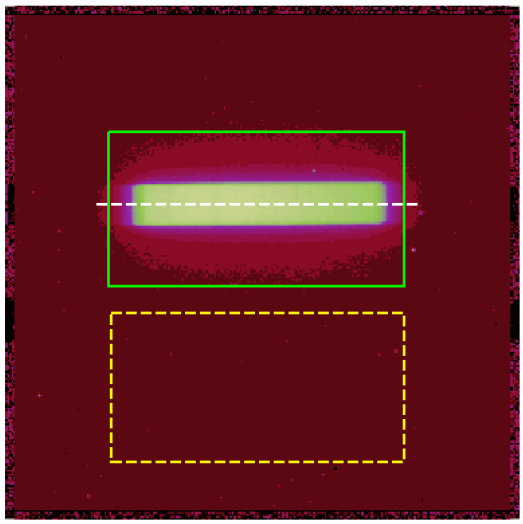

Figure 3.2.8: Single *ima* frame of a WASP-31 spectral exposure image. The green box outlines the extraction window cut out of the subarray, with the centering profile used for the aperture spectral extraction. The yellow dashed line encloses the region used for background subtraction.

3.2.2 WASP-31b

WASP-31b is a low mass ($0.48\,M_J$) hot Jupiter with a radius of $1.55\,R_J$ and a therefore low planetary density of $0.129\,g/cm^3$. WASP-31b orbits a low metallicity, low activity F6V star with a period of 3.405 days. A best-fit planetary equilibrium temperature of $1575\pm32\,K$ is found by Anderson et al. (2011), assuming zero albedo and efficient redistribution of heat from the planet's dayside to its nightside. The planet's high temperature, low density and correspondingly low surface gravity ($4.56\,ms^{-1}$) make it very favourable to transmission spectral studies due to an atmospheric scale height greater than 1000 km. HST STIS observations in the optical indicate Rayleigh scattering at short wavelengths and a cloud deck stretching into the near-IR (Sing et al. 2015). The observations also show the presence of a narrow potassium feature at a pressure of ∼10 mbar, though little to no sodium is detected, suggesting a sub-solar [Na/K] abundance ratio.

A single transit of WASP-31b was observed with HST WFC3 on May 13th 2012, in forward spatial scan mode using the G141 spectroscopic grism as part of a large HST programme (HST GO 12473, P.I. Sing). Forward spatial scans were conducted at a rate of ∼0.15 pixels per second, with the final spatial scan spanning ∼22 pixels. We trimmed a 152×80 box around each spectral image and extracted the spectra with an aperture of ±12 pixels around the computed centring profile, which was found to be consistent across the spectrum with an error of 0.06 pixels (see Table 3.1.1). Background subtraction was applied using a clean region of the untrimmed image directly below the target spectral trace (see Fig. 3.2.8). A maximum count rate of

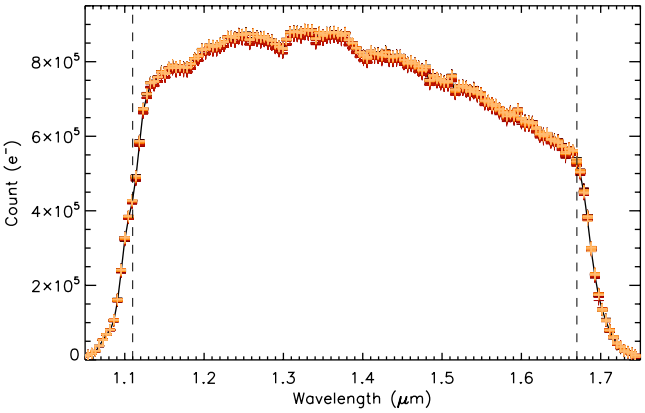

Figure 3.2.9: All spectra of WASP-31 cross-correlated and overplotted on a scale of wavelength vs. count. The vertical dashed lines represent the wavelength cut off used in the transmission spectral analysis.

$\sim$38,000 counts/pixel was obtained with an average background count of $\sim$27 $e^{-}s^{-1}$.

Figure 3.2.9 shows the spectrum of all 74 exposures after cross-correlation and wavelength calibration. The wavelength solution is calculated using a F139M filter image, giving a spectral range from 1.04–1.76 µm. This is later restricted to 1.11–1.67 µm, shown by dashed lines, when constructing the transmission spectrum from various spectroscopic bins as the strongly sloped sides of the spectrum produce unreliable results.

White lightcurve

To compute the white lightcurve we remove the first orbit of observations as the flux shows systematics that are inconsistent with the subsequent orbits. We also remove a further three exposures from the fit as they are found to be greater than 4σ from the standard deviation of the raw white light residual flux. This results in a total of 56 exposures across the remaining 4 HST orbits. The raw lightcurve is calculated by summing the spectral flux across all wavelengths from 1.05–1.76 µm. We use the system parameters from Sing et al. (2015) to compute the Mandel & Agol (2002) transit model fixing the inclination and a/R_* to the values shown in Table 3.2.1, as the phase coverage of our observations does not allow for strong constraints to be placed on the general system parameters.

Figure 3.2.10 shows the raw white lightcurve and residuals (black) and the corrected flux (orange) given the best-fitting systematic model from the grid of models

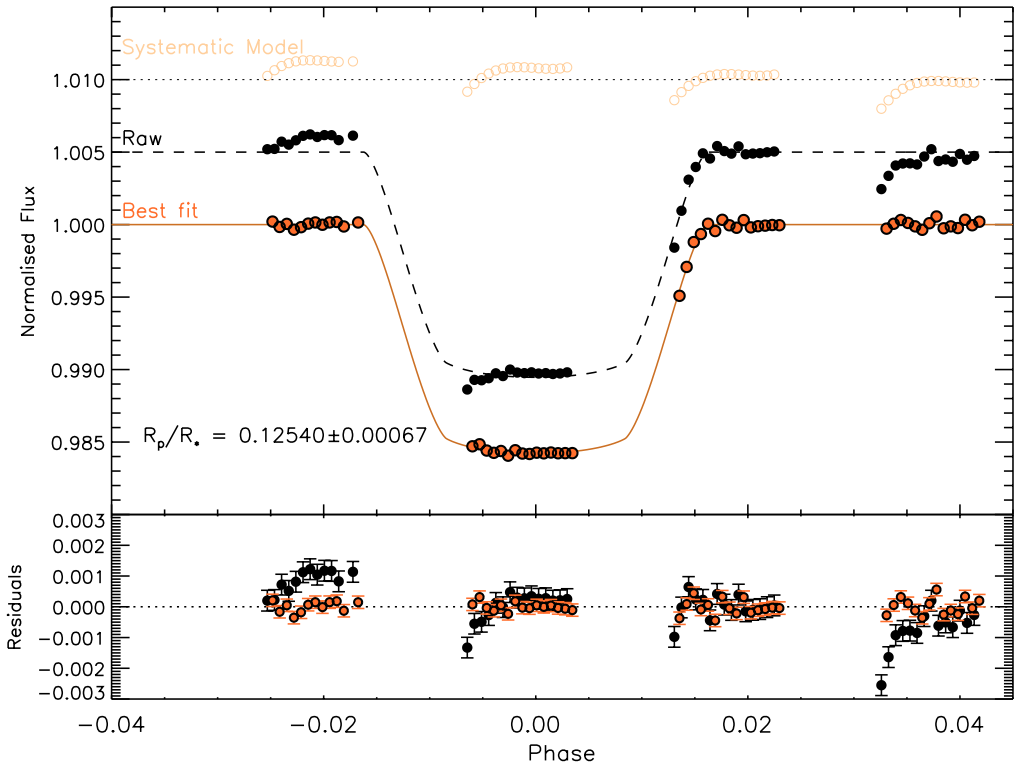

Figure 3.2.10: WASP-31 raw white lightcurve (black-middle) and corrected lightcurve (orange-bottom), corrected by dividing through with the best-fitting systematic model determined from a grid of potential models (light orange-top). The lightcurves are offset in flux for clarity. The bottom plot shows the residuals from each lightcurve with the associated uncertainties.

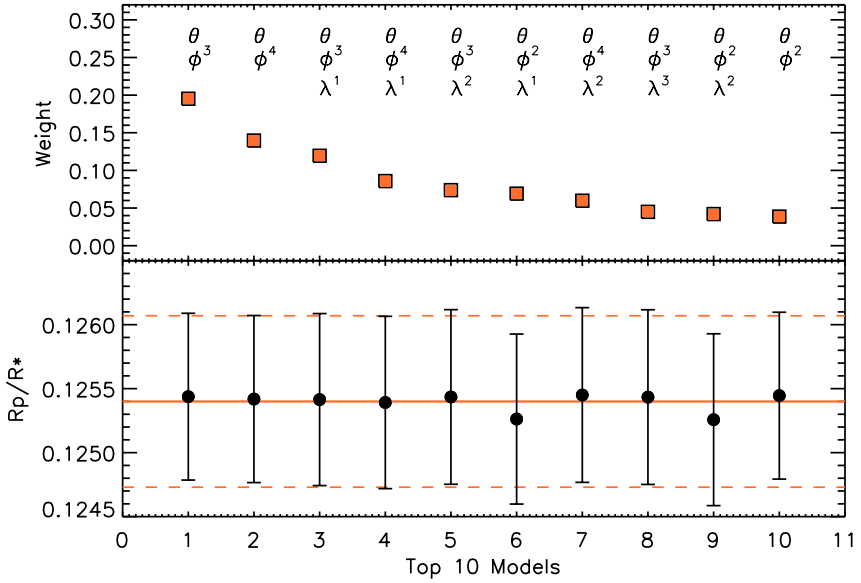

Figure 3.2.11: Top: Weighting for the top 10 models fit to the white lightcurve based on the AIC approximation. The model parameters are outlined below each model with best to worst from left to right. (symbols same as Fig. 3.2.4) Bottom: The computed R_p/R_* and uncertainty for each of the models as in the top plot. The solid horizontal line represents the final marginalised radius ratio with the dashed lines marking the uncertainty range.

shown in Table 2.6.1. The best-fitting model is found to be,

$$systematics = T_1\theta + \sum_{i=1}^{3} p_i\phi^i. \tag{3.2}$$

This shows that the white lightcurve is dominated by "HST breathing" effects, with a linear trend across the entire visit. Marginalising over a grid of systematic models we compute an $R_p/R_* = 0.12540 \pm 0.00067$. We find a similar fit using both the AIC approximation, as above, and the BIC approximation, which favoured the same systematic model and a marginalised R_p/R_*=0.12541 ± 0.00066. We show the top ten model weights and R_p/R_* in Fig. 3.2.11 for the white lightcurve systematic models, which clearly shows the dominant systematics impacting the exposure images. This also shows that the computed radius ratio is robust across a range of systematic models, even as the weighting becomes negligible.

The previously published white lightcurve depth for the atmosphere of WASP-31b using this WFC3 dataset lies well within the uncertainty of our marginalised value, $R_p/R_* = 0.12536 \pm 0.00050$ (Sing et al. 2015). The analysis used in Sing et al. (2015) applies the same systematic model and a non-linear limb-darkening law. The slight

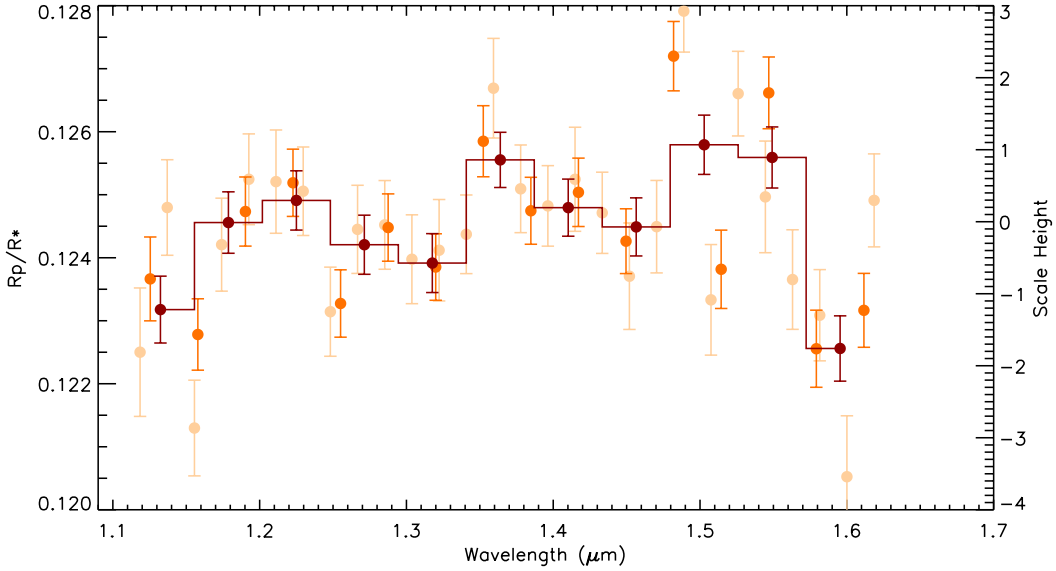

Figure 3.2.12: WASP-31b transmission spectrum measured at 4 (light orange), 7 (orange), and 10 pixels (dark orange) bandwidth across the spectrum. We highlight the transmission spectrum with a bin width of 463 Å (10 pixels) as this is the transmission spectrum used for subsequent atmospheric interpretation.

differences in the computed values can be accounted for by the marginalisation. While the best-fitting systematic model is heavily favoured in this case, $W_q = 0.3$, the other systematic models in the grid additionally contribute to the final radius ratio and uncertainty.

Transmission spectrum

The transmission spectrum is computed from 1.11 to 1.67 µm with a pixel binsize of 4, 7, and 10 pixels by summing the flux in the spectrum across the equivalent wavelength bins $\Delta\lambda = 185$, 324, and 463 Å respectively. We use the best-fitting systematic model from the white lightcurve to decorrelate each of our spectroscopic lightcurves, removing any outliers that deviate greater than 4σ from the residuals in each bin, and calculate the respective R_p/R_*.

Figure 3.2.12 shows the resultant transmission spectrum at each bin, where we highlight the transmission observed at a resolution of 10 pixels. In Table 3.2.3 we list the R_p/R_* and uncertainty for each 10 pixel bin, along with the corresponding

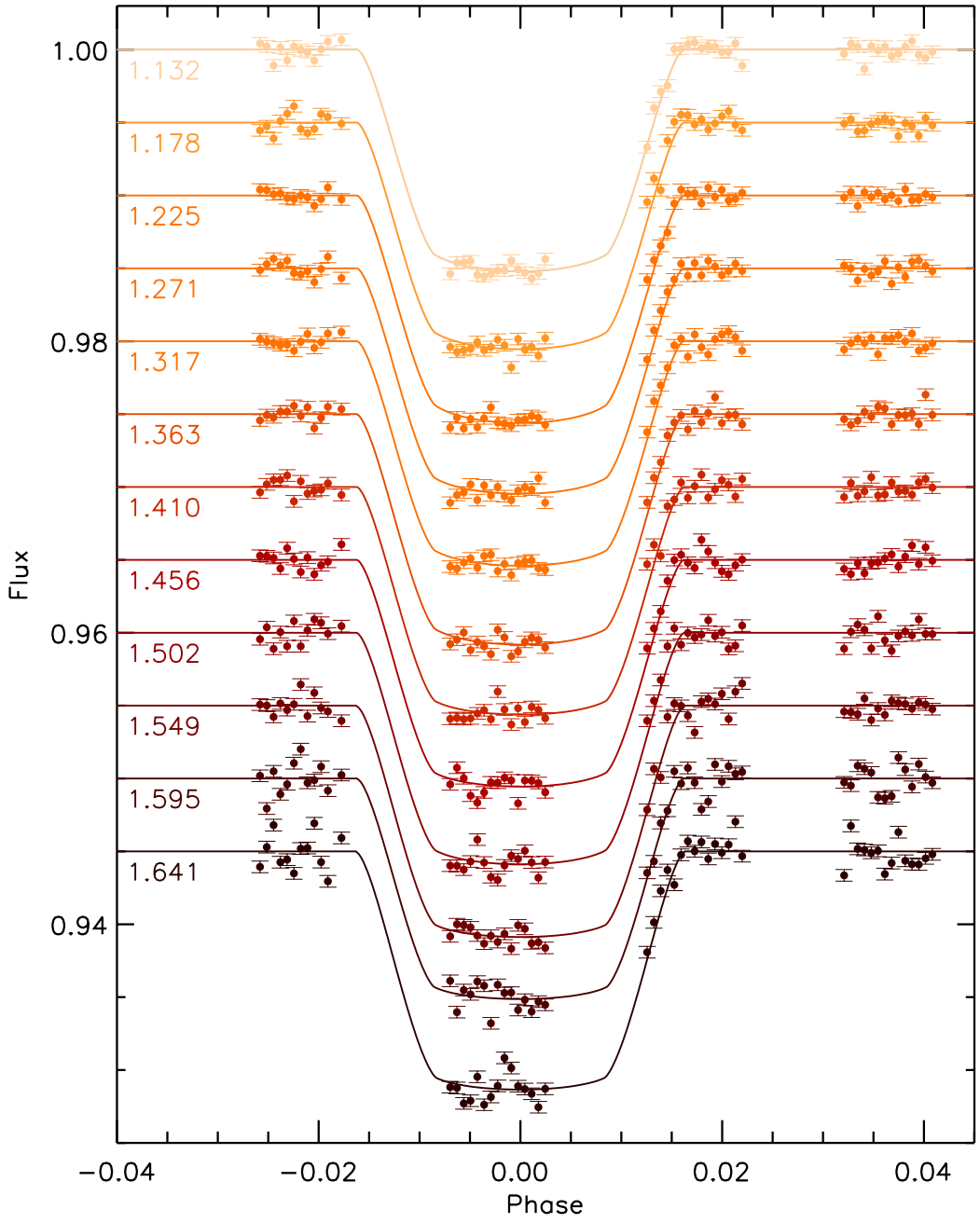

Figure 3.2.13: Spectroscopic lightcurves of WASP-31 when the spectrum is divided into 10 pixel bins between 1.11 to 1.67 µm. The lightcurves are offset in flux for clarity, making changes in the transit depth clear.

Table 3.2.3: Table of transmission spectral properties of WASP-31b, and the limb-darkening parameters for each wavelength 10 pixel bin.

Wavelength	Rp/R*	σ	c1	c2	c3	c4
1.1324	0.12317	0.00053	0.45746	0.22881	-0.20593	0.03692
1.1787	0.12455	0.00048	0.44448	0.30250	-0.33246	0.09706
1.2250	0.12490	0.00047	0.04592	1.94405	-2.52702	1.07374
1.2713	0.12420	0.00046	0.38512	0.61466	-0.80384	0.31029
1.3176	0.12391	0.00046	0.42515	0.49046	-0.67197	0.25622
1.3639	0.12555	0.00043	0.41418	0.55768	-0.77184	0.30154
1.4102	0.12479	0.00045	0.46535	0.54559	-0.94731	0.42497
1.4565	0.12448	0.00046	0.50042	0.41013	-0.73435	0.31584
1.5028	0.12579	0.00047	0.53304	0.34252	-0.66807	0.28998
1.5491	0.12559	0.00048	0.67445	0.04875	-0.50431	0.27085
1.5954	0.12255	0.00051	0.65832	0.07951	-0.50611	0.25766

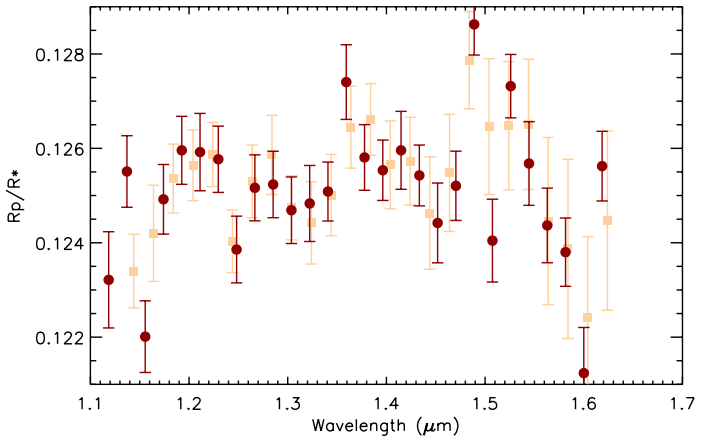

Figure 3.2.14: WASP-31b transmission spectrum with a bin width of 185 Å (dark circles) compared with the previously published transmission spectrum from Sing et al. (2015) (light squares).

limb-darkening parameters.

The spectroscopic lightcurves for each of the 12 wavelength bins summed over 10 pixels on the detector show the variation in scatter across the stellar spectrum (see Fig. 3.2.13). There are still some visible outliers in each of the individual lightcurves which are not accounted for in our sigma clipping or by the systematic model corrections. We compare this newly computed transmission spectrum with the one previously published in Sing et al. (2015), which can be seen in Fig. 3.2.14. The difference in the overall level of the transmission spectrum is likely the result in the common-mode removal, which can cause a change in the absolute level of the whole spectrum relative to the absolute depth computed from the white lightcurve.

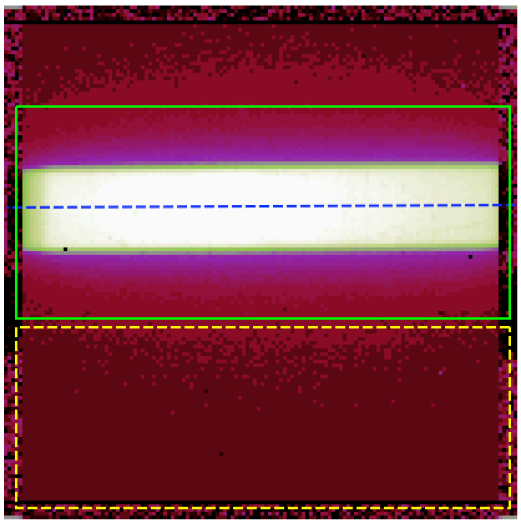

Figure 3.2.15: Single *ima* exposure frame of the spectral trace from XO-1. The green box indicates the box trimmed around the exposure with the dashed blue line representing the centring profile through the spectrum for aperture extraction. The yellow dashed line encloses the region used for background extraction.

3.2.3 XO-1b

XO-1b was the first transiting exoplanet to be discovered by the XO project in 2006 (McCullough et al. 2006). XO-1b orbits one of the most Sun-like exoplanet host stars known, with $R_* = 1.0 \pm 0.08\,R_\odot$ and $M_* = 1.0 \pm 0.03\,M_\odot$. The hot Jupiter exoplanet was confirmed using both radial velocity measurements to determine its mass ($M_p = 0.942\,M_J$) and through the planetary transit finding a $R_p = 1.209\,R_J$ and an orbital period of 3.941 days (McCullough et al. 2006; Holman et al. 2006; Cáceres et al. 2009; Burke et al. 2010; Deming et al. 2013). *Spitzer* IRAC secondary eclipse measurements at 3.6, 4.5, 5.8, and 8.0 µm suggest an atmosphere with a moderate temperature inversion and a possible stratospheric absorber (Machalek et al. 2008).

WFC3 near-IR G141 spectroscopic grism spectra were obtained for XO-1 as part of the large HST programme GO 12181 (P.I. D. Deming) on September 30, 2011 in forward spatial scan mode. The observations were conducted using WFC3's smallest sub-array field of 128×128 pixels, which can be seen to cut off the edges of the spectral trace in the exposure images (see Fig. 3.2.15) and in turn cutting off the steeply sloped sides of the grism response at ∼1.68 µm (see Fig. 3.2.16).

The XO-1 dataset is very similar to that of WASP-31, where each covers ∼20 pixels in the cross-dispersion direction, and with stars of similar brightness. To extract each of the spectra we trim a 134×62 box around the spectral trace and sum the flux across an aperture of ±12 pixels around a computed centring profile. Figure 3.2.16 shows all 127 spectra plotted with the wavelength solution determined from the position of

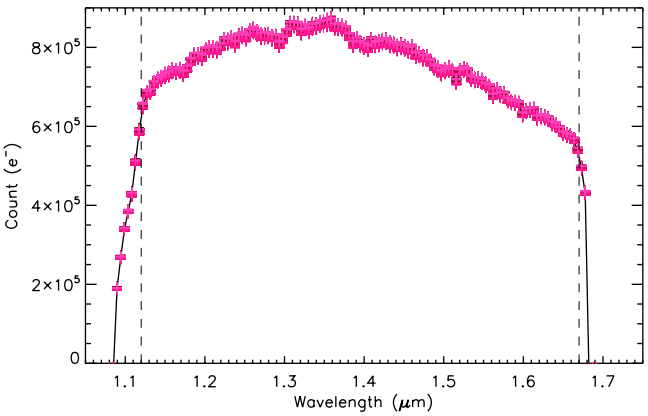

Figure 3.2.16: All spectra of XO-1 cross-correlated and overplotted on a scale of wavelength vs. count. This shows the cut-off caused by the selected subarray size on the strongly sloped sides of the stellar spectrum. The vertical dashed lines represent the wavelength cut off used in the transmission spectral analysis.

the target star on the F139M filter image obtained prior to the transit observations. We use an unexposed region of the ima exposure image to correct for the background count level, which shows a mean count of 67 e^-/s over the 22 pixel range covered by the spectral trace.

White lightcurve

We compute the white lightcurve from the 127 exposures across 5 orbits and evaluate the impact of the first orbit systematics. We find that the first orbit is only subject to extreme changes in the grism response during the first five exposures, which we remove for the following analysis. We remove a further five exposures across the visit which exhibit residual scatter greater than 4σ to that of the mean flux. The raw flux for each exposure is calculated by summing the flux across the entire spectrum from 1.08 – 1.70 µm. Figure 3.2.17 shows the raw white lightcurve (black) and the corrected lightcurve (red) using the most favoured systematic model

$$model = T_1\theta + \sum_{i=1}^{3} p_i \phi^i. \tag{3.3}$$

To calculate the transit model we fix the planetary inclination and a/R_* to previously published values (see Table 3.2.1). While the 3rd HST orbit covers the ingress of the planet, the WFC3 data does not have sufficient phase coverage to further constrain these parameters. The best-fitting systematic model favours correctional trends to remove the effects of "HST breathing" on the observations and a small linear correction over the entire visit. We marginalise over the grid of 52 systematic

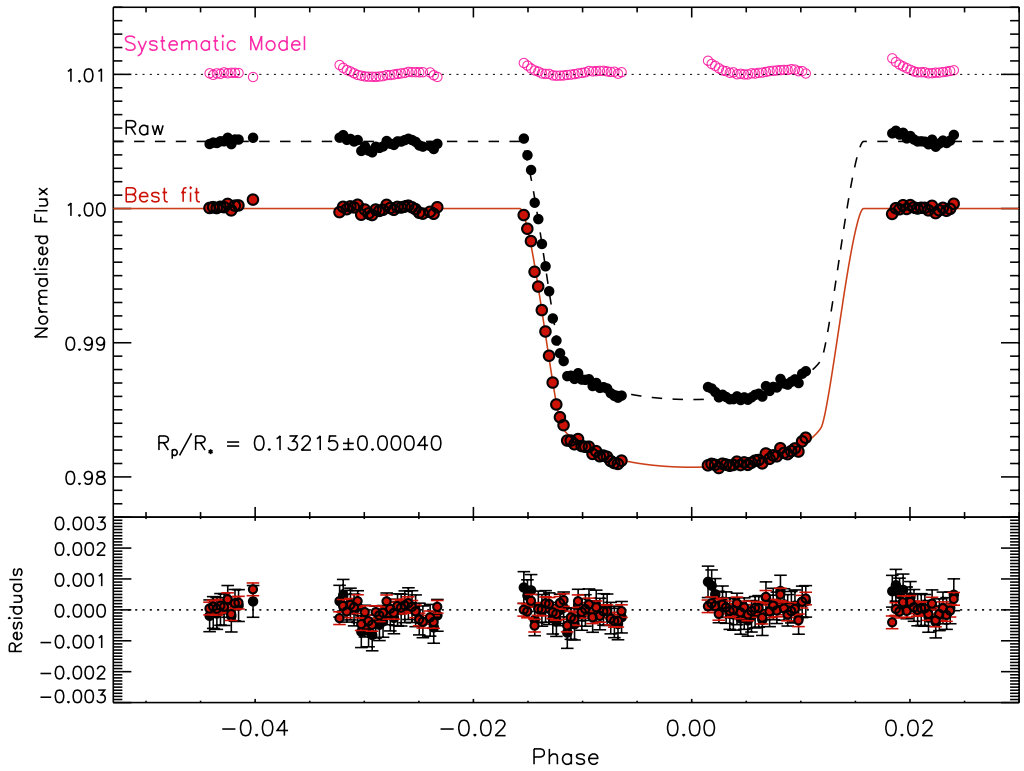

Figure 3.2.17: XO-1 raw white lightcurve (black-middle) and the corrected white lightcurve (red-bottom) after dividing through by the most favoured systematic model (pink-top). The lightcurves are offset in flux for clarity. The bottom plot shows the residuals of both lightcurves relative to the displayed models, and the associated uncertainties.

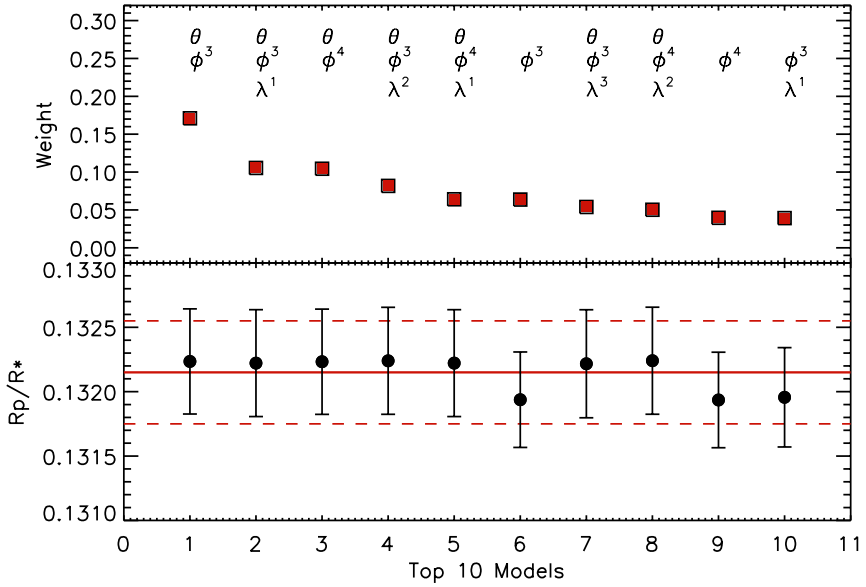

Figure 3.2.18: Top: Weighting for the top 10 models fit to the white lightcurve based on the AIC approximation. The model parameters are outlined below each model with best to worst from left to right (symbols same as Fig. 3.2.4). Bottom: The computed R_p/R_* and uncertainty for each of the models as in the top plot. The solid horizontal line represents the final marginalised radius ratio with the dashed lines marking the uncertainty range.

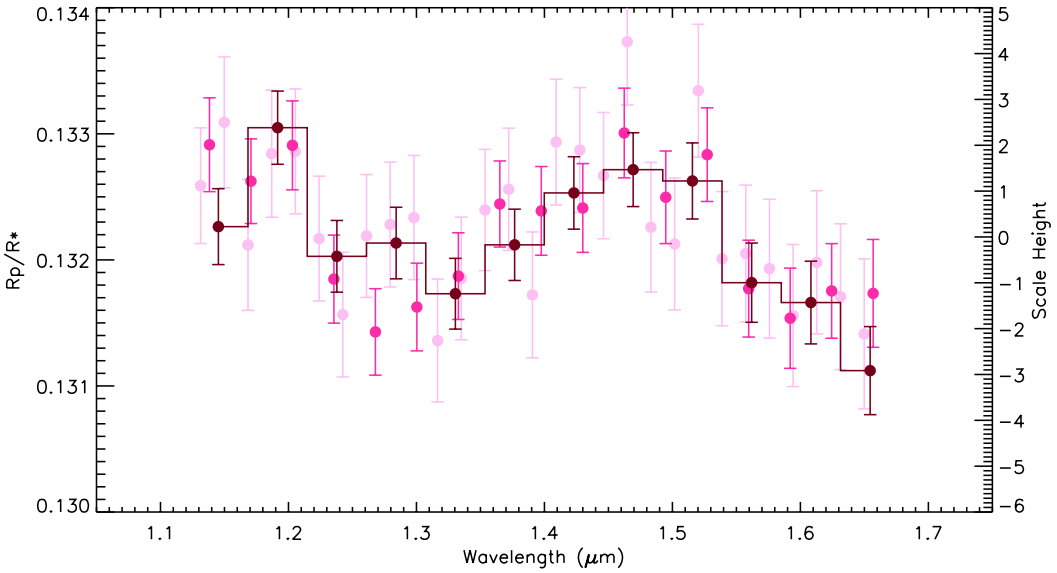

Figure 3.2.19: XO-1b transmission spectrum measured for a series of pixel bandwidths: 4 pixels (light pink), 7 pixels (pink), and 10 pixels (dark red). The transmission spectrum is computed across 10 pixels (463 Å) and we use this data for the following analysis.

models to obtain a $R_p/R_* = 0.13215 \pm 0.00040$. In Fig. 3.2.18 we show the weight calculated from the AIC approximation for the top ten systematic models fit to the white lightcurve. From this it is clear to see that the dominant systematic is the "HST breathing" effect, which requires a third or fourth order polynomial correction in each of the top ten cases. However, it is also clear to see that the linear correction for a visit-long slope is also favoured as it appears to have a significant effect on the computed R_p/R_*.

Transmission spectrum

We restrict the wavelength range examined for the transmission spectrum of XO-1b from 1.12 to 1.69 µm, which is restricted in the red end of the spectrum by the edge of the subarray. We compute the transmission spectrum by summing the flux of each spectrum into small wavelength bins and determining the R_p/R_* for each bin. We first remove any points of the individual spectroscopic lightcurves which deviate from the transit model by more than 4σ. A systematic model correction is applied using the best-fitting model as determined by the white lightcurve. The resultant

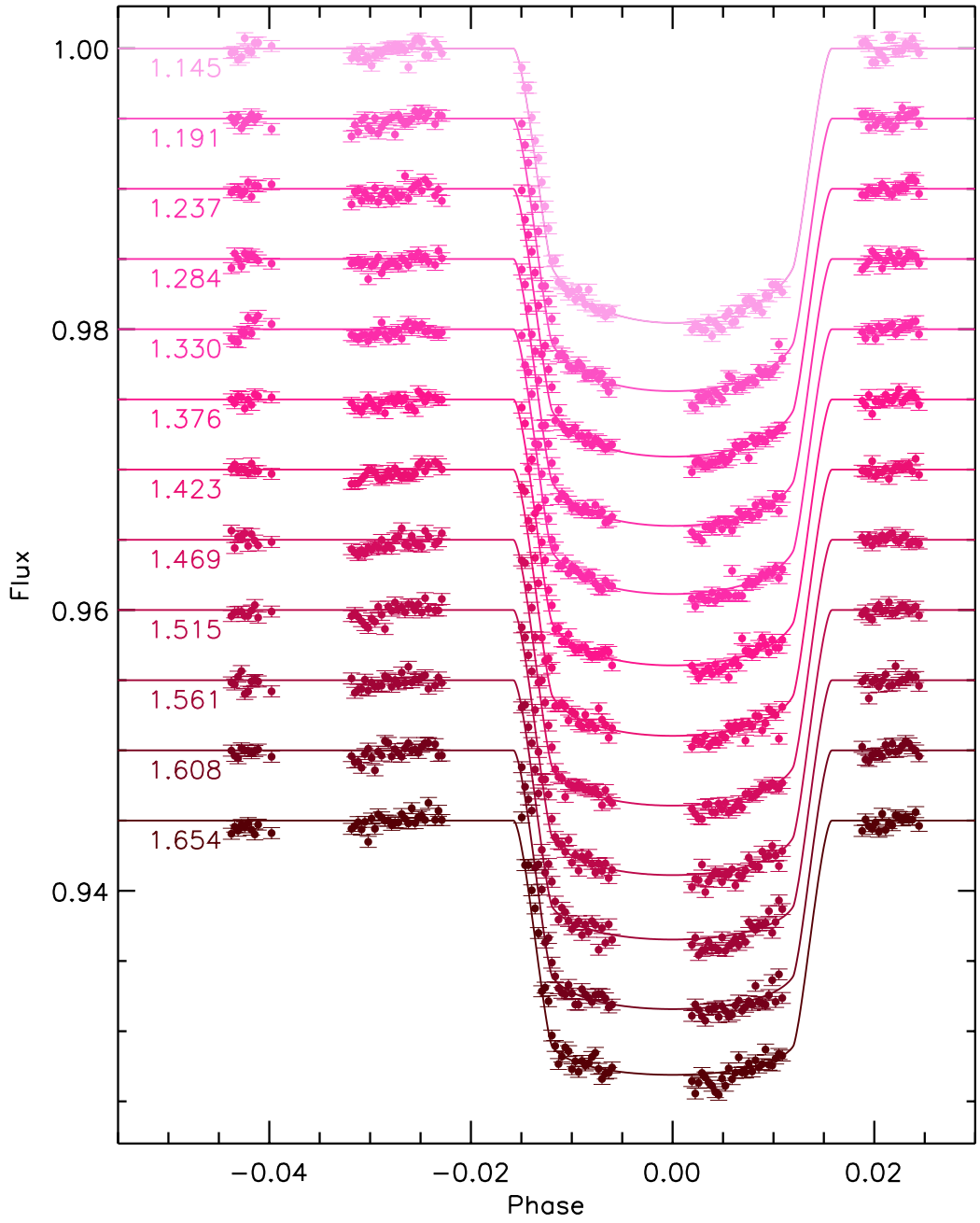

Figure 3.2.20: XO-1b spectroscopic lightcurves for bins of 10 pixels between 1.12–1.69 µm. Each lightcurve is offset in flux for clarity.

Table 3.2.4: Table of transmission spectral properties of XO-1b reduction at bins of 10 pixels, with the corresponding limb-darkening parameters following the four-parameter non-linear limb-darkening law.

Wavelength	Rp/R*	σ	c1	c2	c3	c4
1.1452	0.13226	0.00030	0.35229	0.59114	-0.58934	0.22840
1.1915	0.13304	0.00029	0.57916	-0.14252	0.29760	-0.17251
1.2378	0.13202	0.00028	0.58624	-0.16321	0.30590	-0.17213
1.2841	0.13213	0.00028	0.51042	0.20877	-0.20602	0.04031
1.3304	0.13173	0.00028	0.52242	0.14844	-0.12516	0.00317
1.3767	0.13211	0.00028	0.49832	0.29345	-0.34196	0.09910
1.4230	0.13253	0.00028	0.49275	0.51466	-0.73446	0.28024
1.4693	0.13271	0.00029	0.55253	0.26239	-0.43379	0.15796
1.5156	0.13262	0.00030	0.56613	0.38131	-0.66366	0.26786
1.5619	0.13181	0.00031	0.68081	0.09551	-0.44392	0.20528
1.6082	0.13166	0.00032	0.68180	0.08084	-0.42294	0.19660
1.6545	0.13112	0.00034	0.72615	0.00209	-0.42299	0.21342

transmission spectrum computed for wavelength bins of $\Delta\lambda = 185$, 324, and 463 Å (4, 7, and 10 pixels) is shown in Fig. 3.2.19. It is clear to see from the overall shape of the transmission spectrum, that there is potentially a small feature corresponding to the absorption of H_2O at 1.4 µm. However, the equally enhanced absorption at the blue end of the spectrum at ∼1.19 µm may contradict this when we later fit the transmission spectra to atmospheric models in §3.4. Small differences can be seen between the transmission spectrum for each bin size, with apparent disconnection between the measured depth in the largest bin and the measured depth in the smaller bins over the same wavelength region. These difference often occur when the edges of the smaller bins lie within stellar absorption lines compared to larger bin widths, which span the whole of the drop in stellar flux over the small wavelength ranges. This is especially prominent around the Paschen-beta stellar absorption lines at 1.28 µm where the measured radius ratio between the larger and smaller bins is on the level of 1σ. The effect of this on the shape of the spectrum is easily investigated by shifting the starting and ending pixel of the wavelength range investigated for the transmission spectrum moving the bin edges outside of prominent stellar absorption lines. We discuss this further in §3.2.4 with regards to the effects on the transmission spectrum of HD 209458b

We highlight the transmission spectrum computed for bins of 463 Å (10 pixels) and list the R_p/R_* values and uncertainties in Table 3.2.4. Figure 3.2.20 also shows each of the individual spectroscopic lightcurves for this transmission spectral resolution,

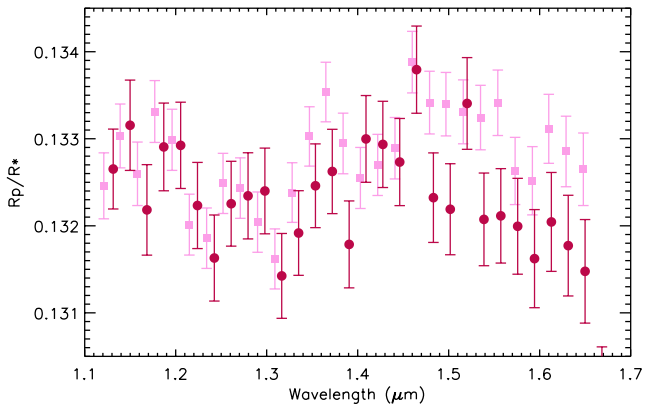

Figure 3.2.21: XO-1b transmission spectrum with a bin width of 185 Å (dark circles) compared the previously published transmission spectrum of Deming et al. (2013) (light squares).

which indicate any potential outliers in the spectrum. We compare our computed transmission spectrum to the previously published results of this dataset by Deming et al. (2013), which shows a similar amplitude feature at 1.19 µm (see Fig. 3.2.21).

Deming et al. (2013) applies a differential correction to each of the individually extracted spectra by dividing by a template spectrum of the target star. This method effectively applies a common-mode removal to each of the individual spectra prior to the construction of the spectroscopic lightcurves. We can see from the analysis of the XO-1b transit data that both analysis methods are able to produce a transmission spectrum which has the same overall structure, producing a muted H_2O absorption feature at 1.4 µm. We do note slight changes in the two different methods used to account for shifts in wavelength that have the potential to cause significant differences in the transmission spectrum. We outline these differences in the following analysis of the HD 209458b WFC3 transit data.

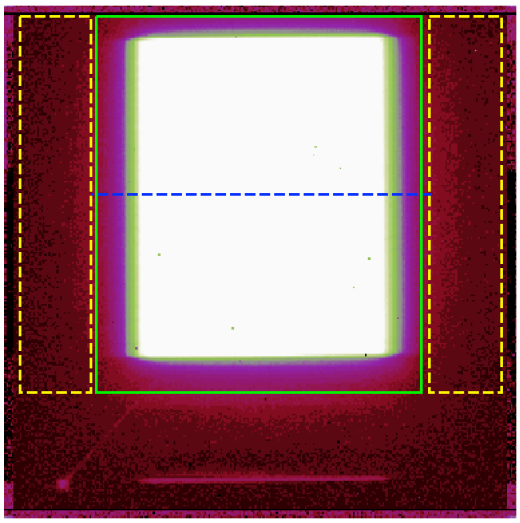

Figure 3.2.22: Single image of *ima* exposure of HD 209458 in spatial scan mode. The boxes outline the full frame cut out of the subarray encompassing the spectral trace (green box) and the background regions (yellow dashed boxes), with the blue dashed line representing the central trace.

3.2.4 HD 209458b

After the discovery of HD 209458 via radial velocity measurements (Henry et al. 2000; Mazeh et al. 2000), it became the first exoplanet to be observed transiting its host star via both photometric and spectroscopic observations (Queloz et al. 2000; Charbonneau et al. 2000). HD 209458b rapidly became one of the most studied hot Jupiters, as it orbits a bright star (V Mag = 7.7) in a period of 3.524 days, offering numerous opportunities for study with both ground- and space-based telescopes (e.g. Brown et al. 2001; Charbonneau et al. 2002; Narita et al. 2005; Knutson et al. 2007a; Sing et al. 2008; Snellen et al. 2008; Vidal-Madjar et al. 2011; Deming et al. 2013). Multi-wavelength observations have effectively probed different layers of the planet's atmosphere confirming the presence of an inflated H_2 atmosphere (Ballester et al. 2007; Lecavelier des Etangs et al. 2008; Ben-Jaffel 2007) and the presence of molecules deeper in the planets atmosphere with near-IR detections of CO and H_2O (Snellen et al. 2010; Deming et al. 2013).

We have reanalysed the single transit of HD 209458b observed with HST WFC3 on September 30th 2011, one of the first spatial scan observations conducted with WFC3 using the G141 spectroscopic grism (Deming et al. 2013). These observations were part of the large HST programme headed by P.I. D. Deming (HST GO 12181, see Table 3.1.1).

As HD 209458b orbits one of the brightest known exoplanet host stars, observations were conducted with a rapid scan rate of ∼7.43 pixels per second so that the count rate per pixel did not enter the non-linear regime of the detector. The resultant

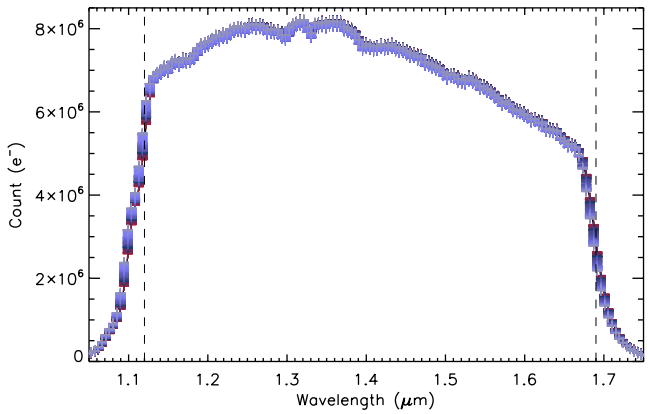

Figure 3.2.23: All spectra of HD 209458 cross-correlated and overplotted on a scale of wavelength vs. count. The vertical dashed lines represent the wavelength cut off used in the transmission spectral analysis.

spectral trace covers over 160 pixels in the cross-dispersion direction on the detector, and a total of 31% of the subarray. As a result of this a background region equal to the scan area is not available on the subarray image. We therefore compute the background level by using the count level alongside the exposed target spectrum (see Fig. 3.2.22). Using this we can extrapolate the count rate across the region of the subarray exposed to the stellar spectral trace with a simple linear function fit across the two regions in each cross-dispersion pixel row (see § 2.3.3).

We trimmed a 170×200 box around each spectral image and extracted the spectra using an aperture of ±83 pixels around the computed centring profile, which was found to be consistent across the spectrum with an error of 0.005 pixels. The extracted spectrum of HD 209458 was found to vary by ∼0.18 pixels in the wavelength direction over the course of the transit. This deviation across pixels plays a significant role in the overall systematics of the data, which are determined by cross-correlating the measured shifts with the raw white lightcurve residuals (see Fig. 3.1.1). The impact of this can more readily be seen in the individual spectroscopic band-passes where sub-pixel deviations in the wavelength solution can affect the computed transmission spectrum. We discuss these effects in more detail later on in this analysis.

White lightcurve

We compute the white lightcurve with both the first orbit and a subsequent five exposures removed. The additional five exposures occur at the start of an exposure sequence following each buffer dump and are found to be greater than 4σ from the residual scatter of the spectra. The final lightcurve is composed of 109 exposures over the remaining 4 HST orbits. The raw lightcurve is calculated by summing up the flux over the entire wavelength range covered by the target spectrum, from 1.00 to

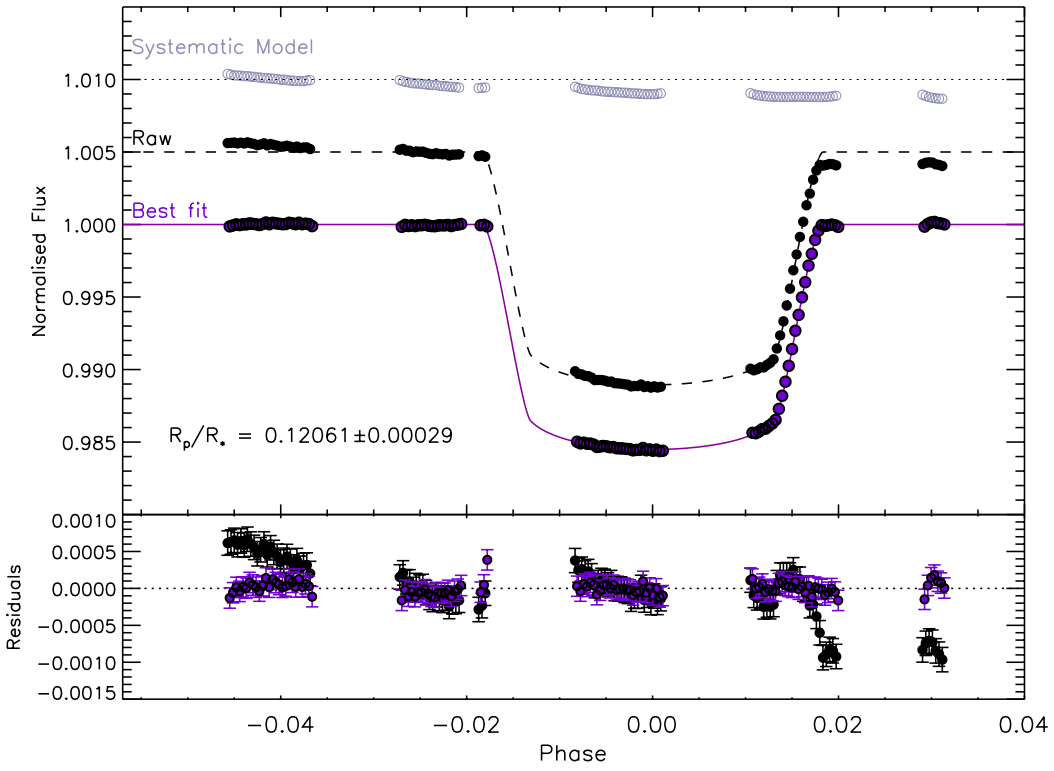

Figure 3.2.24: HD 209458 raw white lightcurve (black-middle) and the corrected white lightcurve (purple-bottom) after dividing through with the most favoured systematic model (light purple-top). The lightcurves are offset in flux for clarity. The bottom plot shows the residuals relative to the model transit lightcurves. From this it is clear to see the dominant visit-long slope across the whole timeseries.

1.78 µm, in each exposure. To compute the Mandel & Agol (2002) transit model we use the system parameters stated in Deming et al. (2013), fixing the inclination to 86.59° and a/R_* to 8.859 (see Table 3.2.1). While one of the orbits covers the entire egress of the planetary transit, which can give information as to the inclination of the planetary orbit, the total phase coverage is not sufficient to constrain the parameters greater than those previously published.

We fit the white lightcurve for our grid of systematic models and determine that the most favoured systematic model used to correct the data is,

$$model = \sum_{i=1}^{4} p_i \phi^i + \sum_{j=1}^{3} l_j \lambda^j. \tag{3.4}$$

This suggests that the overall slope observed in the raw white lightcurve (see Fig. 3.2.24,

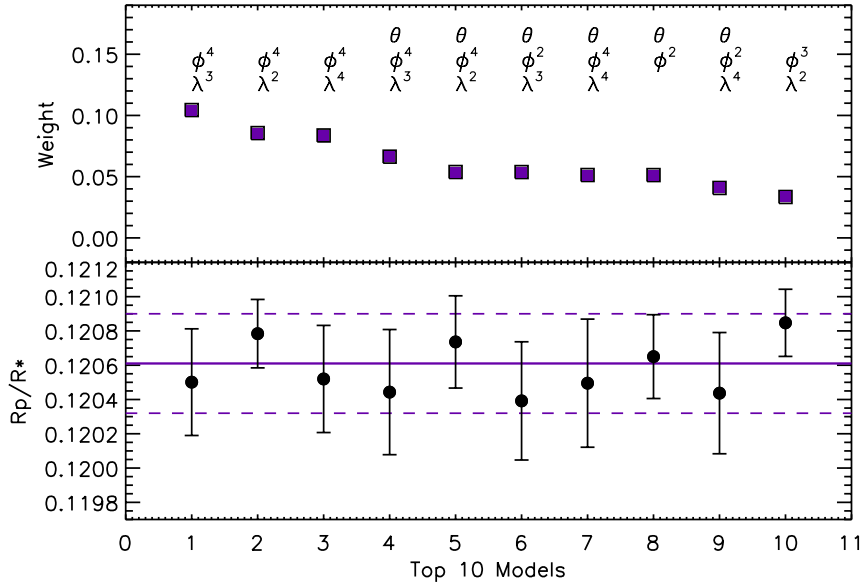

Figure 3.2.25: Top: Weighting for the top 10 models fit to the white lightcurve based on the AIC approximation. The model parameters are outlined below each model with best to worst from left to right. (symbols same as Fig. 3.2.4) Bottom: The computed R_p/R_* and uncertainty for each of the models as in the top plot. The solid horizontal line represents the final marginalised radius ratio with the dashed lines marking the uncertainty range.

black) can be corrected with a combination of a high order polynomial in HST phase with additional polynomial corrections in wavelength shift. The correlation between the change in wavelength over the period of the planetary transit observations can be seen in Fig. 3.1.2, which is reflected in the best-fitting model. In Fig. 3.2.24 we show the corrected white lightcurve using the most favoured systematic model; the visit-long slope is likely accounted for by our wavelength corrections as they are correlated in this case. Figure 3.2.25 shows the systematic parameters favoured for our top ten models used to correct the white lightcurve data with the corresponding weighting based on the AIC approximation, and the measured R_p/R_* and uncertainties from the lightcurve based on each corrected lightcurve.

We compute a marginalised $R_p/R_* = 0.12061 \pm 0.00029$ from all 52 systematic models, weighted according to the evidence based on the AIC approximation. The scatter on the corrected white lightcurve residuals is small compared to that of HAT-P-1 and WASP-31, likely due to the number of photons that can be collected for this very bright target star when using spatial scan mode with WFC3. In the bottom of Fig. 3.2.25 the marginalised R_p/R_* is shown as coloured horizontal lines relative to the measured values from the lightcurves corrected by the top ten systematic models.

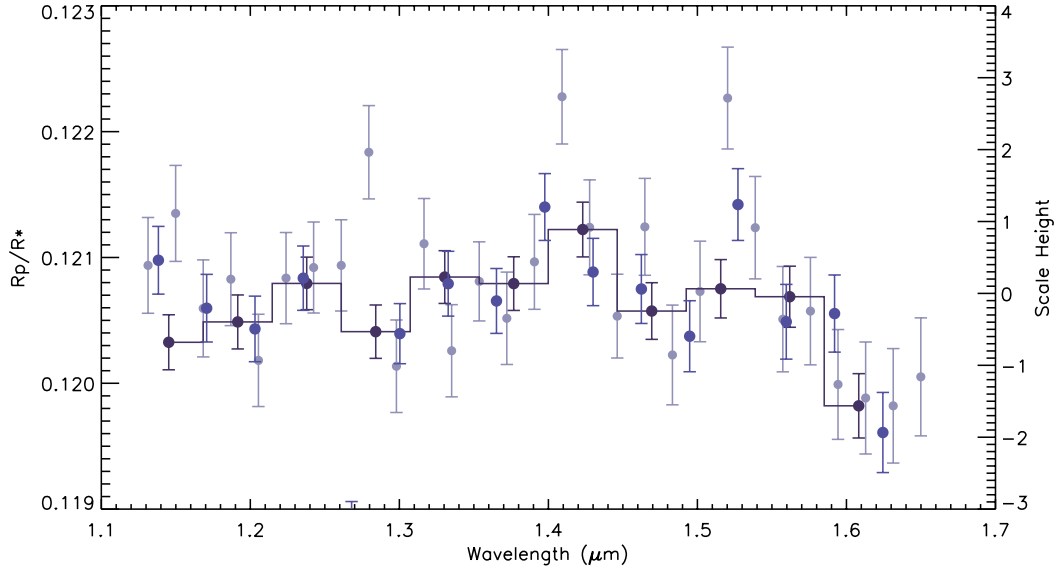

Figure 3.2.26: HD 209458b transmission spectrum measured for a series of binwidths, 4 pixels (light purple), 7 pixels (purple), and 10 pixels (dark purple). The transmission spectrum computed with a binwidth of 10 pixels is picked out with the dark purple histogram and used for subsequent analysis.

It can be seen that there is a slight inflation in the uncertainty measured using the marginalisation technique compared to the individual measurements. This is likely due to the scatter of the measured values between the most favoured models, which is not observed as clearly in other datasets for example WASP-31 (see Fig. 3.2.11).

Transmission spectrum

We restrict the wavelength range examined for the transmission spectrum of HD 209458b from 1.12 to 1.69 µm, removing the effect of the strongly sloped spectral edges of the grism response. Figure 3.2.26 shows the transmission spectrum for HD 209458b computed at a series of binsizes, 4, 7, and 10 pixels, covering the equivalent bandpasses of 185, 324, 463 µm. It can be seen in the transmission spectrum that the 4 pixel bins have four distinct outliers; we find that these are the result of the edge of bandpasses falling in distinct stellar lines affecting the flux in that bin, similar to that seen in the transmission spectrum of XO-1b at the Paschen-beta stellar absorption lines. We again note that this can be avoided by easily adjusting the width or position of the bandpass in each case or increasing the bin width to encompass the entire stellar

Table 3.2.5: Table of the transmission spectrum measured for HD 209458b using bins of 10 pixels. We also list the limb-darkening coefficients used in the four parameter non-linear limb-darkening law for each bin.

Wavelength	Rp/R*	σ	c1	c2	c3	c4
1.1452	0.12032	0.00021	0.39557	0.48045	-0.41943	0.11549
1.1915	0.12048	0.00021	0.53826	0.01536	0.057448	-0.06829
1.2378	0.12079	0.00020	0.54428	-0.01074	0.07998	-0.07545
1.2841	0.12041	0.00021	0.47865	0.34072	-0.43009	0.14447
1.3304	0.12084	0.00020	0.49555	0.26848	-0.33844	0.10429
1.3767	0.12079	0.00021	0.47916	0.38217	-0.51672	0.18495
1.4230	0.12122	0.00021	0.49428	0.53409	-0.83613	0.34179
1.4693	0.12057	0.00022	0.53972	0.30698	-0.55242	0.22414
1.5156	0.12075	0.00023	0.57523	0.34163	-0.66424	0.27859
1.5619	0.12068	0.00024	0.67243	0.08902	-0.48068	0.23488
1.6082	0.11982	0.00025	0.67206	0.07680	-0.46091	0.22620

absorption feature smoothing out the effect in the resultant transmission spectrum.

For our comparative analysis we bin the spectrum into 11 spectroscopic channels each with a bin width of 463 µm over a total of 10 pixels on the detector, shown in Fig. 3.2.26 as dark joined points. Table 3.2.5 and Fig. 3.2.27 document each of the individual spectroscopic lightcurves and their R_p/R_* parameters and uncertainties for this specific bandpass, with the associated limb-darkening parameters also listed.

The resultant transmission spectrum does not show any of the expected absorption features for hot Jupiter atmospheres like that of HD 209458b, where H_2O should be well mixed throughout the upper atmosphere of the planet. We compare our computed transmission spectrum to that of the previously published results in Deming et al. (2013), which shows a distinct increase in absorption at ∼1.35 µm (see Fig. 3.2.28). Deming et al. (2013) conclude that this additional absorption observed in the transmission spectrum is the result of a muted H_2O feature obscured by an additional grey opacity source in the planetary atmosphere. In our re-analysis we are not able to measure an absorption feature in the transmission spectrum, with the scatter observed in our reduction increasing over the expected H_2O absorption band.

From this analysis, and that outlined in Deming et al. (2013), we determine that the differences in the computed transmission spectra are the result of the pixel sized deviation on the detector in the wavelength direction. From our analysis of XO-1 we can see that when the wavelength variation over the course of the observations is small, we are able to match the published transmission spectrum to within the 1σ

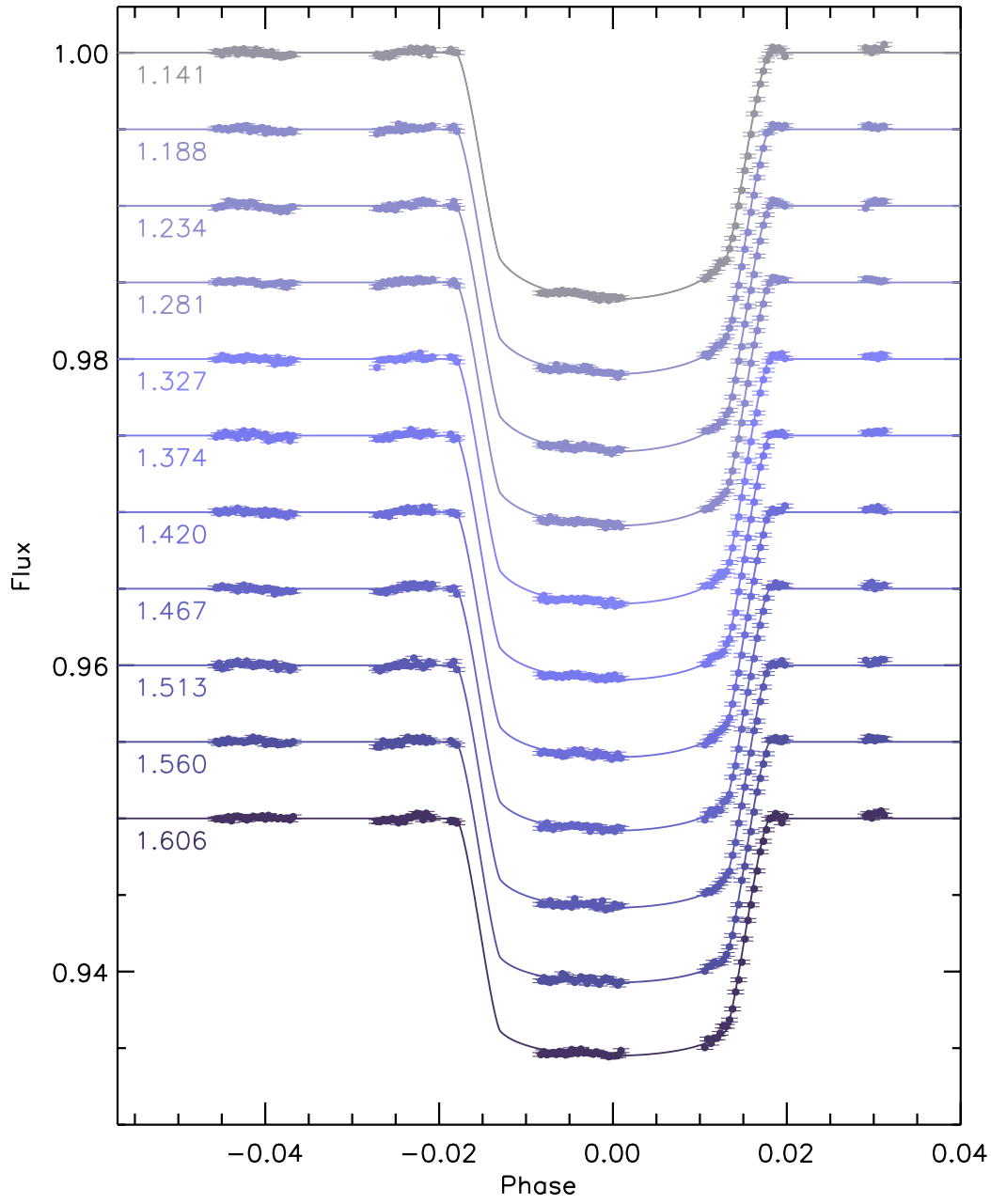

Figure 3.2.27: Spectroscopic lightcurves of HD 209458 with $\Delta\lambda = 463$ Å. The lightcurves are offset in flux for clarity.

uncertainties. To construct our spectroscopic lightcurves we bin our spectra on a pixel by pixel basis defined by the wavelength solution computed on the pixel scale across the spectral trace. This limits our spectroscopic bins to pixel level wavelength change setting a hard cut off on the shifts in wavelength. This will not impact the overall transmission spectrum for small sub-pixel variations in wavelength over the course of a transit observation, as is the case for all other observations. However, the large shifts in the wavelength of the spectral trace on the detector that are observed over the course of HD 209458b's transit in the WFC3 dataset introduce pixel scale variations to the spectroscopic lightcurves. This has a larger impact on the computed spectroscopic lightcurves where the wavelength solution places sub-pixels into incorrect spectral bins for specific exposures across the course of the visit.

To account for this sub-pixel change in the spectral wavelength solution across each exposure, Deming et al. (2013) introduced a spectral template technique to the extracted stellar spectrum from each image. The template spectrum is constructed from the average observed spectrum from exposures within 1 hour of 1st and 4th contact. The template is then used to fit the wavelength solution to each exposure spectrum by shifting it in wavelength stepping through small increments to determine the best fit solution. The individual spectra are then divided by the template spectrum to create residuals effectively removing any additional background contributions and the wavelength shift on the detector. This method also allows for the cancellation of common-mode systematics, similar to the divide-oot method outlined by Berta et al. (2012); however, this requires the common-mode systematics to be consistent in wavelength rather than in time.

From this we can see that our treatment of the shift in wavelength across the course of the observations should be modified to take into account a significant shift as shown for HD 209458b.

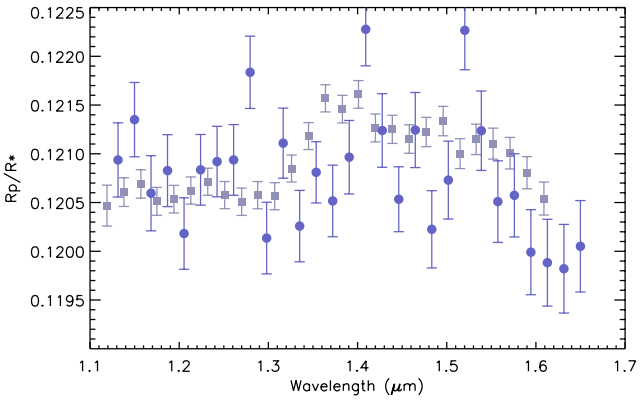

Figure 3.2.28: HD 209458b transmission spectrum with a bin width of 185 Å (dark circles) compared to the previously published transmission spectrum of Deming et al. (2013) (light squares).

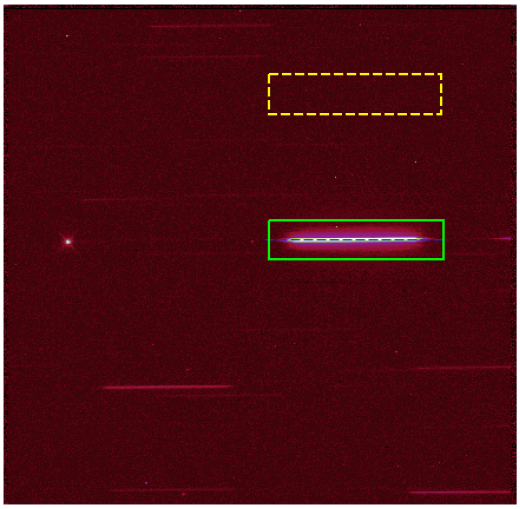

Figure 3.2.29: Image of a single *ima* exposure of WASP-17. The green box outlines the region extracted from the subarray with the centring profile marked by a blue dashed line. The yellow dashed region surrounds the clean region of the subarry used for background subtraction.

3.2.5 WASP-17b

WASP-17b is a very low density exoplanet ($\rho_p = 0.92\,\mathrm{g/cm^3}$) with a significantly inflated radius, R_p=1.932 R_J, and currently the largest known transiting exoplanet (Southworth et al. 2012). Radial velocity observations obtained during transit show that WASP-17b is in a retrograde orbit compared to the rotation of its host star (Anderson et al. 2010; Bayliss et al. 2010; Triaud et al. 2010). Additionally, Southworth et al. (2012) report an equilibrium temperature of 1775 K noting that planets with large inflated radii often orbit stars hotter than 6000 K with masses exceeding 1.15 $M_\odot$. The high equilibrium temperature and low surface gravity result in an extensive atmospheric scale height over 2000 km, making this planet ideal for transmission spectral studies.

A single transit of WASP-17b was observed with HST WFC3 on July 8th 2011,

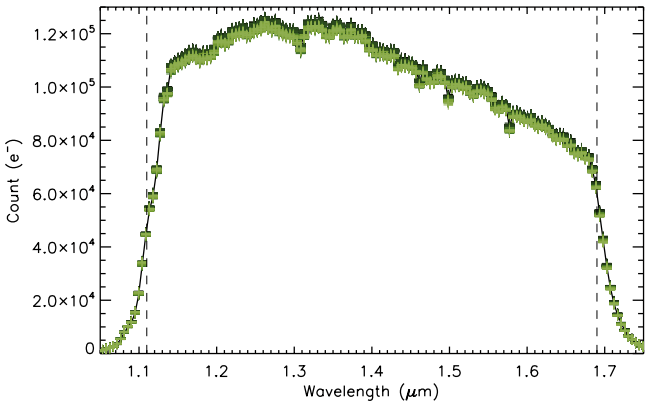

Figure 3.2.30: All spectra of WASP-17 cross-correlated and overplotted on a scale of wavelength vs. count. The vertical dashed lines represent the wavelength cut off used in the transmission spectral analysis.

prior to the introduction of spacial scan mode to WFC3 in September of 2011. Observations of WASP-17b were conducted in stare mode using the G141 spectroscopic IR grism as part of the GO 12181 large HST programme lead by P.I. D. Deming. Stare mode exposures were obtained with an exposure time of 12.795 s using a 512×512 subarray frame. The combination of bright target star (V Mag = 11.6) and relatively long exposure time resulted in a peak pixel count of ∼64,000, which breaches the non-linearity regime of WFC3. This has been previously shown to impact the systematics observed in the lightcurve, causing a reduction in flux over the course of sub-orbit timeframes (e.g. Berta et al. 2012; Huitson et al. 2013; Mandell et al. 2013).

To extract each of the spectral traces we trimmed a 173×40 box around each spectral image and summed the flux over an aperture of ±3 pixels around the computed centring profile, which was found to be consistent across the spectrum with an error of 0.06 pixels. Background subtraction was applied using a clean region of the untrimmed image (see Fig. 3.2.29).

White lightcurve

The white lightcurve for WASP-17 is computed with the first orbit removed, reducing the total number of exposures from 130 to 107 over the course of the visit. The raw lightcurve is computed by summing the flux across the whole spectral range for each exposure. We use the system parameters derived from a joint fit across HST STIS band-passes (Ballester et al. in prep.) fixing the inclination to $i = 86.91716°$ and centre of transit time to 2455750.7973239 JD.

It can clearly be seen in Fig. 3.2.31 that there is a strong 'hook' feature present in the raw data, with an orbit-to-orbit repeating pattern in the residuals. The grid

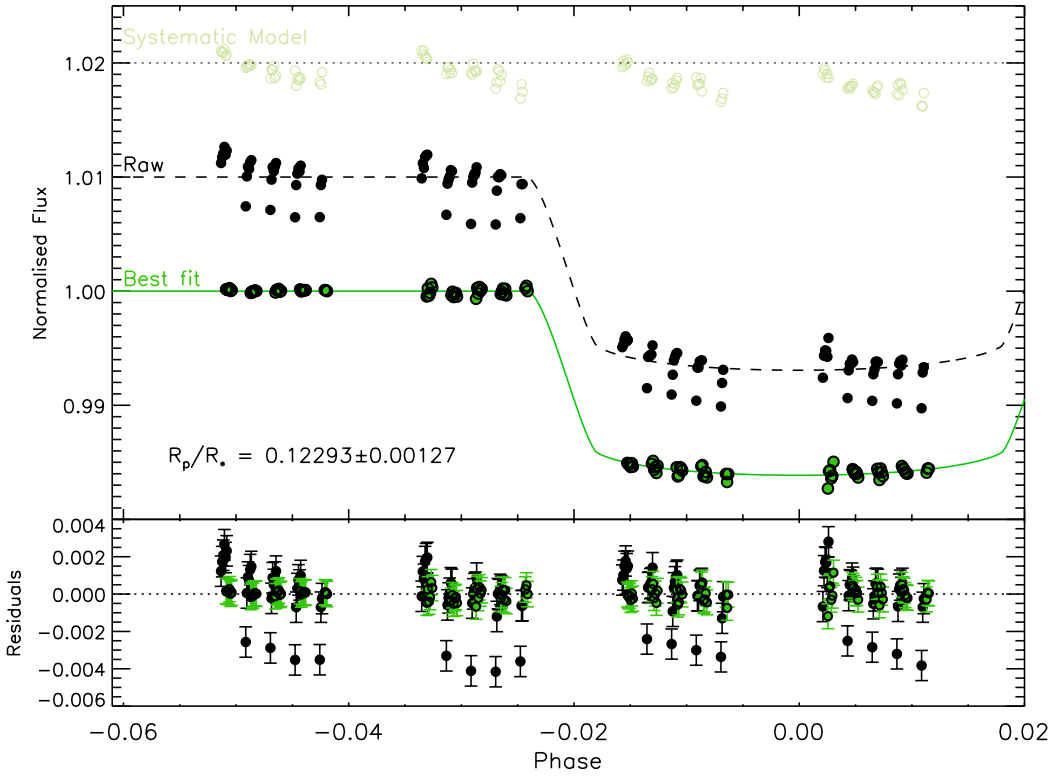

Figure 3.2.31: Raw WASP-17 white lightcurve (black-middle) and the corrected white lightcurve (green-bottom) computed by performing the divide-oot routine with addition systematic correction by dividing through with the most favoured model as determined by the marginalisation (light green-top). The lightcurves are offset in flux for clarity. The bottom plot shows the residuals for each fit compared to the displayed analytic transit model.

of systematic models used to correct the white lightcurve do not accurately account for this 'hook'. To effectively correct for this systematic in the white lightcurve we use the divide-oot routine derived by Berta et al. (2012), which removes common-mode time-dependent systematics. We then additionally apply a marginalisation over the parametrised and exponential systematic models to remove any additional time-independent systematics and determine the planet-to-star radius ratio. Figure 3.2.31 shows the white lightcurve corrected using divide-oot and the computed best-fitting systematic model following the AIC approximation,

$$model = T_1\theta + \sum_{i=1}^{3} p_i\phi^i + \sum_{j=1}^{2} l_j\lambda^j. \tag{3.5}$$

Following the BIC approximation, which tends to favour more simple models, the most favoured systematic correction model $= T_1\theta + p_1\phi$. This demonstrates that the major impacting systematics on this lightcurve, once the time-dependent 'hook' is accounted for, are the visit-long slope and HST phase trends. We note that due to the lack of exposures following the transit the greatest uncertainty on these parameters is in the visit-long slope correction, where the most favoured correction applies a linear fit with a gradient of -0.0149±0.010. The additional HST phase and wavelength corrections favoured following the AIC approximation contribute to a reduction in the marginalised R_p/R_* which is calculated to be 0.12293±0.00127 compared to an uncertainty from the BIC approximation of ±0.00157.

It can be seen in the corrected white lightcurve (Fig. 3.2.31) that the divide-oot routine restricts the use of the out-of-transit orbits for an absolute baseline correction as they are utilised for the 'hook' correction. In addition to this, due to small discrepancies in the repeatability of the observed systematic the divide-oot method is not able to entirely remove the observed 'hook', as can be seen across the first exposures of the 4th orbit.

Figure 3.2.32 shows the top ten systematic correction models favoured by the AIC approximation and their associated weightings used in the marginalisation. From this it is once again clear that the visit-long slope is an important systematic in this dataset greatly impacting the measured R_p/R_* from the transit lightcurve.

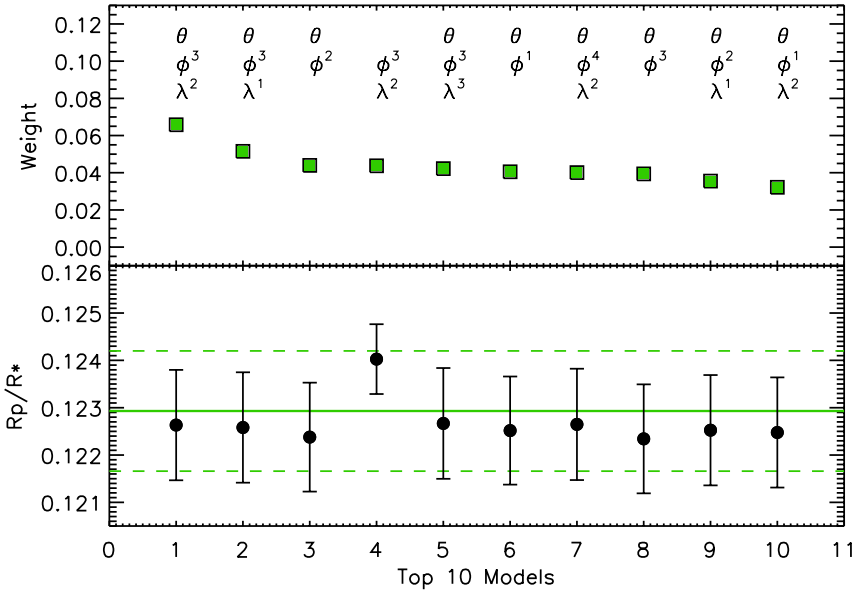

Figure 3.2.32: Top: Weighting for the top 10 models fit to the white lightcurve based on the AIC approximation. The model parameters are outlined below each model with best to worst from left to right (symbols same as Fig. 3.2.4). Bottom: The computed R_p/R_* and uncertainty for each of the models as in the top plot. The solid horizontal line represents the final marginalised radius ratio with the dashed lines marking the uncertainty range.

Transmission spectra

The wavelength range is restricted to 1.11–1.69 µm for the transmission spectrum to reduce the effects of the strongly sloped sides of the grism's spectral response. For each spectroscopic lightcurve we perform our standard common-mode removal technique using the uncorrected white lightcurve residuals. This effectively removes the 'hook' effect in each of the individual lightcurves as it does not appear to be wavelength dependent. We discuss the difference between using our standard common-mode removal and spectroscopically applying the divide-oot technique in § 3.3.1.

We compute the transmission spectrum by binning the stellar spectrum into a number of different wavelength bins covering 4, 7, and 10 pixels on the detector in the wavelength direction. Figure 3.2.30 shows the resultant transmission spectrum computed for each bandpass and the associated uncertainties in each bin. We highlight the transmission spectrum computed over a bin of 10 pixels ($\Delta\lambda$ = 463 Å) and list the specific R_p/R_* values and uncertainties in Table 3.2.6 with the non-linear limb-darkening coefficients used for each bin.

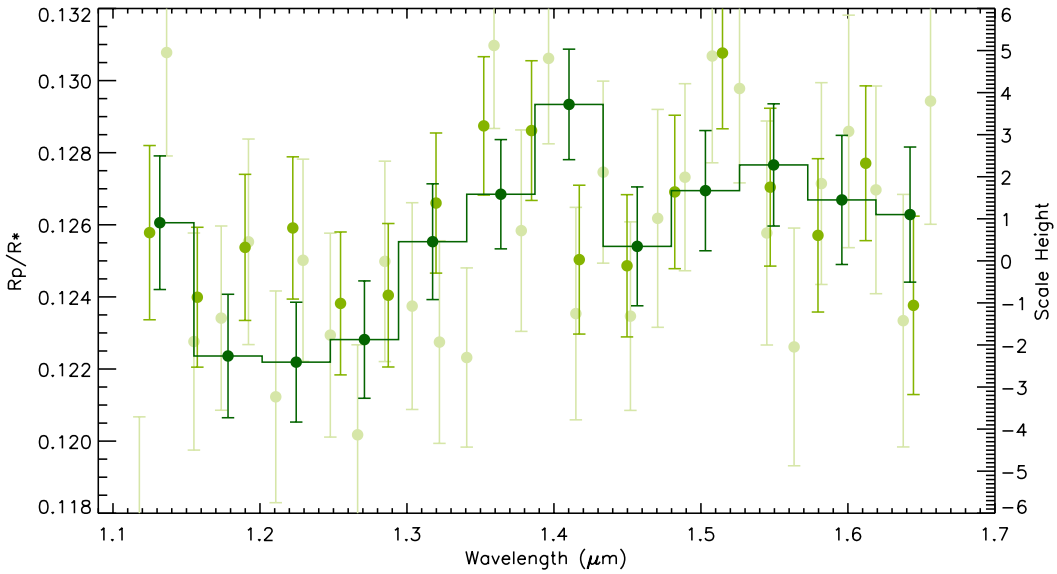

Figure 3.2.33: WASP-17b transmission spectrum measured for a series of binwidths: 4 pixels (light green), 7 pixels (green), and 10 pixels (dark green). The transmission spectrum computed with a binwidth of 10 pixels is picked out with the dark green histogram and used for subsequent analysis.

Table 3.2.6: Table of the transmission spectrum of WASP-17b with a wavelength binsize of ∼463 µm (10 pixels) and the corresponding limb-darkening coefficients for each bin.

Wavelength	Rp/R*	σ	c1	c2	c3	c4
1.1318	0.12605	0.00185	0.39187	0.45517	-0.53905	0.19272
1.1782	0.12236	0.00171	0.40706	0.43109	-0.53245	0.19065
1.2246	0.12219	0.00166	0.47896	0.10298	-0.14042	0.04206
1.2710	0.12281	0.00162	0.36874	0.70165	-0.96698	0.39095
1.3174	0.12553	0.00160	0.40117	0.57273	-0.82050	0.33085
1.3638	0.12684	0.00151	0.40025	0.58765	-0.83270	0.33023
1.4102	0.12933	0.00153	0.49676	0.42907	-0.82476	0.37641
1.4566	0.12540	0.00164	0.49265	0.41303	-0.76712	0.33691
1.5030	0.12694	0.00166	0.51920	0.36094	-0.71416	0.31418
1.5494	0.12766	0.00169	0.66060	0.00131	-0.43681	0.24467
1.5958	0.12669	0.00179	0.64614	0.07075	-0.51243	0.26591
1.6422	0.12628	0.00187	0.66641	-0.02999	-0.39125	0.21797

Figure 3.2.34 shows each of the spectroscopic lightcurves for the 12 channels across the spectrum. From this it can be seen that the common-mode removal effectively removes the strong 'hook' feature with the additional systematics treated with the most favoured systematic correction model from the white lightcurve fit.

We compare our computed transmission spectrum to that of the previously published analysis from Mandell et al. (2013). The displayed transmission spectrum shows many similarities to the previously published values which were computed utilising the divide-oot method with additional linear wavelength and visit-long slope corrections. However, it does not incorporate the uncertainties of these systematics into the displayed errorbars. We find that due to the large uncertainty on the visit-long slope, given the lack of post-transit exposures, the uncertainty associated with each bin is inflated and is a more accurate representation of the observational data.

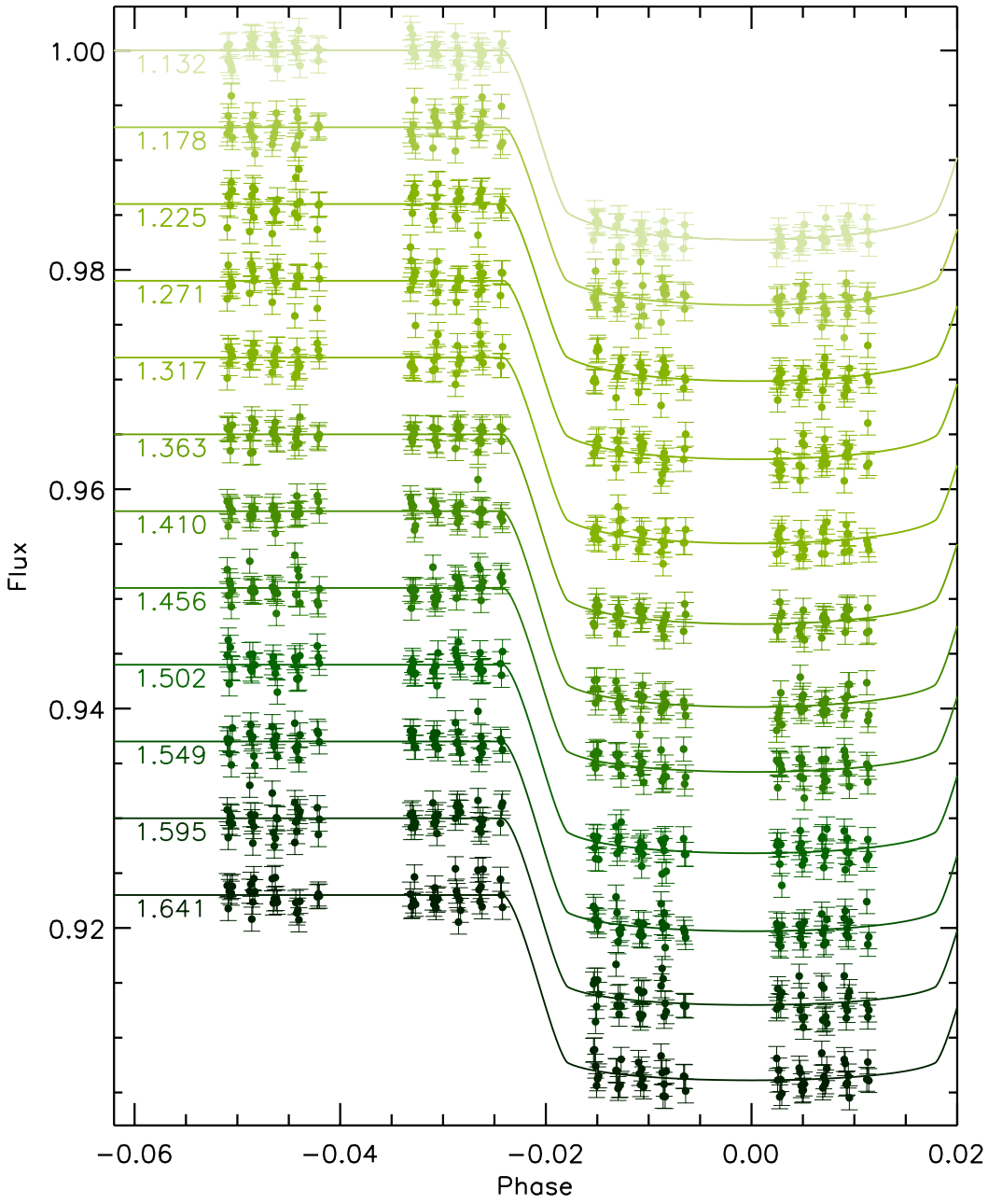

Figure 3.2.34: Spectroscopic lightcurves of WASP-17b when the spectrum is binned up by 10 pixels in the wavelength direction between 1.11–1.69 µm. Each lightcurve is offset in flux for clarity.

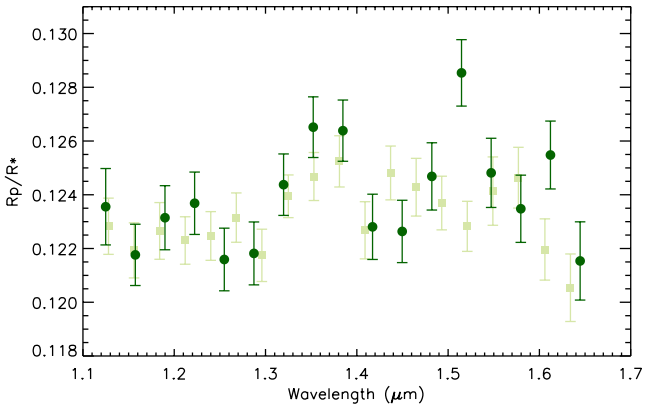

Figure 3.2.35: WASP-17b transmission spectrum with a bin width of 324 Å (dark circles) compared with the previously published transmission spectrum of Mandell et al. (2013) (light squares).

3.2.6 Marginalisation

For each of our datasets we use marginalisation as a tool to compute robust transit parameters from the white lightcurve. This also allows us to determine the main systematics impacting the lightcurves from the different spectral targets in a common and directly comparative manner. Figure 3.2.36 shows the evidence based on the AIC parameter for each systematic model used to correct the white lightcurve following the model numbers in Table 2.6.1. We highlight the model favoured by this criterion corresponding to the systematic corrections with the highest weighting. From each of the fitting statistics it becomes clearer to see the differences across the datasets. For HAT-P-1 there is little difference between a large number of the systematic models with distinct groups of models which correct for only wavelength shifts and no "HST breathing" effects being disfavoured in the final marginalisation. Interestingly, the white lightcurve of WASP-31 does not favour systematic models which only correct for the known "HST breathing" effect, while the introduction of an additional visit-long linear correction makes these models most favourable. The systematic model correction for XO-1 favours higher order polynomials across HST phase and wavelength shift with little difference incurred with or without the visit-long slope. HD 209458 strongly disfavours corrections with only the "HST breathing" effect, with the evidence based on the AIC approximation several hundred points below the other systematic correction fits (these points have been artificially shifted on the scale shown with their original values listed above the shown points). This makes the other systematic models relatively stable in that no model appears to be greatly favoured above any others. This is similarly the case for the WASP-17 data where most models show some favourability with those only correcting for "HST breathing" trends again least favoured in each group of models applied to the data. We also note

that the two exponential models for each of the lightcurves are not heavily favoured and likely contribute negligibly to the resultant transit parameters.

In addition to performing marginalisation on the white lightcurves we also compute the evidence and weighting for each systematic model applied to the individual spectroscopic lightcurves to test the impact on the calculated transmission spectrum. In Fig. 3.2.37 we show the transmission spectrum computed for all of our exoplanet atmospheres using each of the 52 systematic models to correct the spectroscopic lightcurves, and the marginalised transmission spectrum plotted with the single systematic model corrected transmission spectrum. The shape of each transmission spectrum appears robust across most systematic models with variations in the scatter across each of the datasets. HAT-P-1b shows significant variation in the reddest part of the transmission spectrum for a small number of the systematic model corrections; however, this is not represented in the resultant transmission spectrum so is likely the result of negligibly weighted model fits. The only marginalised transmission spectrum to show significant deviation from that computed using the most favoured systematic model from the white lightcurve fits is that of WASP-17b. While most points are still within 1σ of the alternate method, the bluest transmission point deviates over 3σ from the marginalised value. As computing the transmission spectrum for a large number of datapoints for multiple spectroscopic bins is computationally expensive, we use this to demonstrate that using the white lightcurve favoured systematic model is a reasonable approximation to correct the systematics impacting the wavelength dependent channels.

3.3 Tests

There are still a number of differences in the transmission spectra computed here that need to be analysed in more detail. To determine how the different analysis methods and observing modes affect the resultant transmission spectrum we have run a series of analyses to assess each effect in more detail.

Firstly, we assess the use of the divide-oot technique developed by Berta et al. (2012) to calculate the transmission spectrum of WASP-17b and compare it to the method employed in § 3.2.5. We then present the work previously published in Wakeford et al. (2013), which used the observations of HAT-P-1 outlined in § 3.2.1 utilising the additionally observed spectrum of HAT-P-1's companion star to perform differential spectrophotometry (see Fig. 3.2.1).

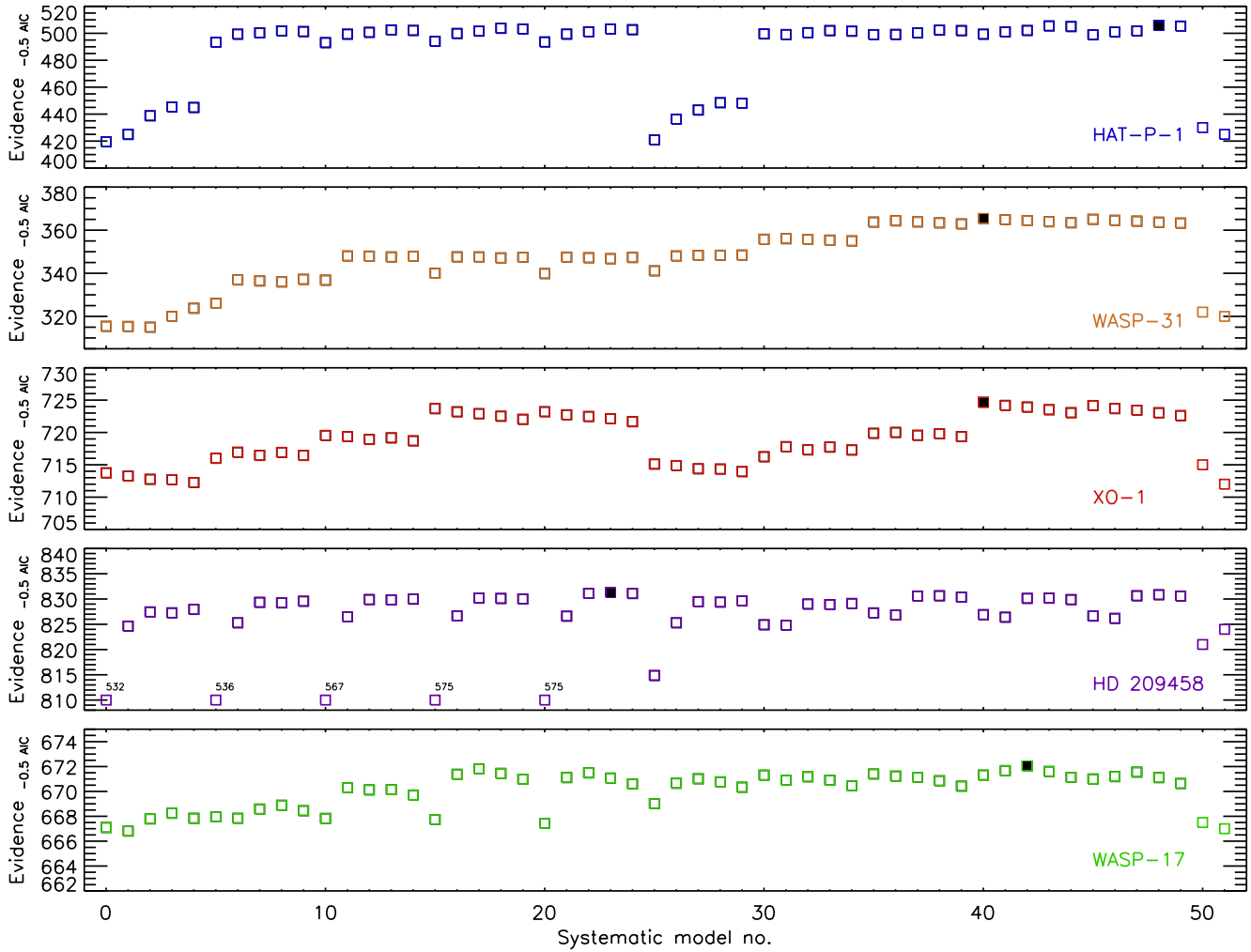

Figure 3.2.36: The evidence based on the AIC approximation for each systematic model applied to the white lightcurve for each exoplanet transit. Top to Bottom: HAT-P-1 (blue), WASP-31 (orange), XO-1 (red), HD 209458 (purple), WASP-17 (green). The best-fitting systematic model for the white lightcurve is filled in with a black square for each planet in each plot.

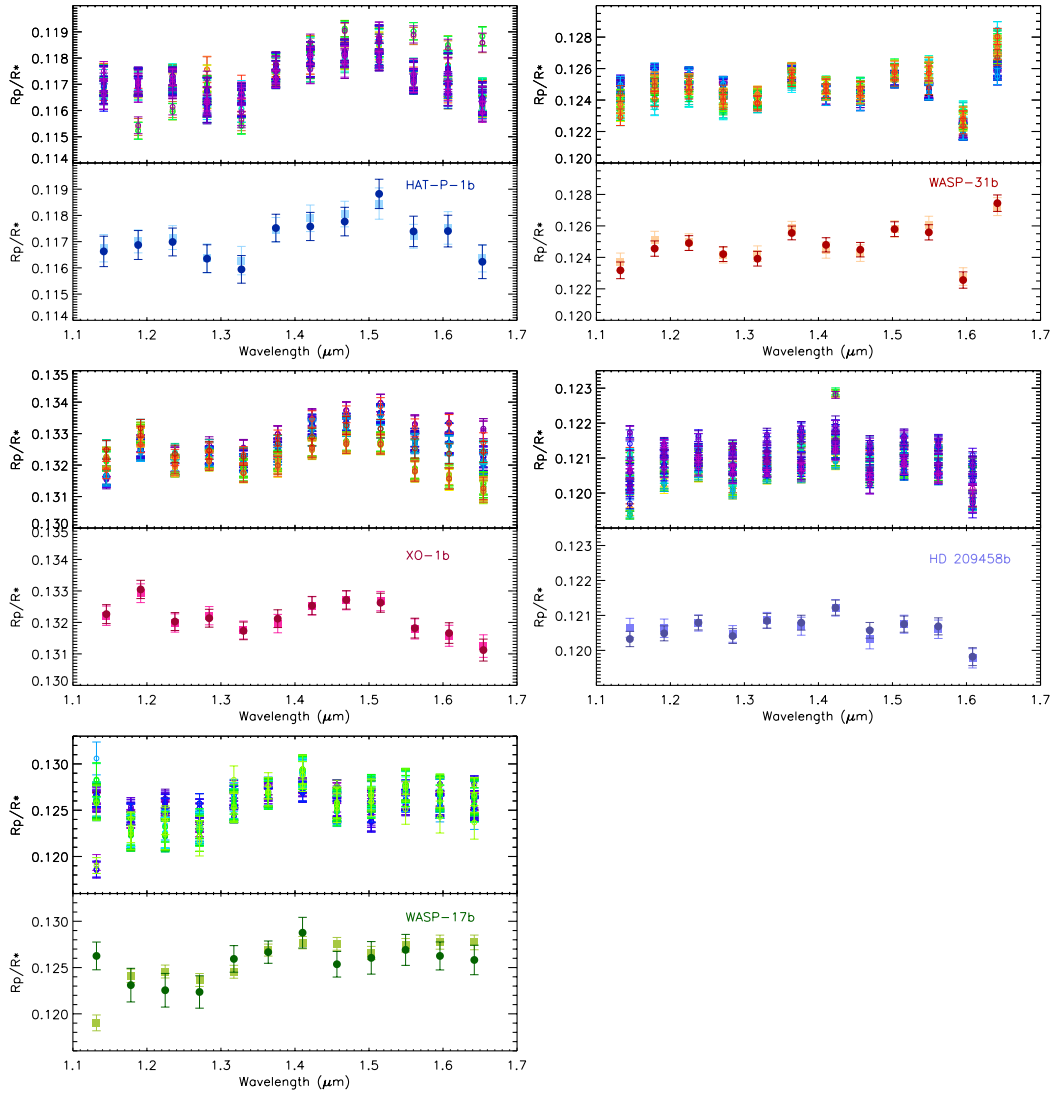

Figure 3.2.37: The marginalised transmission spectrum for each of our five exoplanet atmospheres. Top of each plot: the transmission spectrum for each planet calculated using each of the systematic models outlined in Table 2.6.1. This shows the total dispersion in the R_p/R_* measured for all different systematic corrections applied to the transit lightcurves, highlighting both the robust nature of the transmission spectrum and the need for good systematic model detemination. Bottom of each plot: the transmission spectrum computed using the marginalised R_p/R_* value for each spectral bin (light squares) and the transmission spectrum calculated using the best-fitting systematic model as determined from the white lightcurve analysis of each planetary transit (dark circles).

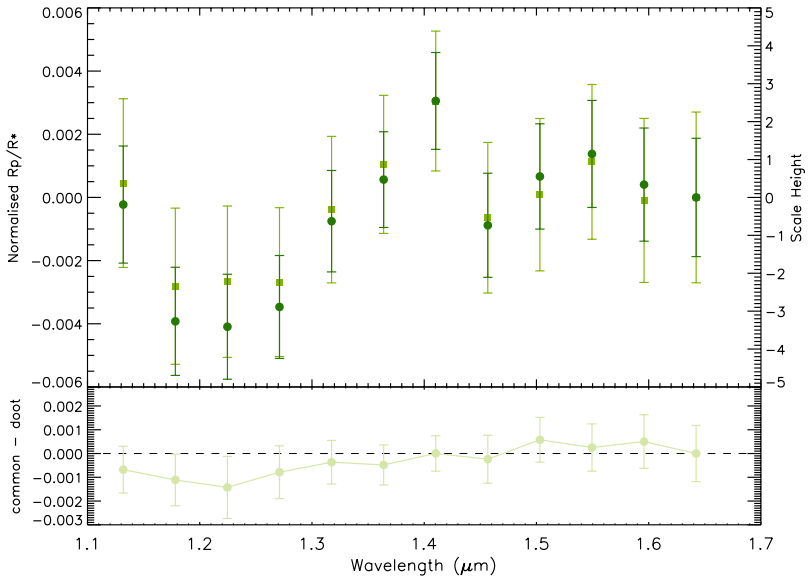

Figure 3.3.1: Top: common mode removal (circles green) vs. divide-oot (squares-light green) transmission spectrum for WASP-17b. Bottom: residuals of the common-mode transmission spectrum minus the divide-oot transmission spectrum. The uncertainties on the residuals is the residual scatter measured on the full spectroscopic lightcurve residuals.

3.3.1 Divide-oot with WASP-17

The divide-oot method originally developed by Berta et al. (2012) was discussed in § 2.5.2 as one of the techniques currently used to reduce WFC3 G141 transit observations. The divide-oot method relies on the cancellation of common-mode systematic errors by operating only on the data themselves using simple linear procedures, relying on trends to be similar in the time domain. As a number of our datasets do not conform to this condition we choose not to apply this to all datasets. Instead we show the impact of this common-mode method on the data using WASP-17 as an example observation.

Divide-oot is applied separately to each individual spectroscopic lightcurve using the two out-of-transit orbits to create a weighted mean template, which is then used to remove common orbit-to-orbit ramp-like systematics in each lightcurve. This method, however, does not account for visit-long trends across the lightcurve, or wavelength dependent shifts on the detector which are time independent. When constructing transmission spectra using divide-oot, as with the white light residual common-mode removal technique, it is necessary to additionally de-trend for the other systematics present (Huitson et al. 2013; Mandell et al. 2013; Ranjan et al. 2014).

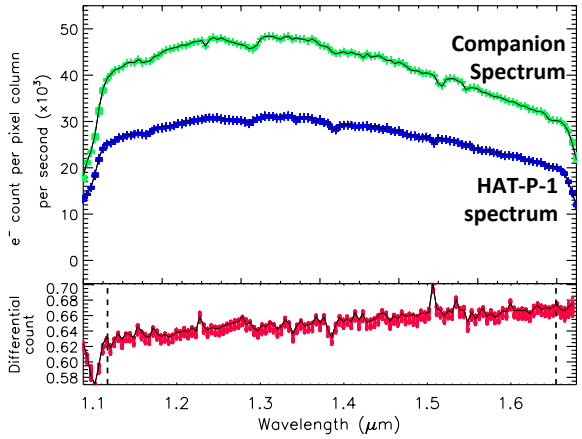

Figure 3.3.2: Top: spectra extracted from HST/WFC3 *ima* images for HAT-P-1 (blue-lower) and its G0 binary companion (green-upper). Bottom: the resultant spectrum from differential photometric analysis; the vertical dashed lines define the wavelength range used in the spectroscopic analysis.

We apply the same systematic model to both the spectroscopic lightcurves treated with the white lightcurve raw residual common-mode removal (common-mode) and those run through the divide-oot routine. Figure 3.3.1 shows the normalised transmission spectrum computed from both techniques. To determine the significance of the differences observed in the two reduction techniques we compute the difference between the absolute radius measured from both transmission spectra by subtracting the divide-oot transmission spectrum from the common-mode transmission spectrum. We determine the uncertainty by subtracting the spectroscopic lightcurves in the same way to obtain the residuals, and present the scatter observed as the uncertainty on the radius ratio residuals. This shows that the differences in the two methods for this particular dataset are very small with the only visible difference that the common-mode method has smaller uncertainties in the radius ratio. We therefore conclude that this method is a powerful tool to remove the highly repeatable systematics observed in a number of WFC3 transit datasets. However, given the dependence on repeatability in HST phase, or exposure cadence, it is not possible to apply this to all datasets, and therefore big comparative studies cannot be carried out.

3.3.2 Differential spectrophotometry of HAT-P-1

HAT-P-1 is the dimmer member of a double G0/G0 star system, ADS 16402, separated by 11.2″ (Bakos et al. 2011). Both stars are clearly resolved in the 68″ x 68″ field of view of HST/WFC3's spatial-scan spectra and are easily extracted separately in the analysis (see Fig. 3.2.1 and 3.3.2). This provides the opportunity to perform differential photometry on HAT-P-1 using the companion's signal which can reduce

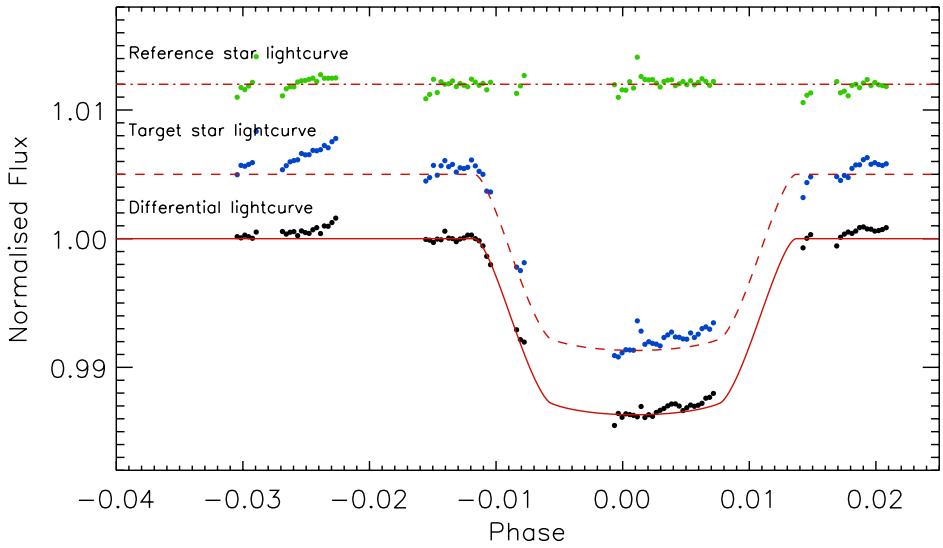

Figure 3.3.3: The raw white light curve for the reference and target star as well as the raw differential light curve produced by dividing the target star light curve by the reference star light curve. Over-plotted in red are the Mandel and Agol (2002) limb-darkened transit models. The different light curves have been artificially shifted for clarity.

observational systematics in the data (see Fig. 3.3.3). This analysis was performed using both spectral traces in an effort to evaluate the methods used in reduction to the shape of the resultant transmission spectrum.

We extract each of the stellar spectra using our custom *IDL* routine *spextract* optimising the aperture separately for each spectral trace. We find a common preferred aperture of ±23 pixels for each spectrum traced around the centring profile of each spectrum. Figure 3.3.2 shows all of the extracted spectra plotted on a common scale. From this it is clearer to see that the companion star is slightly brighter than HAT-P-1; however, it does not reach the saturation limit or non-linear regime of the detector.

Wavelength shifts

The G141 grism images contain both the zeroth order and the 1st order spectra for both stars. Each 1st order spectrum spans 128 pixels with a dispersion of 4.65 nm/pixel; the separation between the two stellar spectra was 23 pixels in the y-axis and 33 pixels in the x-axis. In addition to the wavelength analysis outlined in § 2.3.4

and § 3.1.1, we use the zeroth order spectrum to define the shift in wavelength across the entire observation period for both spectral traces. We measured a ±0.02-pixel column shift in the wavelength direction over the whole observing period, common to both stellar spectra. This corresponded to 186 Å or a ∼10% wavelength shift for each spectral bin over the span of the observations. We therefore adjusted the wavelength solution to use the average wavelength of the visit for each spectral bin. The observations, however, were relatively insensitive to sub-pixel wavelength shifts, as the H_2O spectral absorption band spans a much larger wavelength range.

Limb-darkening

For this analysis we calculated limb-darkening coefficients from a 3D time-dependent hydrodynamical model (Hayek et al. 2012), instead of the four parameter non-linear limb-darkening law used in the previous analysis, as the stellar spectrum is similar to that of HD 209458 which has been modelled extensively. The limb-darkening coefficients are calculated over the wavelength range 1.1–1.7 µm with the coefficients calculated separately for each spectral band. The 3D model shows overall weaker limb-darkening compared to the 1D model (Hayek et al. 2012). The 3D model takes into account convective motions in the stellar atmosphere resulting in a shallower vertical temperature profile. As the strength of limb-darkening is closely related to the vertical atmospheric temperature gradient near the optical surface, the limb darkening slightly weakens for the shallower temperature profile. We find that this leads to an overall common shift in the derived planet-to-star radius ratio, with the shape of the transmission spectrum unaffected.

Differential White Lightcurve

To compute the white lightcurve for each stellar spectrum we sum up the flux across the entire wavelength regime for each spectral exposure. The differential white lightcurve is computed by dividing the the target star flux by the reference star flux, which is shown to reduce the residual scatter by a factor of three (see Fig. 3.3.3 and 3.3.4). There are, however, still noticeable systematics in the resultant lightcurve that are not accounted for by the differential photometric reduction alone. These systematics were attributed to the "HST breathing" effect and fit with a high order polynomial in HST phase, as determined by the BIC following the parametrisation methods discussed in § 2.5.3. We note a significant reduction, up to 65%, in the

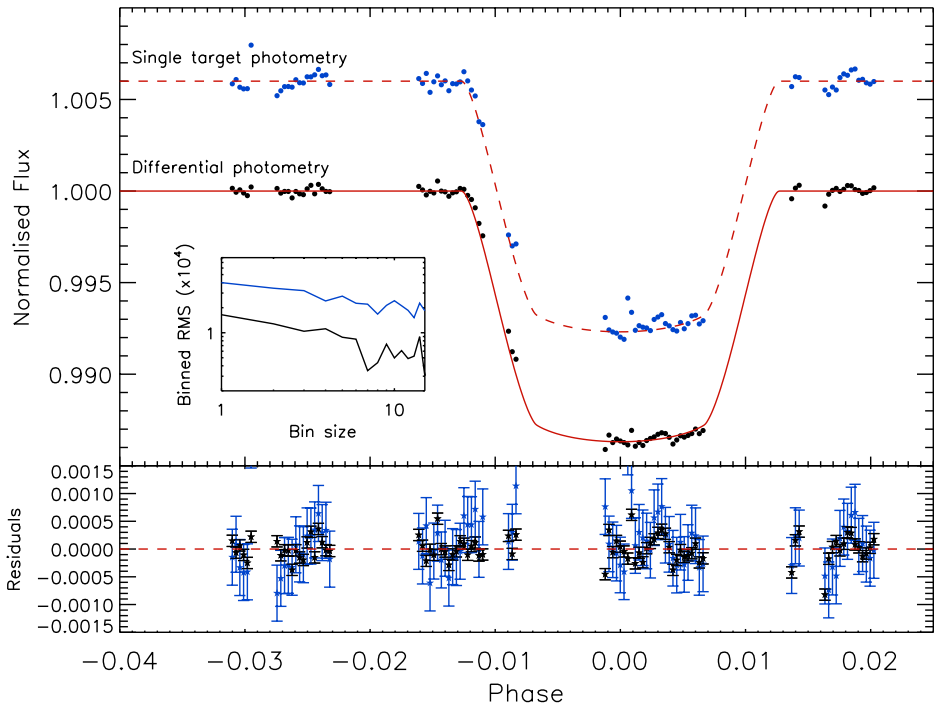

Figure 3.3.4: Upper: breathing-corrected light curves for both single target photometry (top curve) and differential photometry (bottom curve). The subplot shows the red noise for both single target (blue) and differential photometry (black) showing that time correlated noise is decreased when differential photometry is performed. Lower: Corresponding residuals for both fits showing the decrease in errors and deviation from the mean when applying differential photometry to the data.

parameters computed for the "HST breathing" effect between single target and differential photometry showing that the ability to perform differential photometry is an important aspect of this analysis. We find a decrease in the white lightcurve residuals from a standard deviation of 400ppm to 160ppm, placing a meaningful number on the reference star as a calibrator (see Fig. 3.3.4). Telescope systematic errors affect the science and calibrator stars in the same way to a precision of one part in 2400; we address the residual systematics, 3.2 times larger than the photon noise in the case of these observations, using individual parameter analysis.

MCMC analysis

To corroborate the results obtained using *MPFIT*, which implements a Levenberg-Marquardt least-squares minimisation algorithm (L-M), we also applied a Markov-chain Monte-Carlo (MCMC) data analysis (Eastman et al. 2013). While the L-M computes the best fit χ^2 value of the parameters by estimating the parameter errors from the covariance matrix calculated using numerical derivatives, the MCMC computes the maximum likelihood of the parameter fit given a prior value and evaluates the posterior probability distribution for each parameter of the model. The MCMC routine uses a simplified quadratic limb-darkening model described by parameters allowed to vary within the Kurucz grid of stellar spectra as a function of emergent angle. EXOFAST (a fast exoplanetary fitting suite in IDL) also uses the stellar mass-radius relation of Torres et al. (2008) to constrain the stellar parameters, compared to fixed non-linear limb-darkening parameters used in the L-M with unconstrained stellar parameters. MCMC can be more robust against finding local minima when searching the parameter space, where the L-M may get trapped. Each method produces similar results within the errors with the main small differences arising primarily from the different limb-darkening fitting procedures. The best fit lightcurve produced a final white light radius ratio of $R_P/R_* = 0.11709 \pm 0.00038$ (see Fig. 3.3.4), which is significantly different from that obtained using our single target method outlined in § 3.2.1. This, however, did not vary between our *MPFIT* and MCMC analyses.

Transmission spectrum

We construct multi-wavelength spectroscopic light curves by binning the extracted spectra into 28 channels with $\Delta\lambda = 192$ Å from 1.12µm to 1.65 µm, which is close to the resolution of the G141 grism. Similar to the previous analysis we remove the first orbit of exposures which exhibit varied systematics compared to the subsequent orbits.

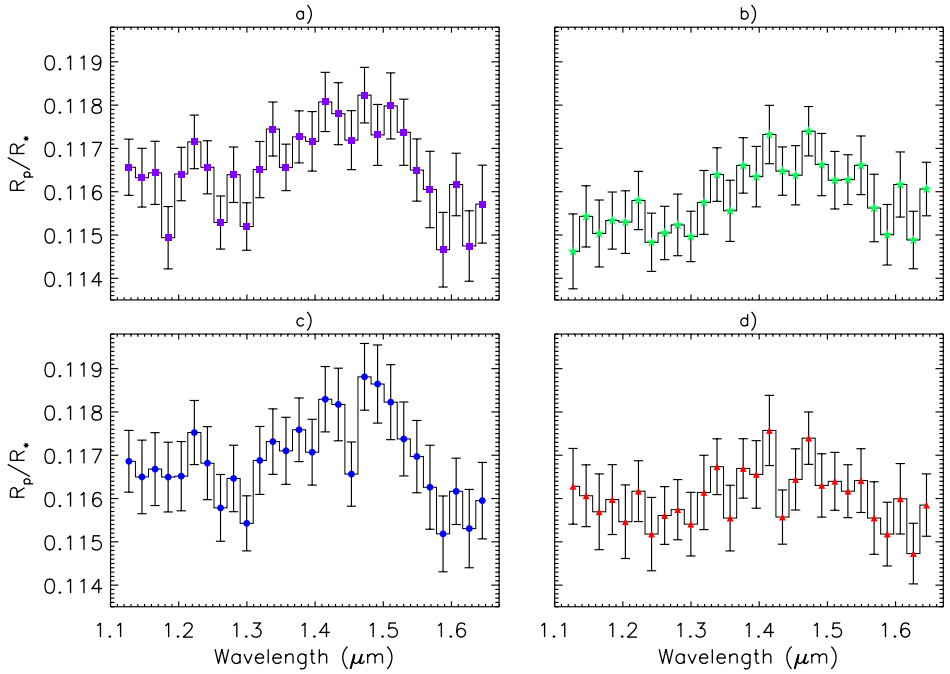

Figure 3.3.5: a) Transmission spectrum of HAT-P-1b for differential photometry individual parameter fitting. b) Single target photometry individual parameter fitting. c) Differential photometry with common mode fitting. d) Single target photometry with common mode fitting. While each spectrum shows a common spectral shape the method used for figure a) has lower red noise and residual scatter for each spectroscopic bin and is therefore adopted for further analysis.

We conduct individual parameter fitting on each spectroscopic differential lightcurve to measure R_p/R_* in each of the 28 channels. For each lightcurve fit we allow the baseline flux and systematic model parameters to vary for a high order polynomial in HST phase, with the orbital inclination, orbital period, a/R_*, and centre of transit time fixed to the values listed in Table 3.2.1. For limb-darkening coefficients we again used the 3D models, fixed for each spectroscopic bin.

We calculated the transmission spectrum using four different methods, testing the effects of individual parameter fitting and the cancellation of common-mode systematics using simple linear procedures, for both differential and single-target photometry. The four different methods displayed in Fig. 3.3.5 show a common structure to the transmission spectrum, indicating the significance of the spectral feature despite the assorted analysis techniques including differential analysis and common mode removal of the systematic trends. The mean scatter of the residuals for all of the spectral bins is reduced by 10% from single to differential photometry. In addition a reduction of

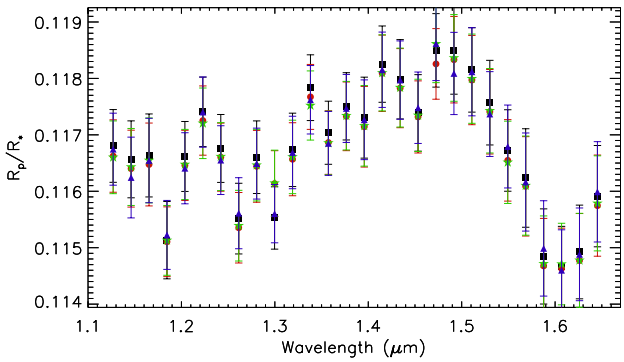

Figure 3.3.6: HAT-P-1b transmission spectrum computed for differential photometry with individual parameter analysis for four different systematic models. 7th order polynomial in HST orbital phase (black squares), 6th order polynomial in HST orbital phase (red circles), 5th order polynomial in HST orbital phase (green stars), 4th order polynomial in HST orbital phase (blue triangles).

$\sim$20% is seen between common-mode removal and individual parameter analysis.

We compute the transmission spectrum for differential photometry over a number of systematic models from a 4th order polynomial in HST orbital phase to the 7th order polynomial in HST orbital phase adopted for this analysis (see Fig. 3.3.6). Figure 3.3.6 shows that systematic models fitting for HST orbital phase with a polynomial of the orders between 4th and 7th do not change the overall transmission spectrum, while the BIC analysis favours a 7th order polynomial fit to the differential data, compared to a 4th order polynomial fit to the single target spectrum.

Finally, to further characterise systematic effects in the data that may not have been accounted for we injected a transit of constant depth ($R_p/R_*=0.1142$) into the reference star's light curve and computed the transmission spectrum over the same wavelength range with the same bin size. To compute the transmission spectrum, high-order HST orbital phase corrections were applied and no common-mode systematic removal was conducted. The resultant transmission spectrum shows the wavelength variation in the flux of the reference star using the same exposures used to measure the planetary transit, and can be directly compared to the transmission spectrum of HAT-P-1b computed using single target photometry and individual parameter analysis (i.e. with 7th order HST orbital phase correction and no common-mode systematic removal; see Fig. 3.3.7).

As expected, the computed reference star 'transit spectrum' is flat, with no water feature observed at 1.4 µm. This further demonstrates the reliability of the derived transit spectrum over the whole G141 spectral range.

Figure 3.3.7: Plotted in red stars is a transmission spectrum for the reference star computed after injecting a transit of constant depth (represented by the dashed red line) into the light curve. The black squares show the transmission spectrum of HAT-P-1b using single target photometry and individual parameter systematic fitting. The 'transit spectrum' of the reference star is rather flat, and does not show the water absorption spectral shape.

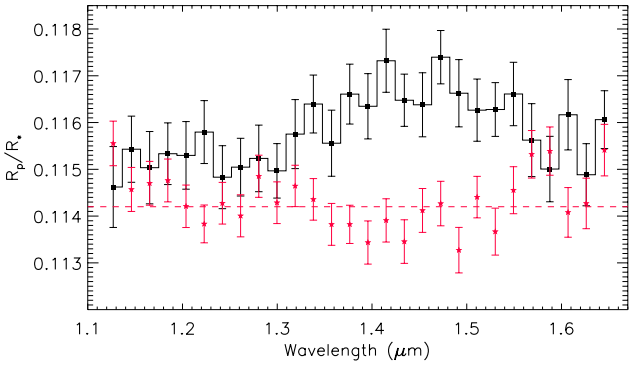

3.3.3 Implications on observed transmission features

The ability to use a simultaneously observed, common spectral type, companion spectrum is very rare in exoplanet transmission observations. This makes large comparative analysis with other planetary transmission spectra difficult. This analysis shows that systematics in the detector, while common between exposed regions of the detector, as seen by the improved precision of differential spectrophotometry, are still dependent on the specific spectral exposure. Deming et al. (2013) suggest a different technique to effectively produce differential spectra from single target observations. They produced a template stellar spectrum of the target star, given the expected response of the detector, and divided through each of the observed spectra by the template. This, like our differential spectrophotometry, still leaves additional systematics that continue to impact the white and spectroscopic lightcurves.

The differential transmission spectrum results presented here (Wakeford et al. 2013) and by Deming et al. (2013) reiterate the need for a new method similar to the one outlined in Chapter 2 and applied earlier in this chapter, as the systematic model needed to correct the present systematics still needs to be determined. The robust nature of the transmission spectral shape as shown in Fig. 3.3.5 and in Fig. 3.2.7 means that the emphasis needs to be placed on methods that not only effectively reduce the data, but ones that can be applied successfully to multiple datasets simultaneously for a true comparative study. The reduction method outlined in this thesis is the first universal analysis technique being applied to WFC3 data which is able to take into account a range of differences in the observed datasets.

3.4 Absorption features

The identification of atmospheric species is one of the first steps for understanding the nature of exoplanetary atmospheres. The presence of key species, or the lack thereof, provides information on the exoplanet composition, chemistry, temperature, and atmospheric structures such as clouds or hazes, thus helping us place exoplanets into subcategories.

Over the observed wavelength range sampled by the WFC3 G141 grism, the strongest atmospheric feature expected is the water absorption band with a characteristic bandhead at 1.4 µm. In most lower atmosphere models of hot Jupiters H_2O is well-mixed throughout the atmosphere, and most of the features between 0.7 and 2.5 µm come from the H_2O vibration-rotation bands (Brown 2001). These features are difficult to measure with ground-based telescopes due to confusion with water vapour signatures from the Earth's atmosphere. Space-based observations are therefore essential to probe such spectral regions in exoplanetary atmospheric studies.

3.4.1 Model fitting

Once we have determined the R_p/R_* value of our exoplanetary atmosphere from each spectroscopic lightcurve and produced a transmission spectrum, we can apply theoretical atmospheric models to determine the significance of any features observed and place constraints on the planet's atmospheric parameters, such as global temperature at the limb.

For each of our computed transmission spectra we select a suite of isothermal models calculated from a grid formulated by Fortney et al. (2010) to fit the data. These models include a self-consistent treatment of radiative transfer and thermochemical equilibrium of neutral and ionic species. Each of the isothermal models assumed a solar metallicity and local thermo-chemical equilibrium, accounting for condensation and thermal ionisation, though without photochemistry (Lodders 1999; Lodders & Fegley 2002; Lodders 2002; Visscher et al. 2006; Lodders & Fegley 2006; Lodders 2010; Freedman et al. 2008). In addition to these isothermal models we also, where possible, used planetary specific transmission spectra models calculated from 1D profiles for both dayside- and planetary-averaged cases from Fortney et al. (2010) and specific dayside- and planetary-averaged T–P profiles calculated using the 1D equilibrium code Atmo described in Amundsen et al. (2014) and Tremblin et al. (2015, submitted) which assumes radiative-convective and chemical equilibrium.

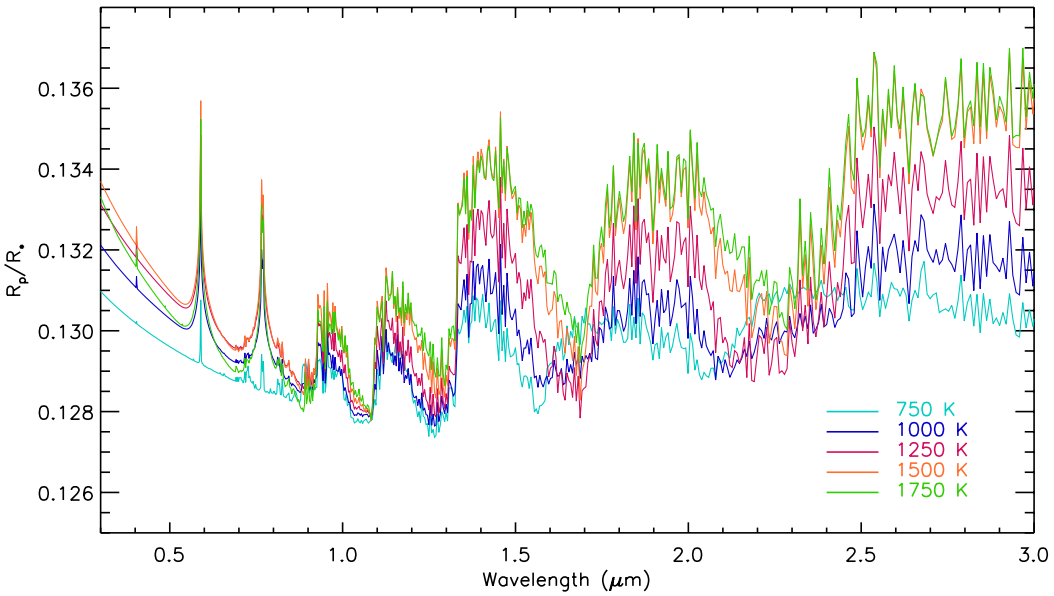

Figure 3.4.1: A series of hot Jupiter atmospheric transmission spectra from a grid of isothermal models computed by Fortney et al. (2010) with a g = 25 and 10× Rayleigh slope.

Figure 3.4.1 show the suite of isothermal Fortney et al. (2010) models we applied to each of our transmission spectra, where each of the displayed atmospheric transmission spectra is calculated with $g = 25\,ms^{-2}$ and contain an enhanced Rayleigh slope from the UV strtching into the optical. This addition of enhanced Rayleigh scattering does not affect the H_2O feature predicted at 1.4 µm in the transmission spectrum, where models with a greater Rayleigh slope begin to encompass the wavelength band covered by WFC3.

Each of the isothermal models are scaled to the target planetary atmosphere, assuming a specific gravity and equilibrium temperature, to compute the scale height (H). Due to the common-mode removal technique used here to correct for wavelength-independent systematics across the whole spectrum, the overall level of the transmission spectrum is not considered absolute. To account for this we add an additional fit to the transmission spectrum to shift it in altitude, matching that of the computed white lightcurve depth. The scaled model is then fit to the transmission spectrum using *MPFIT* where the model altitude is the only free parameter. We fit each transmission spectrum with a series of isothermal atmospheric models with temperatures of 750, 1000, 1250, 1500, and 1750 K excluding unlikely models based on the specific T–P profiles for each planetary atmosphere.

3.4.2 Comparison

For this comparative analysis we have divided our five planetary atmospheres into two categories: 'clear', defined here by the presence of an unobscured H_2O feature (Fig. 3.4.2), and 'cloudy', where no or severely muted H_2O absorption is measured (Fig. 3.4.3). While we expect H_2O to be well mixed throughout the upper atmospheres of hot Jupiter exoplanets, the strong absorption features in the near-IR can be obscured by high altitude clouds and hazes. The nature of these clouds or hazes will define the structure of the transmission spectrum from the optical into the IR. Our 'cloudless' atmospheres are defined as not containing high altitude obscuring clouds or hazes at the pressure levels observed in transmission; however, low altitude clouds are likely present. For the 'cloudy' atmospheres we fit models with an additional opacity source cutting off the H_2O feature at several scale heights, completely obscuring the 1.15 µm absorption band, and severely muting the 1.4 µm feature centred in the WFC3 bandpass.

Figures 3.4.2 and 3.4.3 show the transmission spectrum computed from each planetary dataset with a binsize of 10 pixels and fit with a suite of isothermal and planetary specific models. The figures also display the corresponding T–P profiles of each model fit and the planetary specific profiles computed from 1D atmospheric models. The pre-calculated models were compared to the data in a χ^2 test, with the base planetary radius as the only free parameter to adjust the overall altitude normalisation of the model spectrum. As no interaction is made directly with the model parameters when making a comparison, such as fitting for the abundance of TiO/VO, H_2O, or T–P profile, the number of degrees of freedom for the χ^2 test does not change between models. This analysis aims to distinguish between a number of the different assumptions used in current models and to identify any expected spectral features, rather than to perform spectral retrieval.

Comparison of the observed atmospheric features to those produced by isothermal hydrostatic equilibrium abundance models helps provide an overall understanding of the observed features and any departures from the models. For each of our exoplanet transmission spectra we first determine the best-fitting isothermal temperature model compared to that of a flat line at the average R_p/R_*, which assumes a featureless atmosphere. This allows us to place a significance value on each of the features observed in the different planetary atmospheres and make a direct comparison between transmission spectra. Where available we also apply planetary-specific transmission

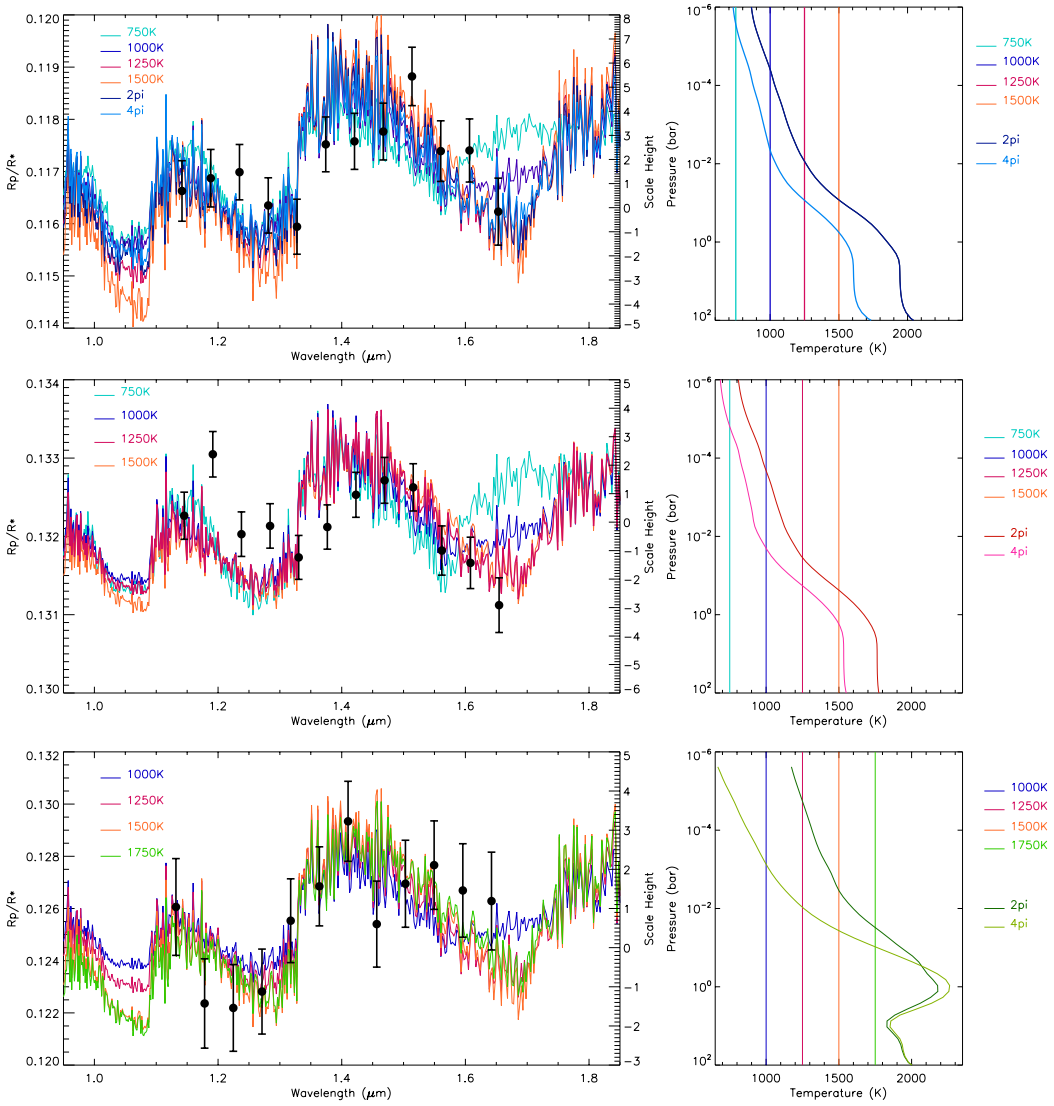

Figure 3.4.2: Top: HAT-P-1b transmission spectrum in binsizes of 10 pixels and fit with a suite of isothermal models and two planetary specific models, with the corresponding T–P profiles displayed in the right-hand plot. Middle: XO-1b transmission spectrum fit with a suite of isothermal models. The right-hand plot also shows the XO-1b specific T–P profiles for dayside-averaged (2pi) and planetary-averaged (4pi) (Fortney et al. 2010; private communication: N. Lewis). Bottom: WASP-17b transmission spectrum fit with a suite of isothermal models. The right-hand plot also shows the dayside- and planetary-averaged WASP-17b specific T–P profiles (Fortney et al. 2010; private communication: T. Kataria).

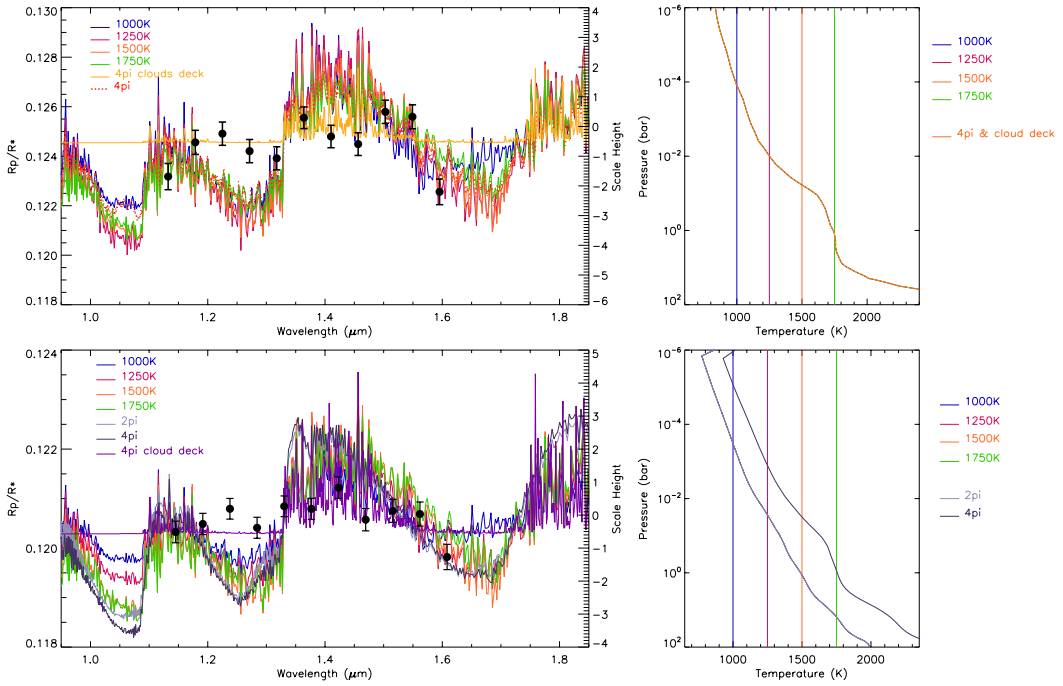

Figure 3.4.3: Top: WASP-31b transmission spectrum fit with a suite of isothermal models in addition to WASP-31b specific models, where a grey cloud-deck has been added obscuring a majority of the observed H_2O feature. The T–P profiles are shown in the right-hand plot (private communication: N. Lewis). Bottom: HD 209458b transmission spectrum fit with a suite of isothermal models (Fortney et al. 2010) and 1D atmospheric models for the dayside and planetary averaged transmission spectra (Amundsen et al. 2014; Tremblin et al. 2015, submitted; private communication: D. Amundsen). We additionally fit the spectrum with a cloud deck model applying a grey cloud-deck which obscures a majority of the H_2O features. The right-side plot shows the T–P profile for all of the models fit with the measured transmission spectrum.

spectral models to the measured transmission spectrum and again compute the χ^2 significance over that of a flat featureless atmosphere (see Table 3.4.1).

To determine the significance of each absorption feature observed in the five transmission spectra we also scale each model by a percentage of the full amplitude feature. While this is not a realistic simulation of muted features that would be observed in an atmosphere, it allows us to make quantitative comparison between each planetary atmosphere as a scaling parameter. In Table 3.4.1 we list each of the planets observed and the χ^2 fit for each model tested against the observed transmission. We then quote the χ^2 for models rescaled in amplitude with the most favoured percentage amplitude and its uncertainty.

Using the best-fitting model, as determined from the minimum χ^2 from models where only the altitude was allowed to vary, we plot the full amplitude feature and the best fit scaled feature in Fig. 3.4.4 (see bold columns in Table 3.4.1). This shows the true diversity of atmospheres being observed and the apparent dichotomy of 'clear' versus 'cloudy' atmospheres being observed across the wavelength ranges. Interestingly, the dayside-average T–P profiles for each of the planetary atmospheres converge at temperatures $\sim$1000$\pm$300 K at the pressures expected to be probed by transmission at the limb of the planet. However, the cooler planetary-averaged T–P profiles show a divergence to cooler temperatures, with the T–P profile of WASP-17b indicating very poor heat redistribution from the permanent dayside.

3.5 Results Summary

In this chapter we present the re-analysis of five hot Jupiter transmission spectra in the near-IR between 1.1–1.7 µm. This study has implemented a new analysis technique to reduce WFC3 near-IR spectroscopic data from exoplanet transit events to obtain robust and comparable transmission spectra for a range of exoplanetary atmospheres. We divide each stellar spectral trace into 10 pixel sized bins in the wavelength direction to compute the individual transmission spectra for the specific exoplanetary atmosphere. We present the derived transmission spectra from both spatially scanned and stare mode data, and assess the effect of various reduction methods on the resultant transmission spectrum.

We confirm that the 'clear' atmospheres of WASP-17b and HAT-P-1b show broad H_2O absorption features centred at 1.4 µm with a $\Delta\chi^2$ greater than 11 and 4 respectively. We also determine the significance of a muted feature given the best fit

Table 3.4.1: Table of exoplanets observed using WFC3 G141 grism, and model fits to the data where specific T–P profiles for dayside-averaged (2pi) and planetary-averaged (4pi) are included with the isothermal models. Models at the full amplitude are shown along with rescaled models where the amplitude of the model was adjusted to fit the data and is also listed. The χ^2 value to a straight line is also shown. Best-fitting models for each planet are in bold.

	750 K	1000 K	1250 K	1500 K	1750 K	2pi	4pi	cloud-deck	line
HAT-P-1b									
χ^2 full	23.02	18.89	21.96	25.85		20.15	**17.89**		22.39
χ^2 rescaled	18.85	14.03	11.32	9.68		11.37	**12.65**		-
% rescaled	48(25)	57(18)	50(15)	47(13)		52(15)	**59(20)**		-
XO-1b									
χ^2 full	43.83	**38.99**	46.16	62.76					31.95
χ^2 rescaled	31.94	**29.41**	26.91	27.72					-
% rescaled	18(26)	**34(21)**	33(15)	25(12)					-
WASP-17b									
χ^2 full		10.21	10.82	10.17	**8.44**				19.99
χ^2 rescaled		9.74	10.58	9.22	**8.25**				-
% rescaled		127(39)	86(28)	77(23)	**88(25)**				-
WASP-31b									
χ^2 full		92.23	109.21	131.79	117.67		**87.46**	**41.54**	41.54
χ^2 rescaled		38.40	35.15	34.54	34.62		**35.12**	-	-
% rescaled		23(13)	22(8)	21(8)	22(8)		**25(10)**	-	-
HD 209458b									
χ^2 full		**56.42**	98.22	155.19	134.63	157.18	184.06	**19.31**	23.50
χ^2 rescaled		**18.00**	16.60	17.63	18.34	17.12	16.93	**15.14**	-
% rescaled		**27(11)**	22(8)	17(7)	17(7)	17(6)	16(6)	**58(20)**	-

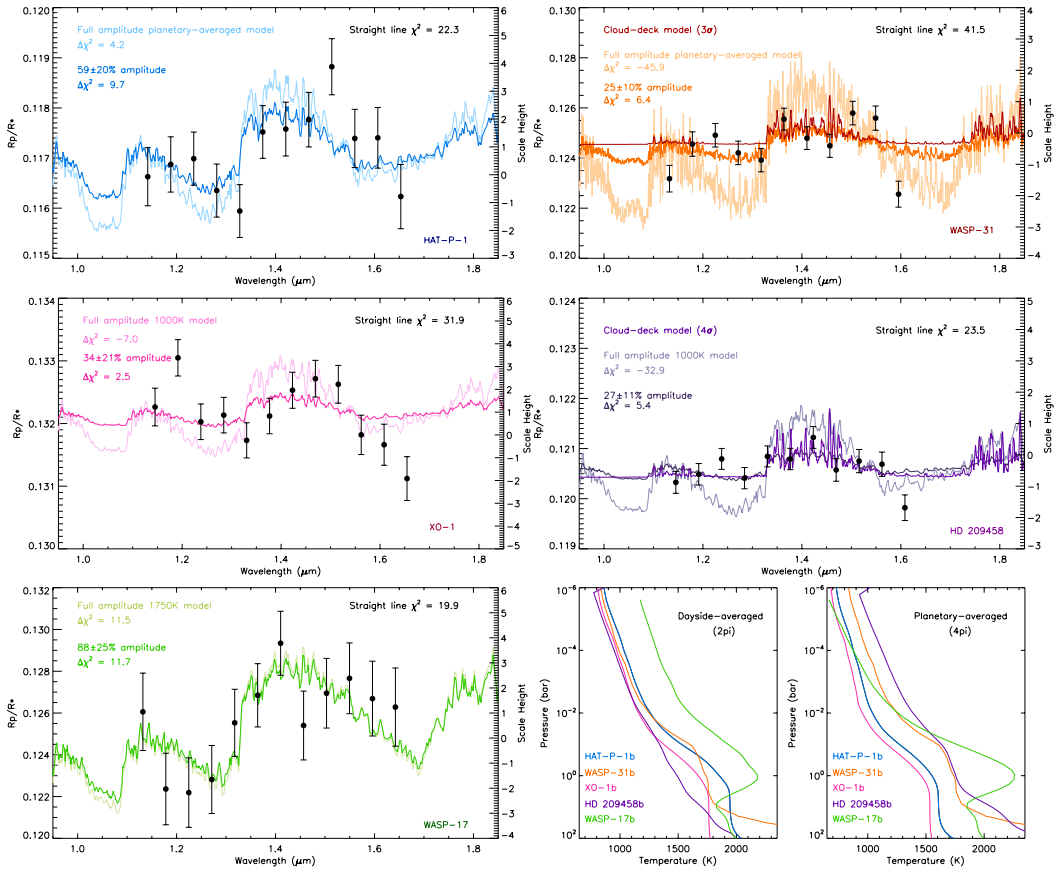

Figure 3.4.4: This shows the best fit model scaled to the full expected amplitude for each planetary atmosphere (light) and the amplitude scaled models (dark) for each of the transmission spectra measured in bins of 10 pixels for each planet. On each panel of the figure we list the $\Delta\chi^2$ fit compared to the χ^2 fit of a straight line at the average R_p/R_* which is listed in the top right corner of each panel. Each plot also states the most favoured percentage amplitude and the associated uncertainty. Bottom-right: the two panels show the planetary specific T–P profiles for the dayside-averaged (2pi) and pleantary-averaged (4pi) atmosphere (see the text for references).

amplitude of the modelled feature from the best fit models. We find an 88±25% feature favoured for the atmosphere of WASP-17b at 1750 K, and a 59±20% feature favoured in a planetary-averaged profile of HAT-P-1b increasing the significance of fit from ∼2 to 3.2σ.

We re-analyse the observations made of XO-1b and HD 209458b as the first spatially scanned transit datasets with WFC3 (Deming et al. 2013). We confirm the presence of a muted H_2O feature in the transmission spectrum of XO-1b with an atmospheric profile favouring a 1000 K model scaled to 34±21 % lowering the χ^2 by ∼10 when compared to a flat line representing a featureless atmosphere. Our analysis was not able to reproduce the transmission spectrum of HD 209458b obtained by Deming et al. (2013), instead finding a relatively flat featureless atmosphere best fit by a grey cloud-deck modelled as a strong opacity source at several scale heights in the atmosphere obscuring almost all expected H_2O features. In addition to our new analysis method, we need to incorporate the wavelength fitting technique outlined in Deming et al. (2013), which is most likely responsible for the differences in measured transmission spectra.

Finally, we confirm the implication of a strongly obscuring grey cloud-deck stretching into the near-IR in the atmosphere of WASP-31b (Sing et al. 2015), and find a best-fitting model atmosphere with a planetary-averaged profile at 25±10 % the amplitude of the full H_2O absorption feature. This also favours an atmosphere where the H_2O feature is not entirely obscured by the cloud, with a portion of the molecular vibro-rotational absorption signatures still present roughly one scale height above the unknown obscuring opacity source.

We hope to apply this analysis to a multitude of WFC3 near-IR transit observations and expand our study to make a true and robust comparison of exoplanet atmospheres as more and more favourable targets are observed. The impact of clouds on the transmission spectra is still a relatively new region of study. Continued optical and near-IR observational and theoretical studies are needed to explore the current dichotomy of atmospheres. The launch of James Webb Space Telescope in 2018 will extend the wavelength regime probed in transmission well into the IR.

There's just nothing new in the universe is there? It's the same everywhere, good cop, bad cop.

JOHN CHRITON
Farscape

4

Transmission spectral properties of condensate clouds

The work discussed in this chapter is part of a published paper in A&A, Wakeford & Sing (2015).

Where there is an atmosphere, there are clouds, or so the evidence suggests. Every planet in our solar system with a persistent atmosphere has clouds, though they are notoriously hard to define. Here we take the definition of liquid or solid aerosol particles suspended in a planet's atmosphere.

Clouds are a vital part of the energy balance of a planetary atmosphere, and they can potentially play a major role in the observed structure, blocking the atmosphere beneath them and weakening any emergent spectral lines. Jupiter's atmosphere is a prime example of how clouds can shape the atmosphere of a planet, forming coloured belts and zones of dark and light bands through vertical mixing of different species, which can represent differences in cloud depth of over one planetary scale height (Evans & Hubbard 1972). The clouds in the atmospheres of solar system planets are, however, hugely different from what we expect to form in the atmospheres of hot Jupiters (e.g. Sudarsky et al. 2003; Marley et al. 2007; Lodders 2010).

4.1 Hot Jupiter clouds

Hot Jupiters occupy a vastly different region of parameter space compared to the planets in our solar system, occupying higher temperatures, spanning wider temperature ranges, pressure structures, and chemical compositions. To compute the expected transmission spectrum for different cloud condensates requires us to understand a number of different processes in a planetary atmosphere. Studies have been conducted on the impact of clouds in exoplanet atmospheres (e.g. Ackerman & Marley 2001; Fortney 2005; Helling 2008; Howe & Burrows 2012; Marley et al. 2013; Morley et al. 2013) and the condensates that are expected in a wide range of temperatures from brown dwarfs to solar system bodies (e.g. Burrows & Sharp 1999; Khare et al. 2001; Lodders 2003; Cruikshank et al. 2005; Seager & Deming 2010; Morley et al. 2012).

The location and formation of cloud condensates is informed by the temperature-pressure (T-P) profile of the exoplanetary atmosphere. The altitude, and therefore pressure, at which a cloud deck will be observed is dependent on the condensation temperature as a function of pressure, where the condensation curve crosses the planetary T–P profile (see § 1.7). At and around the millibar pressure range it can be assumed, to the first order, that the temperature is constant with altitude at the limb of the planet when the absence of significant inversions is assumed (Fortney 2005).

Studies of dust species in the interstellar medium (ISM) have shown that while the precise composition cannot be determined from the absorption spectra alone (e.g. Li & Draine 2001, Li & Draine 2002; Draine 2003), it is possible to differentiate between different bond species from their stretching mode frequency, which generates strong broad absorption features at characteristic wavelengths. Similar detections of broadband absorption features have been made in brown dwarf atmospheric spectra (Cushing et al. 2006, Burgasser et al. 2008), where absorption features observed in the mid infrared are attributed to clouds of small silicate grains in the photosphere of cloudy L dwarfs. A majority of the absorption and emission features of dust species in the ISM and brown dwarfs can be found between 3 and 25µm. These features show strong correlation to wavelengths of major optically-active vibrational modes.

In this chapter we discuss the radiative properties of multiple cloud condensates expected for hot Jupiter atmospheres and compute the expected transmission spectra over a wide wavelength regime, including well into the infrared. Condensate absorption properties rely upon the index of refraction which we discuss in § 4.2.1 and later use to calculate the scattering and extinction cross-sections of each condensate. In

§ 4.2.2 we discuss Mie Theory and bond species vibrational modes in the context of potentially observable condensates. These are then combined to calculate the transmission spectrum in § 4.3 using the planetary scale height and condensate abundance with a look at the effect of different grainsize distributions. In the following chapter we apply the calculations to the well studied hot Jupiter HD 189733b to give reference to the resulting spectra.

4.2 Radiative properties of cloud condensates

Condensate chemistry in hot Jupiter atmospheres is dependent on the temperature-pressure profile and mass balance between refractory elements, such that the formation of condensate clouds at high temperatures severely depletes the gas at lower temperatures (Lodders 1999). The condensates considered in this study are compiled from a number of sources considering equilibrium and condensate chemistry in brown dwarf and exoplanet atmospheres (e.g. Lodders 1999; Lodders & Fegley Jr 2006; Helling 2008; Morley et al. 2012, Morley et al. 2013; see Table 4.2.1) with consideration for cooler atmospheres like those found in our solar system (e.g. Carlson et al. 1988; Baines et al. 1995; Lodders 2003; Bilger et al. 2013; see Table 4.2.2).

The condensates and cloud properties control the way that radiation moves through the planet's atmosphere, with the planetary transmission spectra dependent on the absorption and scattering of incoming and outgoing radiation. Mie theory is used to derive the absorption and scattering cross sections of solid and liquid particles (Hansen & Travis 1974), which can then be used to estimate transmission spectra. In this study, we do not attempt to derive a full self-consistent cloud model, but rather use simple analytic formulae and the expectations of current cloud modelling to help interpret hot Jupiter spectra.

4.2.1 Index of refraction

In order to calculate all radiative properties of cloud condensates, knowledge of their refractive properties is needed. The experimental values of the refractive index need to be known so that accurate absorption cross sections can be calculated. Table 4.2.1 shows a list of cloud condensates and where the refractive indices for this work were obtained. The index of refraction is defined as $N = n + ik$, where n and ik are the real and complex parts of the refractive index, respectively. The index of refraction

Table 4.2.1: Table of references for n and k index for a number of condensates expected to form clouds in the upper atmosphere of hot Jupiters.

Condensate	Reference n, k index	λ Range (µm)	Condensation Temperature^{+} (K)	Molecular Weight
SiO_2	Palik (1998)	0.04 - 11	1725	60.08
	Andersen et al. (2006)	7 - 28	-	-
	M. Meinecke (2005)*	6.6 - 10000	-	-
Al_2O_3	Koike et al. (1995)	0.3 - 150	1677[1]	101.96
FeO	Begemann et al. (1995)	10 - 100	1650[4]	71.79
	Andersen et al. (2006)	15 - 40	-	-
$CaTiO_3$	Posch et al. (2003)	2 - 155	1582[1]	135.94
Fe_2O_3	M. Meinecke (2005)*	0.1 - 987	1566	159.68
Fe_2SiO_4	Day (1981)	8.2 - 35	1443[4]	203.77
$MgAl_2O_4$	M. Meinecke (2005)*	1.6 - 270	1397[1]	142.26
$FeSiO_3$	Day (1981)	8.2 - 35	1366[4]	131.92
Mg_2SiO_4 (Fe–rich)	Henning et al. (2005)	0.2 - 445	1354[1]	140.63
Mg_2SiO_4 (Fe–poor)	Zeidler et al. (2011)	0.19 - 800	1354[1]	140.63
$MgSiO_3$	Egan & Hilgeman (1975)	0.1 - 0.4	1316[1]	100.33
	Dorschner et al. (1995)	0.5 - 80	-	-
Na_2S	Morley et al. (2012)	0.03 - 73	1176	78.04
MnS	Huffman & Wild (1967)	0.1 - 3	1139[2]	87.00
TiO_2	Kangarloo (2010a)	0.3 - 1.2	1125[2]	79.86
	Kangarloo (2010b)	1.3 - 30	-	-
NaCl	Palik (1998)	0.04 - 1000	825[3]	58.44
KCl	Palik (1998)	0.02 - 200	740[3]	74.55
ZnS	Querry (1987)	0.2 - 167	700[5]	97.45
CH_4	Martonchik & Orton (1994)	0.02 - 72	∼80	16.04
C_6H_{12}	Anderson (2000)	2.0 - 25	68	84.1
Titan Tholins	Khare et al. (1984)	0.01 - 0.2	≤90	∼50.0
	-	1.1 - 1000	-	-
	Ramirez et al. (2002)	0.2 - 1	-	-

* http://www.astro.uni-jena.de/Laboratory/OCDB/oxsul.html; $^{+}$ at 10^{-3} bar
[1] Lodders (2003), [2] Grossman (1972), [3]Burrows & Sharp (1999), [4]Ebel & Grossman (2000)
[5] Morley et al. (2012)

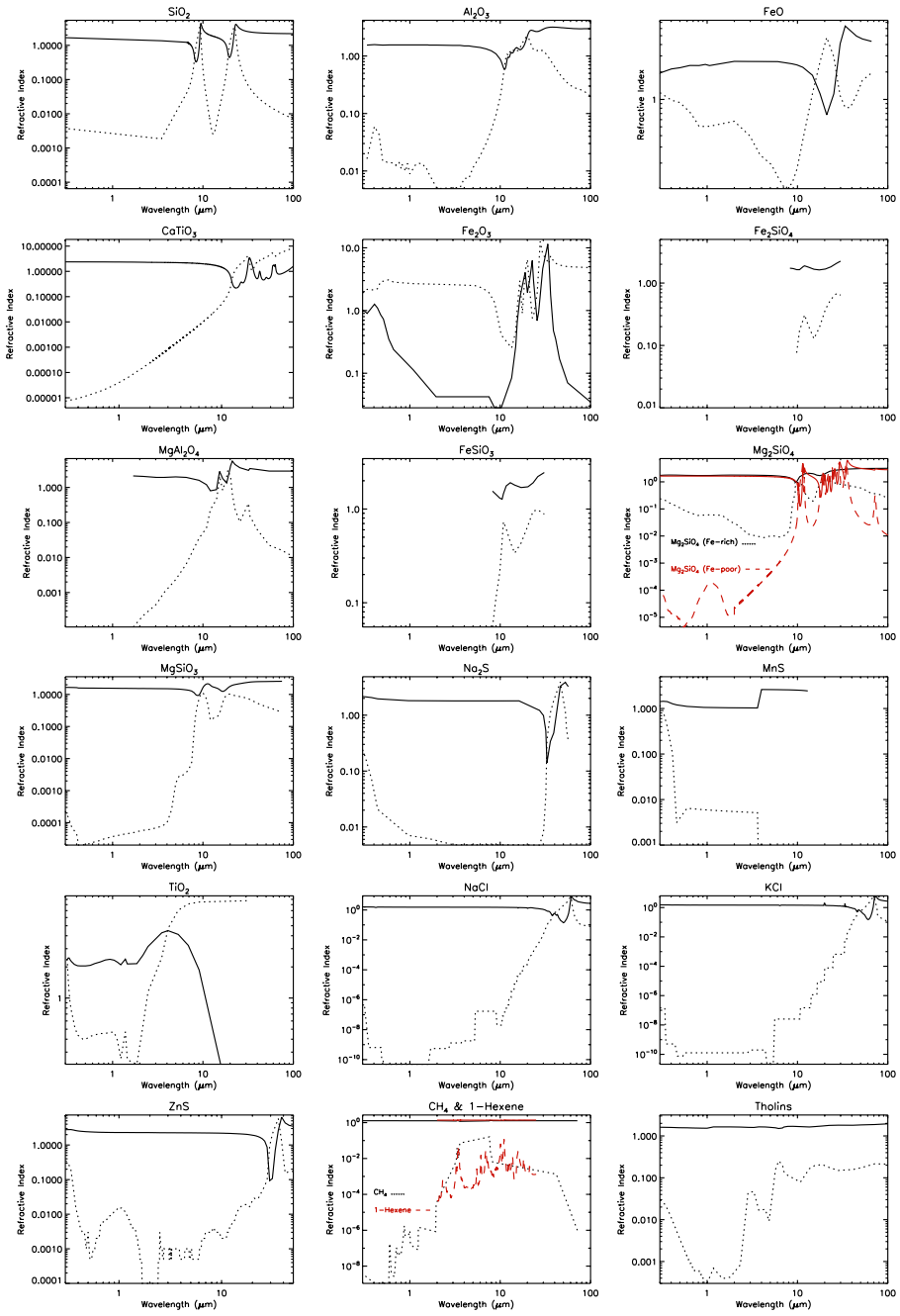

Figure 4.2.1: Real (solid) and complex (dotted) index of refraction for each of the condensates listed in Table 4.2.1. Condensates are listed in terms of their condensation temperature from hot in the top left corner to cold in the bottom right corner.

Table 4.2.2: Table of cloud condensates found in the atmosphere of solar system planets.

Condensate	Planet	Condensation Temperature$^+$ (K)	Pressure Range$^+$ (cold-hot) (bar)
H_2O	J, S, U, N	274 - 348	4.85 - 526
NH_3	J, S, U, N	147 - 163	0.66 - 7.62
NH_4SH	J, S, U, N	209-237	2.01 - 42
H_2S	S, U, N	116 - 124	0.66 - 3.23
CH_4	U, N	$\sim$80	0.94 - 1.2
Titan tholins	Titan	$\leq$90	

$^+$Carlson et al. (1988)

informs the scattering and absorption of electromagnetic waves through a material, while the complex index of refraction acts as a damping factor and is used to describe the attenuation of the waves (Liou 2002).

Figure 4.2.1 shows the real and complex index of refraction for each of the condensates in Table 4.2.1. The wavelength coverage of each condensate is determined by the experimental data presented in the associated papers. The calculated spectra are also dependent on the resolution of the measurements recorded. Features in the absorption properties of each condensate will have strong implications on the resulting spectrum of that particle. By referring to the complex index of refraction, trends emerge between different species of condensates, which can be explained by the vibrational properties of each molecule (see § 4.3.2).

4.2.2 Mie theory

Mie theory is an analytical solution to Maxwell's equations, which describes how to calculate the phase functions and absorption and scattering cross sections of solid or liquid particles. To compute these we use *bhmie*[1], an IDL routine that uses Bohren-Huffman Mie scattering to calculate scattering and absorption by a homogeneous isotropic sphere (Bohren & Huffman 1983). When the radius of the particle greatly exceeds the wavelength, the theory tends to geometric optics, while if the wavelength greatly exceeds the radius of the particle Mie theory tends to Rayleigh scattering as observed in a number of exoplanetary atmospheres in the UV and optical (Lecavelier des Etangs et al. 2008; Sing et al. 2011b). Mie theory is used to derive solutions for

[1]http://www.met.tamu.edu/class/atmo689-lc/bhmie.pro

spherical particles and is able to provide a first-order description of optical effects in non-spherical particles like those likely to exist in planetary atmospheres.

4.2.3 Scattering and extinction efficiency

Given the index of refraction, we can calculate the extinction, scattering, and absorption cross-section (σ_{abs}) and efficiency for a given particle size, where the scattering efficiency (Q_{scatt}) and extinction efficiency (Q_{ext}) are

$$Q_{scatt} = \frac{\sigma_{scatt}}{\pi a^2} = \frac{2}{x^2}\sum_{n=1}^{\infty}(2n+1)[|a_n|^2 + |b_n|^2]\,, \text{and} \tag{4.1}$$

$$Q_{ext} = \frac{\sigma_{ext}}{\pi a^2} = \frac{2}{x^2}\sum_{n=1}^{\infty}(2n+1)R_e(a_n + b_n)\,, \tag{4.2}$$

with the extinction and scattering cross-sections, σ_{ext} and σ_{scatt}, respectively, a is the grain radius, x is the size parameter ($x = 2\pi a/\lambda$), and a_n and b_n are the Mie coefficients expressed in terms of the complex index of refraction and Bessel functions (see Sharp & Burrows 2007 for full equations). From this the extinction, scattering, and absorption cross section can be calculated as

$$\sigma_{ext} = \sigma_{scatt} + \sigma_{abs}\ . \tag{4.3}$$

4.3 Transmission spectrum

To compute the transmission spectrum for a given condensate we calculate the effective altitude, $z(\lambda)$, of the atmosphere as a function of wavelength using the analytical formula of Lecavelier des Etangs et al. (2008) and the cross sections estimated from Mie scattering. This needs to be done separately for each of the condensates considered as it relies upon the planetary scale height and specific abundance for each cloud considered. Here we use the well-studied hot Jupiter HD 189733b as an example atmosphere with $R_p = 1.138\,R_J$, $R_* = 0.756\,R_\odot$, $g_p = 3.34\,ms^{-2}$, and $T_{eff} = 1350\,K$ (Southworth 2010; Torres et al. 2008). The effective altitude is given by

$$z(\lambda) = H\,ln\left(\frac{\xi_{abs}P_{(z=0)}\sigma_{ext}(\lambda)}{\tau_{eq}} \times \sqrt{\frac{2\pi R_p}{k_B T \mu g}}\right)\,, \tag{4.4}$$

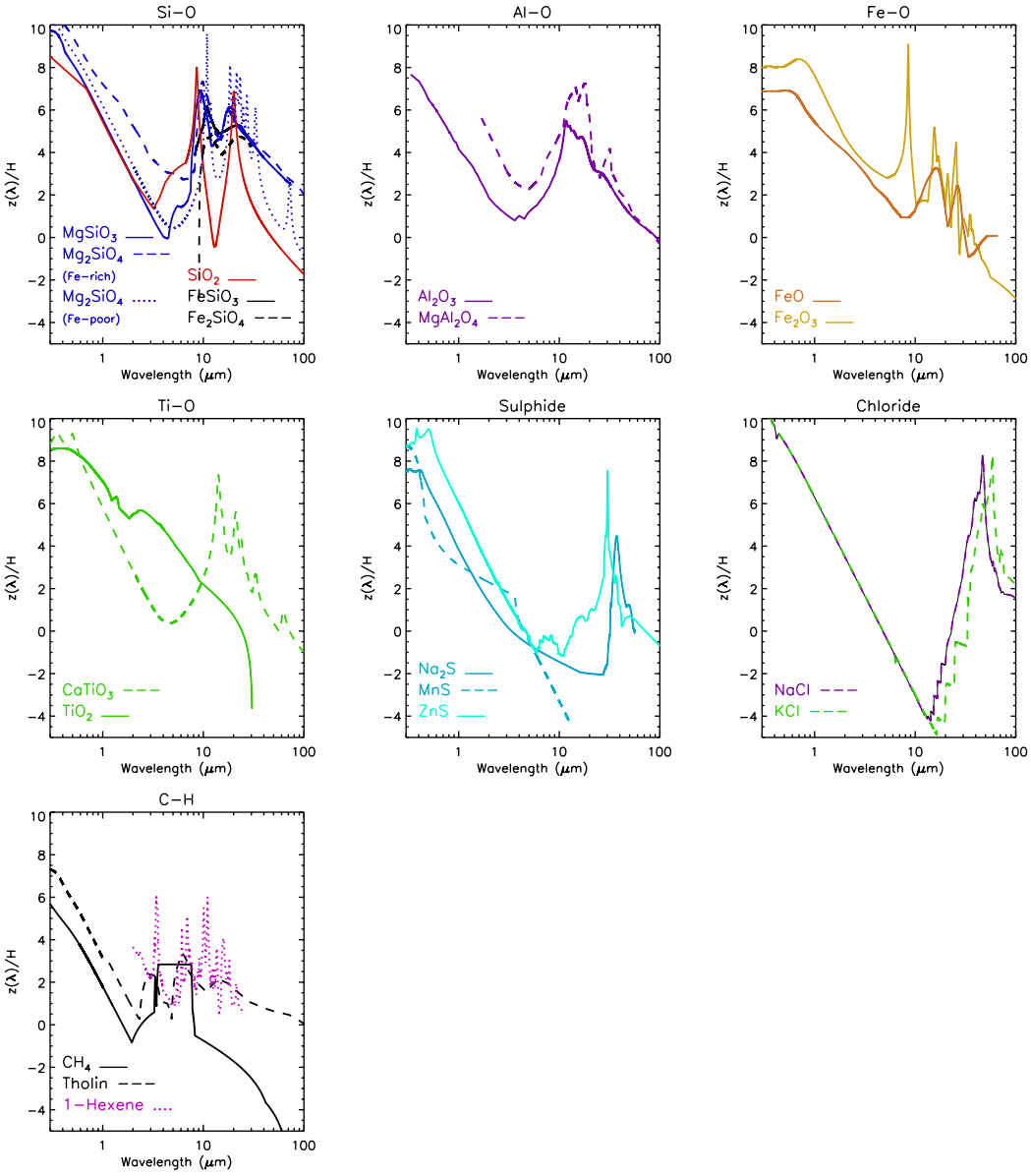

Figure 4.3.1: Transmission spectra for a number of condensates expected in hot Jupiter atmospheres using HD 189733b system parameters (a = 0.1μm, T_{eff}=1350 K). The condensates have been separated out according to their primary bond where vibrational modes between these species dominate the spectra.

where H is the planetary scale height, ξ_{abs} is the abundance of the dominant species, $P_{z=0}$ is the reference pressure at $z = 0$, $\sigma_{ext}(\lambda)$ is the wavelength dependent extinction cross-section, τ_{eq} is the equivalent optical depth at the measured transit radius ($\sim$0.56; Lecavelier des Etangs et al. 2008), and k_B is the Boltzmann constant.

A planetary scale height, H, is the altitude range over which the atmosphere pressure decreases by a factor of e, such that

$$H = \frac{k_B T}{\mu_m m_H g}, \tag{4.5}$$

where T is the estimated atmospheric temperature, m_H is the mass of a hydrogen atom, μ_m is the mean molecular weight of the atmosphere, and g is the surface gravity. For condensates their scale height, H, can potentially be smaller than the gaseous scale height; $H \sim H_g/3$ (Fortney 2005). Lecavelier des Etangs et al. (2008) showed that, in the case of HD 189733b, the gaseous pressure scale height can be equated to that of the condensate scale height determined from the observed Rayleigh slope, which implies strong vertical mixing of condensates in the planetary atmosphere. We use the same assumption here. We compute the condensate cloud transmission spectra for an isothermal atmosphere. Following temperature-pressure profiles from Fig. 1 of Showman et al. (2008) and Fig. 5 of Fortney et al. (2010) it can be seen that at altitudes probed in slant geometry at the terminator, in the mbar pressure range, the transmission spectra are not overly sensitive to changes in temperature, where ΔT is of the order of 100 K (also see Howe & Burrows 2012).

4.3.1 Condensate abundance

To determine the expected abundance of a certain condensate we first assume that it relies upon the metalicity abundance of the main atom from solar abundances (Burrows & Sharp 1999). Here we use the example of $MgSiO_3$ to demonstrate the calculation (Lecavelier des Etangs et al. 2008),

$$\xi_{MgSiO_3} = \frac{3\ a^3\ N_A\ m_p\ \mu_{MgSiO_3}\ \xi_{Mg}}{2\ \pi\ \rho_{MgSiO_3}} \tag{4.6}$$

where ξ_{Mg} is the solar abundance of Mg, ρ_{MgSiO_3} is the density of $MgSiO_3$, and $N_A m_p$ is Avogadro's constant multiplied by the mass of a proton acting as a scaling factor. The effective altitude, $z(\lambda)$, is then added to the bulk planetary radius to compute the observable transmission spectrum, $R_p(\lambda)/R_*$, of the condensate.

Figure 4.3.1 shows the transmission spectrum for each cloud condensate in Table

Table 4.3.1: Table of vibrational modes for the major diatomic bond species in the different cloud condensates considered in this paper.

Major Bond	Reduced Mass, μ_M (g)	Vibrational Frequency, ν (cm^{-1})	Wavelength, λ (µm)
Si - O	10.192	1110 - 830[a]	9 - 12
Al - O	10.043	1100 - 350[c]	9 - 28.7
Fe - O	12.436	790[b]	12.5
Ti - O	11.99	850 - 150[d]	16 - 66
MnS	20.247	295-220[e]	20.2
ZnS	21.51	464[f]	21.5
NaCl	13.95	366[g]	13.95
KCl	18.60	281[g]	18.6
C - H	0.923	3032[a]	3.3

[a]Glassgold & Graham (2008); [b]Lehnert et al. (2002)
[c]Saniger (1995); [d]Gillet et al. (1993)
[e]Batsanov & Derbeneva (1969); [f]Kröger & Meyer (1954)
[g]Rice & Klemperer (2004)

4.2.1 computed for the atmosphere of HD 189733b given a condensate grain size of 0.1 µm and abundances 1x solar. We plot the spectrum in units of scale height, H, such that the transmission spectra of different exoplanets will appear very similar, as z/H is only weakly dependent upon specific values of R_p or g. The different condensates have been separated into groups of their primary diatomic bond to highlight the similarities between different condensate spectra when the absorption is dominated by one vibrational state.

4.3.2 Vibrational modes

Major dust spectral features are determined by vibrational modes. Silicate dust has a major feature at 10 µm, while hydrocarbons have major features at 3 µm. The vibrational frequency, ν, for the major dipole bonds considered here can be estimated assuming a harmonic oscillation with,

$$\nu = \frac{1}{2\pi c}\sqrt{\frac{K}{\mu_M}} \tag{4.7}$$

where c is the speed of light, K is the force constant of the bond considered, and μ_M is the reduced mass in grams $\mu_M = (m_1 m_2)/(m_1 + m_2)$.

The calculated vibrational modes and their corresponding wavelength ranges for each of the major bond species considered in this study can be seen in Table 4.3.1. Unlike gaseous molecules, where the rotational structure of the molecules can be observed as individual narrow absorption lines, solid molecules suppress the rotational structure as they cannot rotate freely resulting in a smearing of the absorption lines into broad peaks. Figure 4.3.1 displays the transmission spectra calculated using Mie theory, and the commonalities between different condensates with the same major vibrational modes due to the main diatomic bond can be seen.

For simple diatomic molecules like MnS and ZnS or NaCl and KCl the slight difference in vibrational modes can be seen clearly in the sharp absorption features of their transmission spectra. More complex molecules show broad absorption features across a range of wavelengths centred around the vibrational wavelength of the major dipole.

4.3.3 Particle size and distribution

The transmission spectrum for all condensate species is highly dependent on the size (a) of the particles composing the cloud. To loft particles to the upper atmosphere, the expectations of vertical mixing need to be taken into account. Models from Parmentier et al. (2013) and Heng & Demory (2013) show that strong vertical mixing can keep micron or sub-micron sized particles aloft in the atmosphere where grain sizes between 0.001 and 100 µm were considered. Lecavelier des Etangs et al. (2008) show that in the Rayleigh regime, the cross section is proportional to a^6. This makes the scattering and resulting transmission spectrum largely dependent on the largest grain size in the particle distribution of the cloud.

To demonstrate the effect of larger grain sizes in clouds with particle distributions, we applied a series of log-normal grain size distributions to our cloud particles and calculated the resulting transmission spectrum. Log-normal distributions, $lnN(\mu, \sigma)$, are dependent upon the centre, μ, of the distribution and the width, σ. We set a grid of log-normal distributions with $\mu = 0.001$ - 7.5 µm and $\sigma = 0.05$ - 1.0 and computed the cumulative transmission spectrum for the condensate clouds of each distribution. Figures 4.3.2, 4.3.3, and 4.3.4 show three distributions with the contributing grain sizes for the transmission spectra, and the resulting cumulative spectrum. These figures demonstrate the effect of larger grain sizes on the cumulative transmission

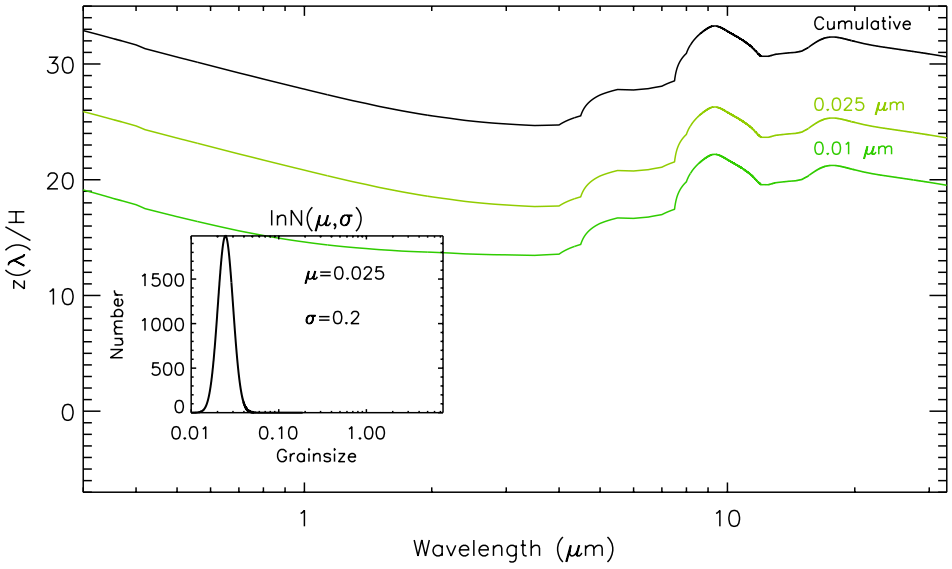

Figure 4.3.2: Cumulative transmission spectrum of a log-normal distribution centred at 0.025μm with a width of 0.2 showing each of the individual spectra contributing to the final transmission spectra of the cloud. Each of the spectra have been offset for clarity. The sub-plot shows the smoothed log-normal distribution used for this cloud with the x-axis on a log scale.

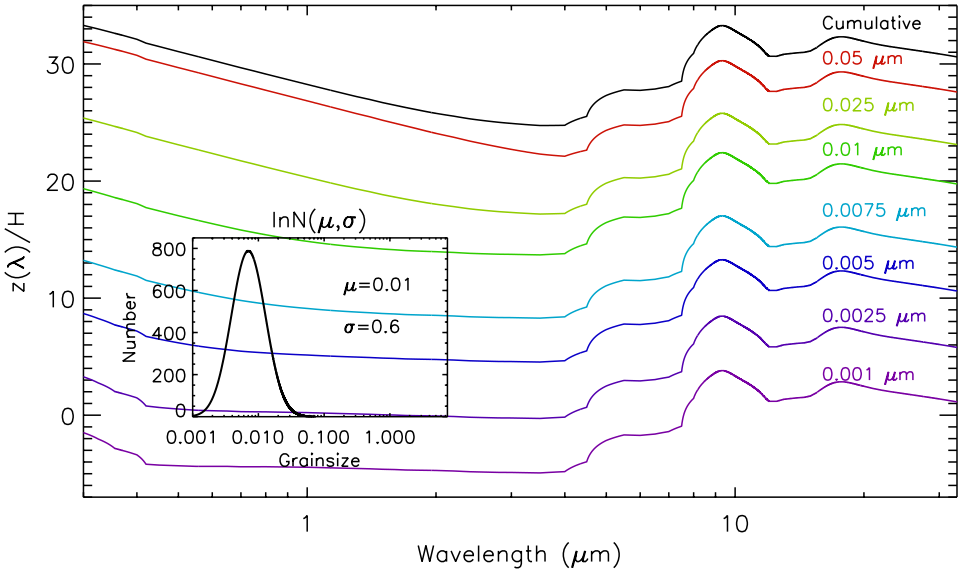

Figure 4.3.3: Cumulative transmission spectrum of a log-normal distribution centred at 0.01μm with a width of 0.6 showing each of the individual spectra contributing to the final transmission spectra of the cloud. Each of the spectra have been offset for clarity. The sub-plot shows the smoothed log-normal distribution used for this cloud with the x-axis on a log scale.

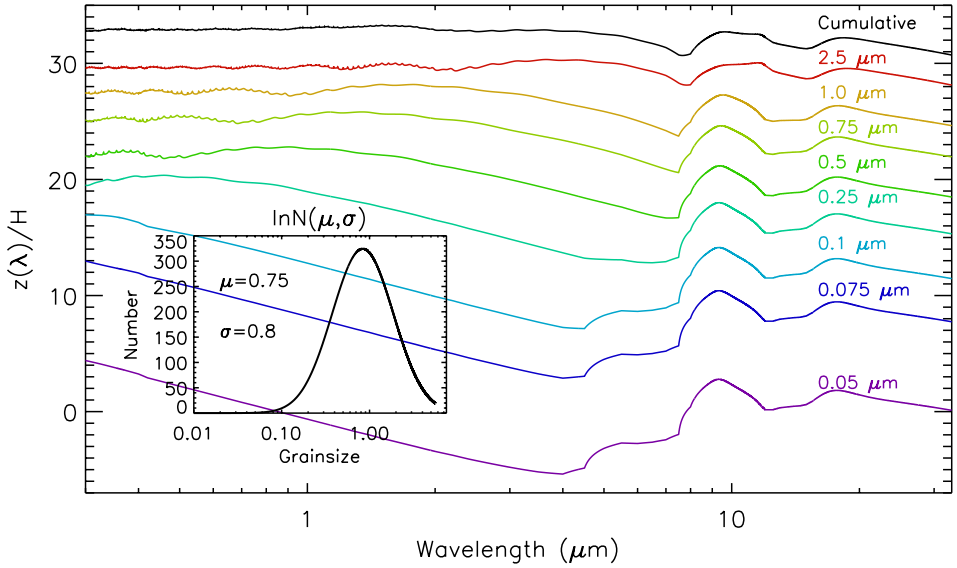

Figure 4.3.4: Cumulative transmission spectrum of a log-normal distribution centred at 0.75μm with a width of 0.8 showing each of the individual spectra contributing to the final transmission spectra of the cloud. Each of the spectra have been offset for clarity. The sub-plot shows the smoothed log-normal distribution used for this cloud with the x-axis on a log scale.

spectrum, where a small number of large grain size particles dominates the resulting cloud spectra. For distributions with only sub-micron sized particles, vibrational mode absorption features in the infrared can be seen. As evident in Figs. 4.3.2, 4.3.3, and 4.3.4 all the cumulative distribution transmission spectra can be well approximated by a single grain size which is the largest in the distribution, as expected given the $\sigma \propto a^6$ relation. Distributions with sizes larger than $\sim$1 µm tend toward completely flat, featureless spectra in the optical and infrared. Figure 4.3.4 shows the transition from prominent absorption features visible in sub-micron sized particle spectra to flat spectra where the grain sizes become larger than $\sim$1 µm.

4.4 Properties of condensate clouds

Key features in hot Jupiter transmission spectra can be used as diagnostic tools to set limits on the grain size of observed clouds, and predict the likelihood of features being observed at longer wavelengths. The presence of a Rayleigh slope in the optical part of the spectra, like that seen in HD 189733b (Pont et al. 2013), indicates that any clouds present in the atmosphere at transmission spectral altitudes are likely made of sub-micron sized grain particles. Further evidence of infrared features (McCullough

et al. 2014), along with the general planetary parameters, can be used to diagnose the probability of observing condensate absorption features in the mid infrared where a majority of the condensate vibrational modes are observed. However, if larger grain sizes are lofted up in the atmosphere to altitudes probed by transmission spectra it is unlikely significant optical to infrared features will be observed, such as in the flat transmission spectra of HAT-P-32b (Gibson et al. 2013).

In the following chapter we use the example of HD 189733b to predict the properties of clouds in its atmosphere and diagnose potential observations to be made with JWST.

The answers are there, you just have to know where to look for them.

AGENT DANA SCULLY
The X-Files

5

Application of modelled condensate cloud spectra

The Work discussed in this chapter is part of a published paper in A&A, Wakeford & Sing (2015).

A majority of current exoplanet spectra are constructed from ground-based measurements with additional low resolution spectra from HST at wavelengths short of 1.7 µm, and in the infrared from Spitzer (e.g. Gibson et al. 2013; Pont et al. 2013; Sing et al. 2013; Nascimbeni et al. 2013). At present, these observations focus on the UV, optical, and near-infrared regions of the spectrum, revealing information on the portion of transmission spectra for aerosols where only scattering features are seen (e.g. Pont et al. 2013; Sing et al. 2013; see Fig. 1.3.5). In the previous chapter we used Mie theory, and the expectations of current cloud modelling, to compute approximate hot Jupiter transmission spectra from the optical to far infrared regime. In this chapter we apply the calculated spectra to observations of the well studied hot Jupiter HD 189733b to interpret the likely cloud condensates to form in the atmosphere, the grainsize distribution, and predict potential condensate absorption features visible in the bandpasses covered by JWST.

When interpreting observations, the slope of spectra in the optical regime is proportional to the temperature of the atmosphere and can be indicative of specific species when small grain sizes are considered. Absorption features in the near- and mid-infrared spectra may then be identified, with the vibrational modes of the major bond pair in the condensates providing additional information on the composition.

Models of brown dwarf atmospheres suggest that silicates are likely to form the dominant cloud structures in hot Jupiter atmospheres where temperatures are greater than ∼1000 K, with sulphide clouds becoming dominant at temperatures below 900 K at which chlorides also begin to condense out (Morley et al. 2012). It is expected that hotter atmospheres could have a greater abundance of Al_2O_3 and Fe_2O_3, as silicates will not have condensed out. Additionally, Al_2O_3 and $CaTiO_3$ will not be present at the mbar pressure level in atmospheres with $T_{eff} \leq 1600$ K as Al and Ca get locked up in magnesium oxides in deeper layers of the atmosphere.

This work shows that while it is unlikely that we will be able to distinguish between individual silicate dust species, similar to the ISM and brown dwarfs, we may be able to discern a contrast between separate dust sub-classes like those shown in Fig. 4.3.1. As a result, an observational distinction can be placed on photochemically generated species, such as hydrocarbons with a dominant C–H bond, and condensation chemistry produced molecules like those with a dominant Si–O bond. Along with wavelength differentiation between major species' vibrational modes, there is also a significant altitude distinction in the transmission spectra where features in the near infrared can extend above the optical slope. At these wavelengths, predominant cloud absorption features could compete with H_2O and other molecules in the near infrared, potentially obscuring expected atmospheric features.

5.1 Interpreting hot Jupiter transmission spectra

Presently exoplanet spectra are limited to the optical and near-infrared regime below 1.7µm with intermittent wavelength coverage into the infrared with Spitzer. Current exoplanet broadband transmission spectra that have evidence for clouds show commonalities in the optical regime, where all scatterers appear to be very similar. There is growing evidence for differences in their molecular transmission spectral signatures. For instance, WFC3 spectra have detected large H_2O features in HAT-P-1b, WASP-19b, and WASP-17b (Wakeford et al. 2013; Huitson et al. 2013; see § 3.2.5), while these features can be muted or even absent for other planets like WASP-12b and WASP-31b (Sing et al. 2013; Sing et al. 2015).

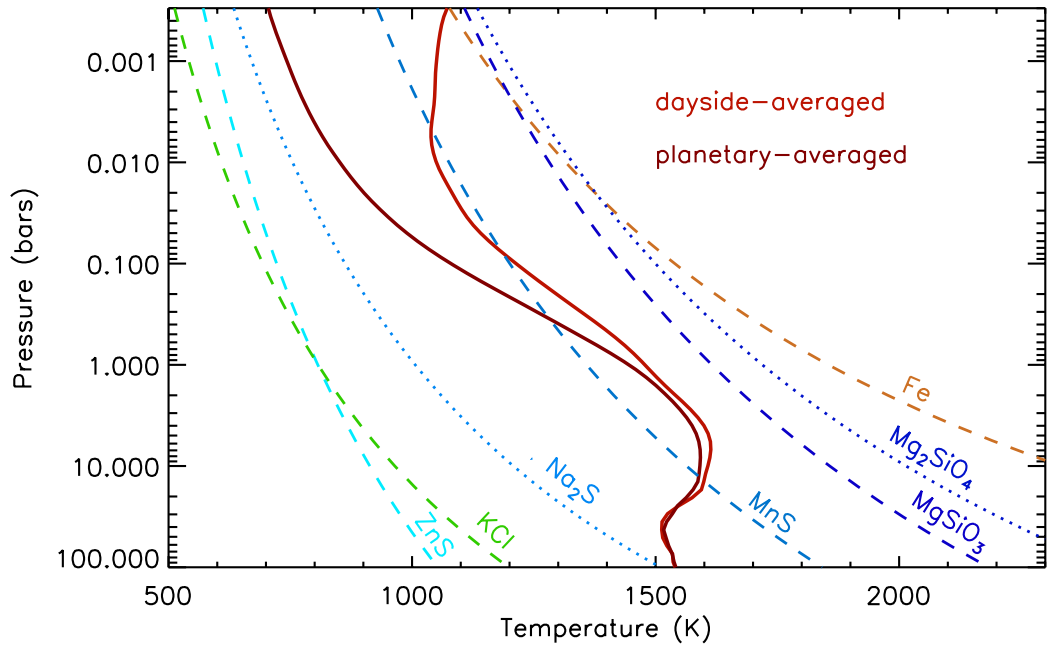

Figure 5.1.1: Condensation curves computed following the equations outlined in Visscher et al. (2010) and Morley et al. (2012) for a series of condensates expected to form clouds in exoplanet atmospheres. A dayside- and planetary-averaged T–P model profile of HD 189733b (Fortney et al. 2010) is over-plotted to show the condensate clouds expected to form at different pressures in the atmosphere.

The hot Jupiter HD 189733b has been extensively studied into the infrared with observations by cold Spitzer at 3.6, 4.5, 5.8, 8.0, and 24 µm (Knutson et al. 2007b, Knutson et al. 2012). Measurements of HD 189733b in the infrared hint at the presence of molecular absorption by water in the planet's upper atmosphere with additional evidence from both high resolution spectroscopy and eclipse spectral data (Grillmair et al. 2008; Birkby et al. 2013; Pont et al. 2013; McCullough et al. 2014). We use the HD 189733b transmission spectrum as an example hot Jupiter atmosphere, and discuss potential spectral features with regards to the condensates and photochemical species shown in this study.

Absorption from gaseous species such as H_2O, CO, and CH_4 can be present in the infrared and obscure condensate features. For HD 189733b, optical scattering can be seen to high altitudes spanning ∼7 H with infrared data giving strong constraints on the altitude levels of the gaseous molecular species such as H_2O. Given the T–P profile for the atmosphere of HD 189733b computed using 1D profiles for both dayside- and planetary-averaged cases following Fortney et al. (2010), we plot the condensation

curves of various species, computed following the equations outlined in Visscher et al. (2010) and Morley et al. (2012) (see Fig. 5.1.1). This shows the different cloud species expected to form in the atmosphere where the condensation curve of the chosen species cross the planet's atmospheric T–P profile. It can also be seen that due to temperature differences across the two hemispheres of the planet, different clouds would be expected to impact the observed spectra at different altitudes. In this case the planetary averaged T–P profile likely represents the limb of the planetary atmosphere probed through transmission, while the condensate species indicated by the dayside-average T–P profile will likely highly impact the planet's emission spectra and albedo.

While only a subset of the condensates considered here are appropriate for HD 189733b, given the planetary parameters, we use it to illustrate where other condensates could be detectable in hotter or cooler exoplanets, given their vibrational modes. Using HD 189733b as an example exoplanet transmission spectrum we address two questions; *what transmission spectral features for the various condensates can we observe?* and *at what wavelength are we likely to observe them?*

5.1.1 Grainsize

We fit the HD 189733b transmission spectrum with a grid of log-normal distributions applied to the condensate $MgSiO_3$. We fit the cumulative spectrum of each grid point with the complete HD 189733b spectrum by allowing only the altitude to vary applying no stretching parameter to the scattering slope in the optical. Figure 5.1.2 shows the $\Delta\chi^2$ fit for each log-normal particle distribution, where the position of the expanded distributions in Fig. 4.3.2, 4.3.3, and 4.3.4 from the previous chapter are labelled A, B, and C respectively. The best fit distribution is shown to be 0.025 µm when σ is small, with wider distributions where the maximum grain size is 0.025µm also providing good fits to the data.

Using the $\Delta\chi^2$ distribution grid we can rule out the presence of particles of $MgSiO_3$ larger than ∼0.025 µm in the atmosphere of HD 189733b, which would generate a 'flat' spectrum from the optical through the infrared and likely hide the deeper H_2O features observed in the near infrared. Expanding these results to other hot Jupiters and across different condensates, a similar exploration of the grain size distributions which are compatible with optical and near-infrared transmission spectra can be used to predict potential condensate vibrational mode features in the infrared. These findings suggest such infrared vibrational modes will only be observable in transmission spectra where

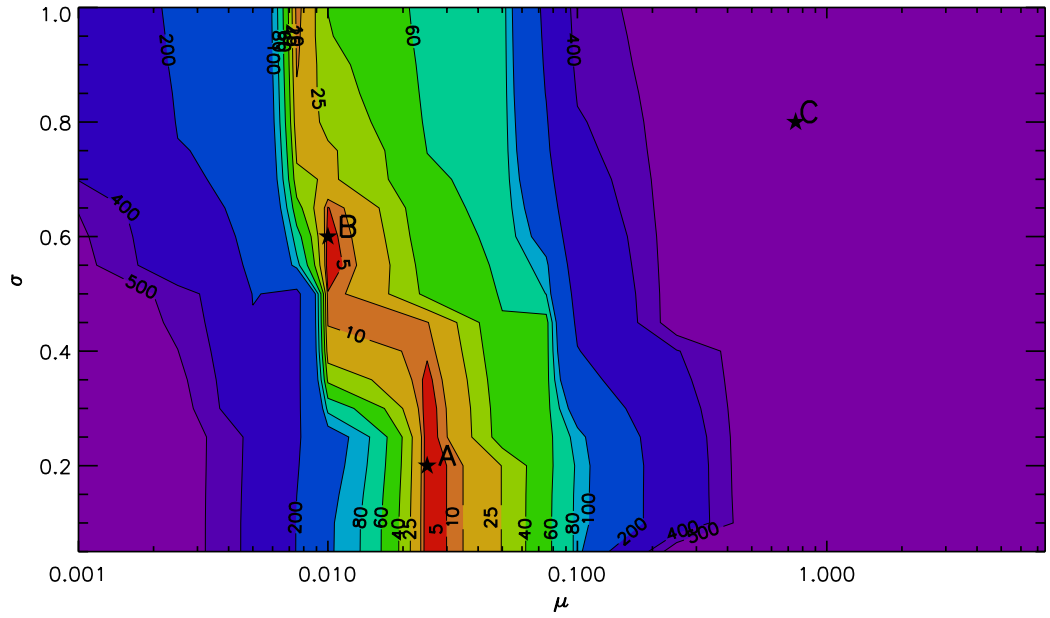

Figure 5.1.2: $\Delta\chi^2$ grid for a series of log-normal grainsize distributions when fitted to the HD 189733b transmission spectral data. The best fit occurs for distributions which contain ∼0.025 µm size particles. The distributions in figs 4.3.2, 4.3.3, and 4.3.4 are labeled A, B, and C respectively

optical scattering is present with sub-micron size particle distributions.

Given the largest grain-sized particle in the distribution produces a reasonable approximation of the transmission spectrum's shape, as shown by Figs. 4.3.2 – 5.1.2, for simplicity a single grain size is assumed in subsequent sections.

5.1.2 Condensate spectra

Figure 5.1.3 shows the observed HD 189733b transmission spectrum from 0.3 to 24 µm (Pont et al. 2013; McCullough et al. 2014) with a representative condensate spectrum for each of the major diatomic vibrational modes shown in Fig. 4.3.1. We fit single grain size condensate cloud spectra from 0.001 – 10 µm calculated using Mie theory for each of the condensates in Table 4.2.1 to the HD 189733b data from 0.3 – 1.0 µm of Pont et al. (2013) where significant Rayleigh scattering is observed. By allowing only the altitude to vary, we find a best-fit grain size of 0.025 µm for each of the condensates matching the grain size distribution fits shown in Fig. 5.1.2.

The cloud model spectra shown in Fig. 5.1.3 demonstrate that while scattering by aerosols becomes negligible at longer (∼2 µm) wavelengths, as the cross-section

becomes small, significant infrared absorption features appear. In some cases, these vibrational absorption features are seen to rise to altitudes in the transmission spectra above the optical scattering levels, making them potentially detectable. Additionally, a number of the absorption features span multiple scale heights becoming visible above the expected molecular bands of the abundant gaseous species (H_2O, CH_4). We use a Fortney et al. (2010) model of HD 189733b which has a 1000× enhanced scattering to estimate the amplitude and relative location of molecular features in the transmission spectrum, fitting for the HD 189733b transmission data (Pont et al. 2013; McCullough et al. 2014) by allowing only the model altitude to vary. The Fortney et al. (2010) model is a good fit to the optical slope, the 1.4 µm H_2O feature, and the Spitzer data, though only contains an artificial pure-Rayleigh scattering component, which has no effect on the transmission spectrum longer than ∼2 µm. As evident in Figs. 4.3.1 and 5.1.3, the scattering properties of each condensate considered here are expected to be similar short-ward of 3 µm, as absorption features, due to the vibrational modes of the molecules, are not observed in the optical and near infrared (see Table 4.3.1). Here we consider each of the major bond species in turn and discuss the absorption features which may be detectable for sub-micron size grains.

Si–O: Each of the silicates considered to be present in the atmospheres of hot Jupiters show a strong Rayleigh slope in the optical up to 3µm with an exception of Fe–rich Mg_2SiO_4 which shows additional absorption to that of standard Rayleigh. Major vibrational mode absorption features emerge from 9 – 12 µm spanning multiple scale heights matching the altitude at the top of the optical Rayleigh slope. In Fig. 5.1.3 these features are represented by the transmission spectrum of $MgSiO_3$ which has an absorption feature across several microns reaching above the 1000× Fortney spectra. If silicate clouds dominated by small particle sizes are present in hot Jupiter atmospheres, it is likely that their presence and pressure altitude can be determined by transmission spectral features observed in the infrared by JWST/MIRI.

Al–O: Aluminium oxides also show distinct Rayleigh properties in the optical, with broadband absorption features extending from 9 – 28 µm. While it is unlikely that the atmosphere of HD 189733b contains Al–O condensate clouds, it is possible that hotter Jupiters, such as WASP-12b which has a significant optical slope, can show Al–O condensate features. As evident in Fig. 5.1.3, the peak of the Al–O vibrational mode feature forms a broadband absorption spectrum between that of the two silicate absorption features at 10 – 12 µm. It is possible that if Si–O or Al–O condensate clouds are present in a hot Jupiter atmosphere, such as the high temperature condensates SiO_2 or Al_2O_3, either could be identified where the altitude of the obscuring feature

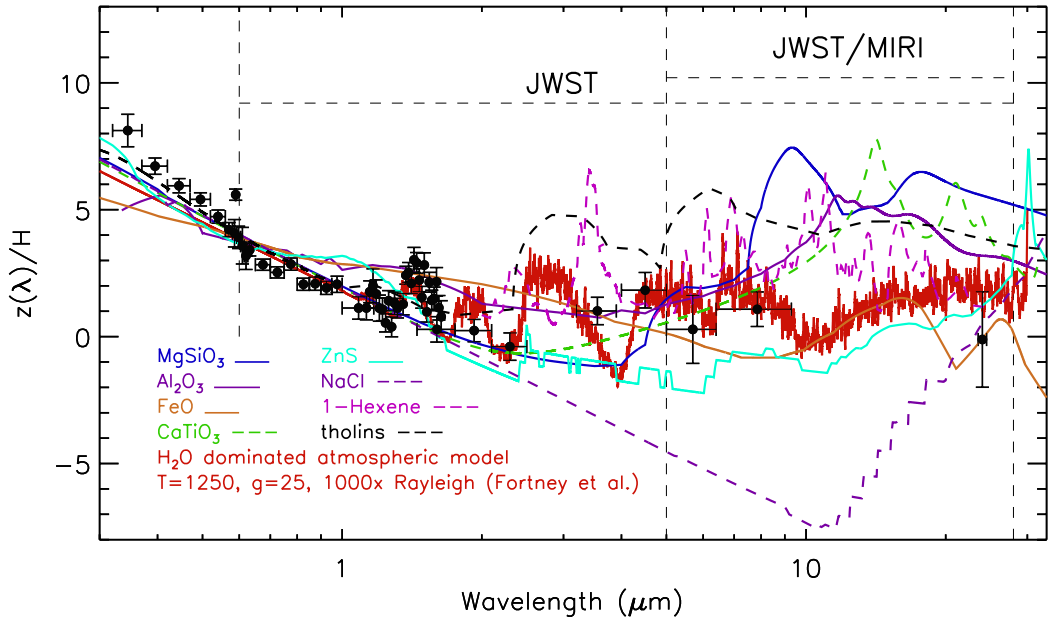

Figure 5.1.3: Transmission spectrum of HD 189733b (Pont et al. 2013; McCullough et al. 2014) compared to a number of different condensates with a best fit grainsize of 0.025μm and a H_2O dominated atmospheric model from Fortney et al.

can exceed that of potential gaseous molecules from ∼8 – 20 µm.

Fe–O: The major vibrational mode features of iron oxides are centred at ∼14 µm with both broad- and narrow-band features from ∼9 – 40 µm. For small grain sizes like that shown in Fig. 5.1.3 the transmission spectrum of Fe–O compounds exhibit a flattened slope from 0.3 – 2 µm which could obscure the expected molecular water bands at 1.1 and 1.4 µm. While potential iron-oxide narrow-band features, like those of Fe_2O_3, may be visible above the expected H_2O dominated transmission spectra (see Fig. 4.3.1), it is unlikely that broadband features will be observed at the mbar pressure level where spectra dominated by gaseous vibro-rotational bands are several scale heights above any potential absorption features.

Ti–O: Figure 5.1.3 shows the computed transmission spectrum of $CaTiO_3$, selected to represent potential Ti–O condensate clouds formed in hot Jupiter atmospheres. Ti–O molecules have vibrational mode features from 16 – 66 µm which is partially covered by JWST/MIRI. While the cooler TiO_2 condensate shows little to no distinct features (see Fig. 4.3.1), the hotter condensate $CaTiO_3$ has visible narrow absorption feature centred at ∼15 µm and ∼21 µm, which span several scale heights above the 1000× Fortney model.

Sulphides: Sulphur-bearing compounds are expected to condense in hot Jupiter

atmospheres at ∼1100 K with highly scattering properties short-ward of ∼10 µm. Similar to iron oxide condensates, the transmission spectra shows a levelling off between 0.5 and 1 µm which can potentially be used to help identify such clouds in UV and optical transmission spectra. In addition, the hotter condensates such as Al–O- and Fe–O-bearing compounds are not expected to coincide with sulphide condensate clouds, which helps identification. However, any additional features distinct to sulphur-bearing compounds do not emerge above the H_2O dominated model in hot Jupiter transmission spectra within the wavelength limits of JWST.

Chlorides: Alkali chlorides begin to condense at around 800 K, depleting the expected Na and K atomic species in the planets upper atmosphere. Figures 4.3.1 and 5.1.3 show that these condensates are highly scattering well into the infrared following a Rayleigh slope to ∼10 µm. Vibrational modes are unlikely to be observed in hot Jupiter transmission spectra due to the obscuring molecular features, similar to sulphur-bearing condensate species. However, there is potential for chloride clouds to be inferred in cooler exoplanetary atmospheres where strong Rayleigh scattering is observed in the optical and there is no evidence for atomic gaseous Na or K in the optical spectra, suggesting that the species may have condensed out of the atmosphere forming clouds of liquid or solid particles.

Spectral measurements well into the infrared with extended wavelength resolution have the potential to differentiate between condensate species for a wide range of exoplanetary atmospheres as most of the cloud species have their lowest opacities at these mid-infrared wavelength regions. The 24 µm point, of HD 189733b further aids in the interpretation of the planets atmosphere placing strong constraints on the particle size given the optical vs. infrared absorption level, also noted by Lee et al. (2014). While these vibrational modes of major bond species can be used to help identify the condensate cloud in the exoplanetary atmosphere, it is hard to ascertain the specific condensate responsible for the absorption feature present. Figure 5.1.3 shows cloud spectra extending above that of gaseous species, with a majority of potentially identifiable species having one or more absorption features in the wavelength range covered by JWST.

Identifying the different vibrational modes of potential cloud condensates and constraining / comparing the species in different exoplanet atmospheres could provide valuable insight into condensation chemistry over large temperature ranges. While the current broadband photometry is not of sufficient spectral resolution to distinguish between the models considered here, the situation should rapidly change with JWST.

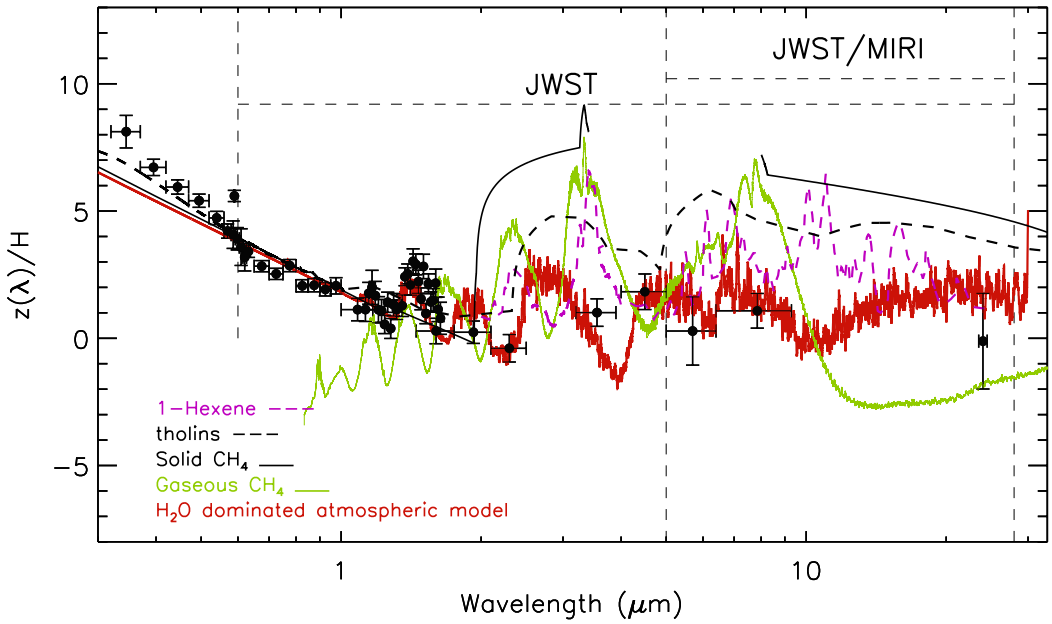

Figure 5.1.4: Transmission spectrum of HD 189733b (Pont et al. 2013; McCullough et al. 2014) compared to hydrocarbon condensates and gaseous CH_4 (Yurchenko & Tennyson 2014; Amundsen et al. 2014) and C_2H_4 (Rothman et al. 2009; Sharp & Burrows 2007)

5.1.3 Photochemical vs. condensation

Although unlikely to be present in the atmosphere of HD 189733b, we have also included clouds composed of hydrocarbon species, such as hexene and Titan tholins, which may be generated photochemically. It can be seen that, although a poor fit to the HD 189733b data, the major absorption features for condensate hydrocarbons extend above the 1000× Fortney model at the ∼3 µm wavelength of the C–H vibrational mode and thus may be potentially observed for other planets.

In cooler planetary atmospheres, photochemistry is expected to play a key role in the overall cloud composition in the generation of gaseous hydrocarbons. When the planetary C/O ratio is greater than 1, the abundance of carbon-bearing compounds increases significantly, with disequilibrium processes enhancing their abundance over that of other species (Moses et al. 2013b). Figure 5.1.4 shows the transmission spectrum of HD 189733b with the considered hydrocarbon species as well as the expected transmission spectrum for gaseous CH_4 at solar abundance. The opacities for gaseous CH_4 are calculated from the new ExoMol line list (Yurchenko & Tennyson 2014), with the line width parameters as in Amundsen et al. (2014). It can be seen that

the gaseous CH_4 transmission spectral features overlap considerably with that of the hydrocarbon condensate cloud spectra, specifically at the 3 µm range where the vibrational mode of the C–H bond is responsible for the absorption feature. There are, however, still some notable differences which may be used to differentiate between the two states with additional absorption features shown in both hexene (∼10 µm) and tholin (∼6 µm) condensate spectra which emerge several scale heights above both the H_2O dominated exoplanet spectra and that of the photochemically generated gaseous CH_4 (see Fig. 5.1.4).

5.2 James Webb Space Telescope

We have considered the different condensates that are expected to form condensate clouds in hot Jupiter exoplanet atmospheres with specific consideration to the wavelengths covered by James Webb Space Telescope (JWST). JWST, set to launch in October 2018, is a NASA mission, with significant contributions from both ESA and CSA. JWST is a 6.5 m near- to mid-infrared telescope that will orbit at the Sun-Earth L2 point giving it an uninterrupted view of the sky. JWST is equipped with low, medium, and high resolution spectrographs from the instruments NIRSPEC (0.6 – 5 µm) and MIRI (5 – 28 µm).

MIRI detectors are similar to Spitzer IRAC 5.8 and 8.0 µm with an expected noise floor less than 100 ppm. It is the only JWST instrument that will observe wavelengths greater than 5 µm. The medium resolution spectrometer (MRS) is composed of four channels from 5 – 28 µm with a resolution ∼3000–1000. To obtain a full transmission spectrum with MRS from 5–28 µm four separate transit observations are required to observe in all four channels equalling ∼24 hours of observations for a majority of known exoplanet targets.

Here we use HD 189733b as an example hot Jupiter to simulate the transmission spectrum of our cloud condensate models and interpret the results with respect to the estimated precision[1] and resolution of the instruments used. A systematic noise floor value of 50 ppm was adopted for the simulations following the framework outlined in Fortney et al. (2013) with additional photon noise estimated using the MRS throughput (Glasse et al. 2010). As discussed in Section 4.3.3, the presence of a strong optical slope in the transmission spectrum of HD 189733b makes it a primary candidate for condensate cloud detection in the wavelength regime covered by JWST. Figure 5.2.1

[1]These estimates can be improved upon with an officially released specific exposure time calculator and increased understanding of the instrument systematics.

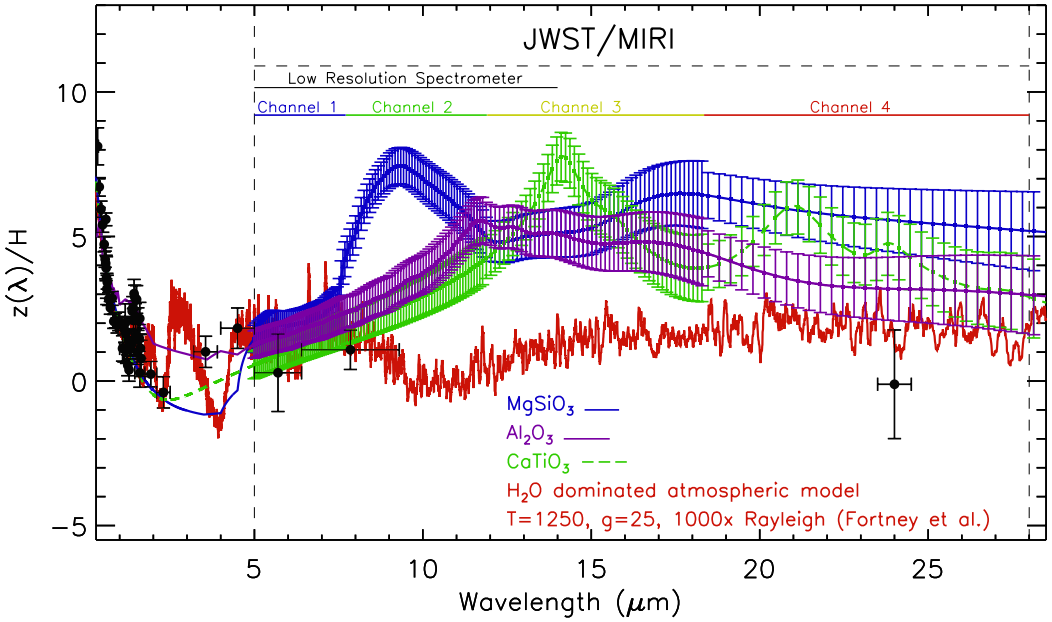

Figure 5.2.1: Transmission spectrum of HD 189733b (Pont et al. 2013; McCullough et al. 2014) over-plotted on cloud model spectra set to R∼50 for JWST/MIRI Medium resolution spectrograph channels 1–3 and R∼30 for channel 4 with the wavelength coverage highlighted above the different regions of the spectra they cover. We also highlight the region of the spectrum covered by the low resolution spectrometer (5 – 14 μm).

shows three of our cloud condensate models plotted to a resolution of R∼50 across channels 1 – 3 and R∼30 in channel 4. The spectra are binned significantly in each of the MIRI channels to increase the photon count at each wavelength therefore reducing the uncertainty of each wavelength bin.

MIRI is ideal to detect the condensate vibrational mode features given in Table 4.3.1 where most condensates have distinguishable features which can rise above the expected levels of the gaseous molecular features, with sulphide and chloride condensates a notable exception. Using the example condensates shown for the atmosphere of HD 189733b, transmission spectral observations using the two central channels (2 & 3) of MIRI/MRS could be vital in distinguishing clouds formed from different condensate species. Each of the Si–O-, Al–O- and Ti–O- bearing condensate compounds considered have absorption features extending several scale heights above that of the H_2O dominated molecular model which can be detected and resolved with MIRI. Channel 2 of the MRS effectively covers the vibrational mode peak of Si–O- bearing compounds with absorption features several scale heights above that of other conden-

sate species shown. Ti–O vibrational mode features are effectively covered by channel 3 of the detector. Al–O- bearing condensate distinction would require observations over multiple channels of MRS, such that species such as Si–O and Ti–O can be ruled out and the infrared absorption features also matched to the levels observed in the optical.

It is also possible to use the MIRI low resolution spectrometer (LRS) which covers $5-14\,\mu m$ with a R$\sim$100 (Fortney et al. 2013). LRS encompasses both the major Si–O vibrational absorption mode at $\sim 9\,\mu m$ and absorption features generated by photochemical species such as tholins at $\sim 6\,\mu m$. LRS is also advantageous as it requires only a single transit event to cover the entire wavelength range. However, to identify vibrational modes from condensates at wavelengths longer than $\sim 14\,\mu m$, MRS will be required.

5.3 Impact of clouds

Clouds are now an increasingly important feature in many hot Jupiter atmospheres. We have investigated the broad spectral properties of clouds, using Mie theory and analytic transmission spectral relations.

We investigate the impact of grain size and distributions on condensate absorption spectra finding that the transmission spectrum can be well represented by the largest particle size in the distribution. Additionally, when a strong optical slope is observed in the optical, condensate vibrational mode features become prominent in the infrared associated with clouds composed of small sub-micron sized particles.

Distinguishing cloud composition could in principle help make the distinction between cloud species generated photochemically or through condensation chemistry. We have highlighted spectral features in the infrared generated by the vibrational mode of a condensates major species bond as potential identifiers of cloud compositions in exoplanet atmospheres with the potential for both altitude and wavelength differentiation between species group. While it is difficult with current observations ($<1.7\,\mu m$) to distinguish between different cloud species we find cloud absorption features, caused by the vibrational mode of the major bond species of the condensate, could be present in the infrared, which could help discern different cloud types and constrain particles sizes and altitudes.

The vibrational modes of the various condensates considered in this paper for hot Jupiter atmospheres span a large wavelength regime well into the infrared, with a majority between $9-28\,\mu m$ where current instruments cannot make transmission

measurements.

Of particular interest for this case study is MIRI, JWST's Mid InfraRed Instrument. MIRI has both imaging and spectroscopic capabilities from $5-28.3\,\mu m$ and will have 50 times the sensitivity and seven times the angular resolution of Spitzer, making it a vital instrument for the detection and characterisation of exoplanetary atmospheres as its long wavelength spectral capabilities will be highly sensitive to the cloud properties of transiting exoplanets.

We've done the impossible, and that makes us mighty.

MALCOLM REYNOLDS
Firefly

6 Summary

Exoplanet atmospheres are wildly complex environments. In the last 20 years a whole new realm of astrophysics has emerged focused on exploring the extent of exoplanets in our Galaxy. It is not a surprise that, as in our own solar system, there is a huge diversity of planetary atmospheres beyond the reach of our Sun, orbiting other stars. In the last few decades, hundreds of transiting exoplanets have been discovered with thousands more waiting to be confirmed. Yet only a few have the favourable characteristics needed for detailed atmospheric studies through transmission and emission spectra using current instruments. These planets are extremely valuable, becoming prototypes for the rest of the field. Transmission and emission spectra reveal a plethora of information on these worlds including spin-orbit alignment, temperature, bulk composition, albedo, dynamics, atmospheric structure, and composition. As hot Jupiter atmospheres are dominated by stellar irradiation, knowing in detail both the optical opacities (where the stellar flux gets deposited) and the infrared opacities (where the stellar flux gets absorbed and re-radiated) for these planets is absolutely crucial. Presently, hot Jupiter exoplanet spectra are limited to the optical and near-IR regime below 1.7 µm with intermittent wavelength coverage into the IR with Spitzer. In this work we have investigated the transmission spectral

properties of hot Jupiter exoplanet atmospheres through observations and analytical models to explore the diversity of atmospheres expected.

Firstly, we have looked at the observations currently being obtained with HST/WFC3 and present a new reduction technique to analyse spectroscopic transit data. The treatment of the systematics can have a significant impact on the measured transit parameters. Currently the systematics present in WFC3 spectroscopic data are treated using a number of different techniques taking into account the individual nature of each dataset. However, this makes comparison of exoplanetary transmission spectra difficult. The new technique presented in this thesis corrects for this by using marginalisation as a statistical tool to determine the most relevant systematics affecting the data consistently across multiple planetary datasets, while still allowing for the individual nature of separate transit observations. We apply our marginalisation technique to a set of five hot Jupiter exoplanet transit datasets across two HST large programs from 2011–2012 in two different observing modes: stare mode and spatial scanning. Our five planetary atmospheric transmission spectra each show varying degrees of absorption by H_2O in a distinctive broadband feature centred at 1.4 µm. We confirm the robust detections of H_2O in the atmospheres of HAT-P-1b and WASP-17b with a greater than 5σ and 5.6σ significance respectively, and a muted feature observed in the transmission spectrum of XO-1b which has a best fit amplitude of 34±21% amplitude. We also confirm the presence of a grey cloud-deck in the atmosphere of WASP-31b stretching into the near-IR and obscuring a majority of the expected H_2O absorption feature, which is found to be muted to ∼25±10% of the full amplitude model. Our analysis of the well studied hot Jupiter HD 209458b transmission spectrum from WFC3 indicates a cooler temperature profile than the equilibrium temperature, which is best fit with 1000 K isothermal atmospheric models muted to 27±11%. This does not correspond with the previous reduction by Deming et al. (2013); however, we find that the spectroscopic lightcurves are impacted by shifts in the wavelength solution presenting sub-pixel variations in the spectra over the course of the observation not accounted for in the individual spectral bins. These five planets well represent the diversity being seen across hot Jupiter atmospheres where a dichotomy is emerging between 'clear' and 'cloudy' atmospheres. For all of our planets, barring WASP-17b, we find that the transmission spectra favour cooler planetary-averaged T–P profiles where the limb of the planet at ∼mbar pressure levels is ∼1000 K. WASP-17b, however, favours a much hotter atmospheric model with T = 1750 K which appears to correspond to a more effective redistribution of heat from the dayside to the limb of the planet as seen in it's dayside-averaged T–P pro-

file. In addition, we explore the impact of different reduction techniques on WFC3 spectroscopic observations and assess the validity of the proposed new technique. We find that the marginalisation method used is a robust and consistent method that can be applied simply to multiple datasets, allowing for a true comparative study, as it effectively takes into account the effect of different analysis methods and weights them according to the significance of fit to the data. However, there are still some improvements that can be made to extend this technique, one being the incorporation of the Deming et al. (2013) template spectrum method to account for variations in the wavelength over the course of the observations.

Expanding on the dichotomy of atmospheres being observed through atmospheric transmission spectra, we explore the impact of condensate clouds on the properties of the measured spectra and outline potential observations to be conducted with JWST. Using Mie theory we construct the transmission spectra of a range of condensates expected to form in hot Jupiter atmospheres given their measured optical properties. Each of the condensates considered show similar optical transmission spectral properties following Rayleigh-like scattering into the near-IR. Using current transmission spectral measurements of the hot Jupiter HD 189733b, we find that the observed optical slope representing Rayleigh scattering at high altitudes can constrain the cloud condensate particle size and can be used as a diagnostic for potential condensate features in the IR where almost all condensate absorption features occur. We find that the major transmission spectral absorption features are generated by the vibrational modes of the major diatomic bond pair in each condensate species, which is often seen in the IR at 5–25 µm. Different condensate species containing the same major diatomic bond have similar transmission spectral properties. This wavelength region, however, is currently unavailable for exoplanet transmission studies, as no instrument has the capabilities of observing over this spectral range to the required S/N. In this light we explore the potential for JWST observations over this wavelength range with the mid-IR instrument MIRI. Using the estimated throughput of MRS we determine that high resolution transmission spectra are obtainable for hot Jupiter exoplanets across MIRI's four MRS channels, with the ability to differentiate between the vibrational mode absorption features of multiple condensate species likely to form clouds in the upper atmosphere of these exoplanets.

The work presented here provides the tools needed to further our study of atmospheric transmission spectra and allow for a true comparison to be made between exoplanet atmospheric datasets. The apparent dichotomy of 'clear' and 'cloudy' atmospheres reinforces the need to consider the impact that clouds can have on a exoplanet

atmosphere and their resultant observational properties. The theoretical work presented on the impact of cloud condensates on the transmission spectral properties of an atmosphere is a first step towards targeted observations with JWST.

What's next?

PRESIDENT JED BARTLET
The West Wing

7 Future Work

To make strides toward true comparative exoplanetology, large datasets need to be analyzed against each other. For exoplanet science today, close-in exoplanets with large transit signals serve as fundamental test cases for our understanding of atmospheric physics and chemistry and can help provide clues that shape our understanding of how these processes work in less easily studied smaller and cooler planets.

My research to date has had two main focuses: on one front using observations in the NIR from Hubble Space Telescope's Wide Field Camera 3 (HST WFC3) to measure the water abundance in the atmospheres of hot Jupiter exoplanetary atmospheres, and on the second front using analytical models to compute theoretical transmission spectra for cloud condensate particles over the wavelength range covered by JWST. There are a number of possible avenues for building on my existing work.

7.1 Continued multi-wavelength observations

HST WFC3 transmission spectral observations are rapidly moving down the exoplanet mass scale. I intend to carry out a thorough and consistent analysis across the present

WFC3 exoplanet transit datasets which span hot Jupiters to super-Earths with 500 orbits, resulting in a true comparative study of their atmospheres over the 1.4 µm water band. In addition to this I propose to obtain ground based J, H, K-band observations using facilities like CFHT, which will extend the wavelength coverage in the NIR out to ∼2.4 µm, where absorbers in the optical potentially break down.

7.2 Analytical transmission spectra

I will use the framework outlined in Wakeford & Sing (2015) to expand transmission spectrum models to smaller and cooler worlds, where observations are moving towards Neptunes and super-Earths. I will also expand on this work by applying Mie theory to exoplanet emission spectra. For this I will use the current knowledge from exoplanetary GCMs, such as those developed at CPS, to compute analytical models of emission spectra for various condensate species at a range of grain sizes.

7.3 Preparation for JWST

I will compare observational transmission and emission measurements to the analytical cloud condensate models developed following the framework outlined in Wakeford & Sing (2015). This will be used to better constrain the cloud composition and grain size for the planetary atmospheres producing a robust target list and strategy for JWST observations when the call for proposals is announced in 2017.

Bibliography

Ackerman, A. S., & Marley, M. S. 2001, ApJ, 556, 872

Amundsen, D. S., Baraffe, I., Tremblin, P., et al. 2014, A&A, 564, A59

Andersen, A. C., Mutschke, H., Posch, T., Min, M., & Tamanai, A. 2006, Journal of Quantitative Spectroscopy and Radiative Transfer, 100, 4

Anderson, D., Hellier, C., Gillon, M., et al. 2010, ApJ, 709, 159

Anderson, D. R., Collier Cameron, A., Hellier, C., et al. 2011, A&A, 531, A60

Anderson, M. R. 2000, Master's thesis, University of Missouri-Rolla

Angerhausen, D., DeLarme, E., & Morse, J. A. 2014, ArXiv e-prints, arXiv:1404.4348

Bailey, J. 2014, PASA, 31, 43

Baines, K. H., Hammel, H. B., Rages, K. A., Romani, P. N., & Samuelson, R. E. 1995, in Neptune and Triton, ed. D. P. Cruikshank, M. S. Matthews, & A. M. Schumann, 489–546

Bakos, G. Á., Noyes, R. W., Kovács, G., et al. 2007, ApJ, 656, 552

Bakos, G. Á., Hartman, J., Torres, G., et al. 2011, ApJ, 742, 116

Ballester, G. E., Sing, D. K., & Herbert, F. 2007, Nature, 445, 511

Barman, T. 2007, ApJ Letters, 661, L191

Barstow, J. K., Aigrain, S., Irwin, P. G. J., et al. 2014, ApJ, 786, 154

Batalha, N. M. 2014, Proceedings of the National Academy of Science, 111, 12647

Batsanov, S., & Derbeneva, S. 1969, Journal of Structural Chemistry, 10, 510

Bayliss, D. D., Winn, J. N., Mardling, R. A., & Sackett, P. D. 2010, ApJ Letters, 722, L224

Begemann, B., Henning, T., Mutschke, H., & Dorschner, J. 1995, Planetary and Space Science, 43, 1257

Ben-Jaffel, L. 2007, ApJ Letters, 671, L61

Benneke, B., & Seager, S. 2012, ApJ, 753, 100

Berta, Z. K., Charbonneau, D., Désert, J.-M., et al. 2012, ApJ, 747, 35

Bilger, C., Rimmer, P., & Helling, C. 2013, MNRAS, 435, 1888

Birkby, J., de Kok, R., Brogi, M., et al. 2013, MNRAS Letters, 436, L35

Bohren, C. F., & Huffman, D. R. 1983, Absorption and Scattering of Light by Small Particles, 82

Borucki, W. J., Koch, D. G., Basri, G., Batalha, N., & Kepler Mission Team. 2011, ApJ, 728, 117

Brown, T. M. 2001, ApJ, 553, 1006

Brown, T. M., Charbonneau, D., Gilliland, R. L., Noyes, R. W., & Burrows, A. 2001, ApJ, 552, 699

Burgasser, A. J., Looper, D. L., Kirkpatrick, J. D., Cruz, K. L., & Swift, B. J. 2008, ApJ, 674, 451

Burke, C. J., McCullough, P. R., Bergeron, L. E., et al. 2010, ApJ, 719, 1796

Burrows, A., Hubeny, I., Budaj, J., Knutson, H. A., & Charbonneau, D. 2007, ApJ Letters, 668, L171

Burrows, A., Rauscher, E., Spiegel, D. S., & Menou, K. 2010, ApJ, 719, 341

Burrows, A., & Sharp, C. M. 1999, ApJ, 512, 843

Cáceres, C., Ivanov, V. D., Minniti, D., et al. 2009, A&A, 507, 481

Carlson, B. E., Rossow, W. B., & Orton, G. S. 1988, Journal of Atmospheric Sciences, 45, 2066

Charbonneau, D., Brown, T. M., Latham, D. W., & Mayor, M. 2000, ApJ Letters, 529, L45

Charbonneau, D., Brown, T. M., Noyes, R. W., & Gilliland, R. L. 2002, ApJ, 568, 377

Charbonneau, D., Knutson, H. A., Barman, T., et al. 2008, ApJ, 686, 1341

Charbonneau, D., Allen, L. E., Megeath, S. T., et al. 2005, ApJ, 626, 523

Claret, A. 2000, A&A, 363, 1081

Crossfield, I. J. M., Barman, T., Hansen, B. M. S., & Howard, A. W. 2013, A&A, 559, A33

Crouzet, N., McCullough, P. R., Burke, C., & Long, D. 2012, ApJ, 761, 7

Crouzet, N., McCullough, P. R., Deming, D., & Madhusudhan, N. 2014, ApJ, 795, 166

Cruikshank, D. P., Imanaka, H., & Ore, C. M. D. 2005, Advances in Space Research, 36, 178 , <ce:title>Space Life Sciences: Astrobiology: Steps toward Origin of Life and Titan before Cassini</ce:title>

Cushing, M. C., Roellig, T. L., Marley, M. S., et al. 2006, ApJ, 648, 614

Day, K. L. 1981, ApJ, 246, 110

de Mooij, E. J. W., de Kok, R. J., Nefs, S. V., & Snellen, I. A. G. 2011, A&A, 528, A49

Deming, D., Seager, S., Richardson, L. J., & Harrington, J. 2005, Nature, 434, 740

Deming, D., Wilkins, A., McCullough, P., et al. 2013, ApJ, 774, 95

Désert, J.-M., des Etangs, A. L., Hébrard, G., et al. 2009, ApJ, 699, 478

Diamond-Lowe, H., Stevenson, K. B., Bean, J. L., Line, M. R., & Fortney, J. J. 2014, ApJ, 796, 66

Dorschner, J., Begemann, B., Henning, T., Jaeger, C., & Mutschke, H. 1995, A&A, 300, 503

Draine, B. T. 2003, araa, 41, 241

Dressel, L., Wong, M., Pavlovsky, C., Long, K., et al. 2010, Wide Field Camera 3 Instrument Handbook

Eastman, J., Gaudi, B. S., & Agol, E. 2013, PASP, 125, 83

Ebel, D. S., & Grossman, L. 2000, Geochimica et Cosmochimica Acta, 64, 339

Egan, W. G., & Hilgeman, T. 1975, aj, 80, 587

Ehrenreich, D., Bonfils, X., Lovis, C., et al. 2014, A&A, 570, A89

Evans, D., & Hubbard, W. 1972, Nature, 240, 162

Evans, T. M., Pont, F., Sing, D. K., et al. 2013, ApJ Letters, 772, L16

Fortney, J. J. 2005, MNRAS, 364, 649

Fortney, J. J., Mordasini, C., Nettelmann, N., et al. 2013, ApJ, 775, 80

Fortney, J. J., Shabram, M., Showman, A. P., et al. 2010, ApJ, 709, 1396

Fossati, L., Bagnulo, S., Elmasli, A., et al. 2010, ApJ, 720, 872

Fraine, J., Deming, D., Benneke, B., et al. 2014, Nature, 513, 526

Freedman, R. S., Marley, M. S., & Lodders, K. 2008, ApJ Supplements, 174, 504

Gibson, N. P. 2014, MNRAS, 445, 3401

Gibson, N. P., Aigrain, S., Barstow, J. K., et al. 2013, MNRAS, 436, 2974

Gibson, N. P., Aigrain, S., Roberts, S., et al. 2012, MNRAS, 419, 2683

Gibson, N. P., Pont, F., & Aigrain, S. 2011, MNRAS, 411, 2199

Gibson, N. P., Aigrain, S., Pont, F., et al. 2012, MNRAS, 422, 753

Gillet, P., Guyot, F., Price, G. D., Tournerie, B., & Le Cleach, A. 1993, Physics and Chemistry of Minerals, 20, 159

Glasse, A. C. H., Bauwens, E., Bouwman, J., et al. 2010, in Society of Photo-Optical Instrumentation Engineers (SPIE) Conference Series, Vol. 7731, Society of Photo-Optical Instrumentation Engineers (SPIE) Conference Series

Glassgold, A., & Graham, J. 2008, UC Berkeley - ISM: Lecture 06 - 08

Grillmair, C. J., Charbonneau, D., Burrows, A., et al. 2007, ApJ Letters, 658, L115

Grillmair, C. J., Burrows, A., Charbonneau, D., et al. 2008, Nature, 456, 767

Grossman, L. 1972, Geochimica et Cosmochimica Acta, 36, 597

Han, E., Wang, S. X., Wright, J. T., et al. 2014, PASP, 126, 827

Hansen, J. E., & Travis, L. D. 1974, Space Science Reviews, 16, 527

Haswell, C. A., Fossati, L., Ayres, T., et al. 2012, ApJ, 760, 79

Hayek, W., Sing, D., Pont, F., & Asplund, M. 2012, A&A, 539, A102

Helling, C. 2007, in IAU Symposium, Vol. 239, IAU Symposium, ed. F. Kupka, I. Roxburgh, & K. L. Chan, 224–226

Helling, C. 2008, in Astronomical Society of the Pacific Conference Series, Vol. 398, Extreme Solar Systems, ed. D. Fischer, F. A. Rasio, S. E. Thorsett, & A. Wolszczan, 443

Helling, C. 2009a, in American Institute of Physics Conference Series, Vol. 1094, 15th Cambridge Workshop on Cool Stars, Stellar Systems, and the Sun, ed. E. Stempels, 162–171

Helling, C. 2009b, in Astronomical Society of the Pacific Conference Series, Vol. 414, Cosmic Dust - Near and Far, ed. T. Henning, E. Grün, & J. Steinacker, 125

Heng, K., & Demory, B.-O. 2013, ApJ, 777, 100

Henning, T., Mutschke, H., & Jäger, C. 2005, Proceedings of the International Astronomical Union, 1, 457

Henry, G. W., Marcy, G. W., Butler, R. P., & Vogt, S. S. 2000, ApJ Letters, 529, L41

Holman, M. J., Winn, J. N., Latham, D. W., et al. 2006, ApJ, 652, 1715

Howe, A. R., & Burrows, A. S. 2012, ApJ, 756, 176

Huffman, D. R., & Wild, R. L. 1967, Phys. Rev., 156, 989

Huitson, C. M., Sing, D. K., Vidal-Madjar, A., et al. 2012, MNRAS, 422, 2477

Huitson, C. M., Sing, D. K., Pont, F., et al. 2013, MNRAS, 434, 3252

Jensen, A. G., Redfield, S., Endl, M., et al. 2011, ApJ, 743, 203

Kane, S. R., Ciardi, D. R., Gelino, D. M., & von Braun, K. 2012, MNRAS, 425, 757

Kangarloo, H. 2010a, ICMEE2010, 2nd International Conference

—. 2010b, ICMEE2010, 2nd International Conference

Kataria, T., Showman, A. P., Fortney, J. J., et al. 2015, ApJ, 801, 86

Khare, B., Bakes, E., Cruikshank, D., & McKay, C. 2001, Advances in Space Research, 27, 299

Khare, B., Sagan, C., Arakawa, E., et al. 1984, Icarus, 60, 127

Knutson, H. A., Charbonneau, D., Allen, L. E., Burrows, A., & Megeath, S. T. 2008, ApJ, 673, 526

Knutson, H. A., Charbonneau, D., Noyes, R. W., Brown, T. M., & Gilliland, R. L. 2007a, ApJ, 655, 564

Knutson, H. A., Howard, A. W., & Isaacson, H. 2010, ApJ, 720, 1569

Knutson, H. A., Charbonneau, D., Allen, L. E., et al. 2007b, Nature, 447, 183

Knutson, H. A., Lewis, N., Fortney, J. J., et al. 2012, ApJ, 754, 22

Knutson, H. A., Dragomir, D., Kreidberg, L., et al. 2014, ApJ, 794, 155

Koike, C., Kaito, C., Yamamoto, T., et al. 1995, Icarus, 114, 203

Kreidberg, L., Bean, J. L., Désert, J.-M., et al. 2014a, ApJ Letters, 793, L27

—. 2014b, Nature, 505, 69

Kröger, F., & Meyer, H. 1954, Physica, 20, 1149

Kuntschner, H., Bushouse, H., Kümmel, M., & Walsh, J. 2009, WFC3 SMOV proposal 11552: Calibration of the G141 grism, Tech. rep., MAST

Lecavelier des Etangs, A., Pont, F., Vidal-Madjar, A., & Sing, D. 2008, A&A, 481, L83

Lee, J.-M., Irwin, P. G. J., Fletcher, L. N., Heng, K., & Barstow, J. K. 2014, ApJ, 789, 14

Lehnert, N., Neese, F., Ho, R. Y., Que, L., & Solomon, E. I. 2002, Journal of the American Chemical Society, 124, 10810

Lewis, N. K., Showman, A. P., Fortney, J. J., et al. 2010, ApJ, 720, 344

Li, A., & Draine, B. T. 2001, ApJ Letters, 550, L213

—. 2002, ApJ, 564, 803

Liang, M.-C., Seager, S., Parkinson, C. D., Lee, A. Y.-T., & Yung, Y. L. 2004, ApJ Letters, 605, L61

Line, M. R., Knutson, H., Deming, D., Wilkins, A., & Desert, J.-M. 2013, ApJ, 778, 183

Linsky, J. L., Yang, H., France, K., et al. 2010, ApJ, 717, 1291

Liou, K.-N. 2002, An introduction to atmospheric radiation, Vol. 84 (Academic press)

Lodders, K. 1999, ApJ, 519, 793

Lodders, K. 2002, ApJ, 577, 974

Lodders, K. 2003, ApJ, 591, 1220

Lodders, K. 2010, Exoplanet Chemistry, ed. R. Barnes, 157

Lodders, K., & Fegley, B. 2002, ICARUS, 155, 393

Lodders, K., & Fegley, Jr. B. edited by Mason, J. W. 2006, Chemistry of Low Mass Substellar Objects (Springer Praxis), 1

Lodders, K., & Fegley Jr, B. 2006, in Astrophysics Update 2 (Springer), 1–28

M. Meinecke, B. P. 2005, Database of Optical Constants for Cosmic Dust

Machalek, P., McCullough, P. R., Burke, C. J., et al. 2008, ApJ, 684, 1427

Madhusudhan, N. 2012, ApJ, 758, 36

Madhusudhan, N., & Seager, S. 2009, ApJ, 707, 24

—. 2010, ApJ, 725, 261

Madhusudhan, N., Harrington, J., Stevenson, K. B., et al. 2011, Nature, 469, 64

Mandel, K., & Agol, E. 2002, ApJ Letters, 580, L171

Mandell, A. M., Haynes, K., Sinukoff, E., et al. 2013, ApJ, 779, 128

Marley, M. S., Ackerman, A. S., Cuzzi, J. N., & Kitzmann, D. 2013, Clouds and Hazes in Exoplanet Atmospheres, ed. S. J. Mackwell, A. A. Simon-Miller, J. W. Harder, & M. A. Bullock, 367–391

Marley, M. S., Fortney, J., Seager, S., & Barman, T. 2007, Protostars and Planets V, 733

Marley, M. S., & McKay, C. P. 1999, Icarus, 138, 268

Marois, C., Macintosh, B., Barman, T., et al. 2008, Science, 322, 1348

Marois, C., Zuckerman, B., Konopacky, Q. M., Macintosh, B., & Barman, T. 2010, Nature, 468, 1080

Martonchik, J. V., & Orton, G. S. 1994, Applied optics, 33, 8306

Mayor, M., & Queloz, D. 1995, Nature, 378, 355

Mazeh, T., Naef, D., Torres, G., et al. 2000, ApJ Letters, 532, L55

McCullough, P. 2011, WFC Space Telescope Analysis Newsletter 6

McCullough, P. R., Crouzet, N., Deming, D., & Madhusudhan, N. 2014, ApJ, 791, 55

McCullough, P. R., Stys, J. E., Valenti, J. A., et al. 2006, ApJ, 648, 1228

McQuillan, A., Mazeh, T., & Aigrain, S. 2013, ApJ Letters, 775, L11

Morley, C. V., Fortney, J. J., Kempton, E. M.-R., et al. 2013, ApJ, 775, 33

Morley, C. V., Fortney, J. J., Marley, M. S., et al. 2012, ApJ, 756, 172

Morley, C. V., Marley, M. S., Fortney, J. J., et al. 2014, ApJ, 787, 78

Moses, J., Madhusudhan, N., Visscher, C., & Freedman, R. 2013a, ApJ, 763, 25

Moses, J. I., Madhusudhan, N., Visscher, C., & Freedman, R. S. 2013b, ApJ, 763, 25

Narita, N., Suto, Y., Winn, J. N., et al. 2005, PASJ, 57, 471

Nascimbeni, V., Piotto, G., Pagano, I., et al. 2013, A&A, 559, A32

Nikolov, N., Sing, D. K., Pont, F., et al. 2014, MNRAS, 437, 46

Nikolov, N., Sing, D. K., Burrows, A. S., et al. 2015, MNRAS, 447, 463

Nixon, C., Achterberg, R., Romani, P., et al. 2010, Planetary and Space Science, 58, 1667 , surfaces and atmospheres of the outer planets, their satellites and ring systems: Part {VI}

Palik, E. D. 1998, Handbook of Optical Constants of Solids: Index, Vol. 3 (Access Online via Elsevier)

Parmentier, V., Showman, A. P., & Lian, Y. 2013, A&A, 558, A91

Perez-Becker, D., & Showman, A. P. 2013, ApJ, 776, 134

Pollacco, D. L., Skillen, I., Collier Cameron, A., et al. 2006, PASP, 118, 1407

Pont, F., Knutson, H., Gilliland, R. L., Moutou, C., & Charbonneau, D. 2008, MNRAS, 385, 109

Pont, F., Sing, D. K., Gibson, N. P., et al. 2013, MNRAS, 432, 2917

Pont, F., Gilliland, R. L., Moutou, C., et al. 2007, A&A, 476, 1347

Posch, T., Kerschbaum, F., Fabian, D., et al. 2003, ApJ Supplements, 149, 437

Queloz, D., Eggenberger, A., Mayor, M., et al. 2000, A&A, 359, L13

Querry, M. 1987, Optical constants of minerals and other materials from the millimetre to the ultraviolet, Tech. rep., Chemical Research, Development and Engineering Center, U.S. Army Armament Munitions Chemical Command

Ramirez, S., Coll, P., da Silva, A., et al. 2002, Icarus, 156, 515

Ranjan, S., Charbonneau, D., Désert, J.-M., et al. 2014, ApJ, 785, 148

Rauscher, E., & Menou, K. 2012, ApJ, 750, 96

Redfield, S., Endl, M., Cochran, W. D., & Koesterke, L. 2008, ApJ Letters, 673, L87

Rice, S. A., & Klemperer, W. 2004, The Journal of Chemical Physics, 27, 573

Rogers, J. C., Apai, D., López-Morales, M., Sing, D. K., & Burrows, A. 2009, ApJ, 707, 1707

Rothman, L. S., Gordon, I. E., & et al. 2009, JQSRT, 110, 533

Rowe, J. F., Matthews, J. M., Seager, S., et al. 2008, ApJ, 689, 1345

Sánchez-Lavega, A., Pérez-Hoyos, S., & Hueso, R. 2004, American Journal of Physics, 72, 767

Saniger, J. 1995, Materials Letters, 22, 109

Seager, S. 2010, Exoplanet atmospheres: physical processes (Princeton University Press)

Seager, S., & Deming, D. 2010, araa, 48, 631

Seager, S., Richardson, L. J., Hansen, B. M. S., et al. 2005, ApJ, 632, 1122

Seager, S., & Sasselov, D. D. 2000, ApJ, 537, 916

Sharp, C. M., & Burrows, A. 2007, ApJ Supplements, 168, 140

Showman, A. P., Cooper, C. S., Fortney, J. J., & Marley, M. S. 2008, ApJ, 682, 559

Showman, A. P., Fortney, J. J., Lian, Y., et al. 2009, ApJ, 699, 564

Showman, A. P., & Polvani, L. M. 2011, ApJ, 738, 71

Sing, D. K. 2010, A&A, 510, A21

Sing, D. K., Désert, J.-M., Lecavelier Des Etangs, A., et al. 2009, A&A, 505, 891

Sing, D. K., Vidal-Madjar, A., Désert, J.-M., Lecavelier des Etangs, A., & Ballester, G. 2008, ApJ, 686, 658

Sing, D. K., Désert, J.-M., Fortney, J. J., et al. 2011a, A&A, 527, A73

Sing, D. K., Pont, F., Aigrain, S., et al. 2011b, MNRAS, 416, 1443

Sing, D. K., Lecavelier des Etangs, A., Fortney, J. J., et al. 2013, MNRAS, 436, 2956

Sing, D. K., Wakeford, H. R., Showman, A. P., et al. 2015, MNRAS, 446, 2428

Snellen, I. A. G., Albrecht, S., de Mooij, E. J. W., & Le Poole, R. S. 2008, A&A, 487, 357

Snellen, I. A. G., de Kok, R. J., de Mooij, E. J. W., & Albrecht, S. 2010, Nature, 465, 1049

Southworth, J. 2010, MNRAS, 408, 1689

Southworth, J., Hinse, T., Dominik, M., et al. 2012, MNRAS, 426, 1338

Stevenson, K. B., Bean, J. L., Fabrycky, D., & Kreidberg, L. 2014a, ApJ, 796, 32

Stevenson, K. B., Bean, J. L., Seifahrt, A., et al. 2014b, aj, 147, 161

Stevenson, K. B., Désert, J.-M., Line, M. R., et al. 2014c, Science, 346, 838

Sudarsky, D., Burrows, A., & Hubeny, I. 2003, ApJ, 588, 1121

Sudarsky, D., Burrows, A., & Pinto, P. 2000, ApJ, 538, 885

Swain, M., Deroo, P., Tinetti, G., et al. 2013, ICARUS, 225, 432

Swain, M. R., Vasisht, G., & Tinetti, G. 2008, Nature, 452, 329

Swain, M. R., Tinetti, G., Vasisht, G., et al. 2009b, ApJ, 704, 1616

Tinetti, G., Deroo, P., Swain, M. R., et al. 2010, ApJ Letters, 712, L139

Tinetti, G., Vidal-Madjar, A., Liang, M.-C., et al. 2007, Nature, 448, 169

Todorov, K., Deming, D., Harrington, J., et al. 2010, ApJ, 708, 498

Todorov, K. O., Deming, D., Burrows, A., & Grillmair, C. J. 2014, ApJ, 796, 100

Torres, G., Winn, J. N., & Holman, M. J. 2008, ApJ, 677, 1324

Tremblin, P., Amundsen, D. S., Mourier, P., et al. 2015, submitted, ApJ Letters

Triaud, A. H. M. J., Collier Cameron, A., Queloz, D., et al. 2010, A&A, 524, A25

Vidal-Madjar, A., Lecavelier des Etangs, A., Désert, J.-M., et al. 2003, Nature, 422, 143

Vidal-Madjar, A., Désert, J.-M., des Etangs, A. L., et al. 2004, ApJ Letters, 604, L69

Vidal-Madjar, A., Sing, D., Lecavelier Des Etangs, A., et al. 2011, A&A, 527

Visscher, C., Lodders, K., & Fegley, Jr., B. 2006, ApJ, 648, 1181

—. 2010, ApJ, 716, 1060

Wakeford, H., Sing, D., Deming, D., et al. 2013, MNRAS, 435, 3481

Wakeford, H. R., & Sing, D. K. 2015, A&A, 573, A122

Waldmann, I., Tinetti, G., Drossart, P., et al. 2012, ApJ, 744, 35

Waldmann, I. P., Tinetti, G., Deroo, P., et al. 2013, ApJ, 766, 7

Wood, P. L., Maxted, P. F., Smalley, B., & Iro, N. 2011, MNRAS, 412, 2376

Yaqoob, T. 2011, Exoplanets and Alien Solar Systems (New Earth Labs)

Yurchenko, S. N., & Tennyson, J. 2014, MNRAS, 440, 1649

Zahnle, K., Marley, M. S., Freedman, R. S., Lodders, K., & Fortney, J. J. 2009, ApJ Letters, 701, L20

Zeidler, S., Posch, T., Mutschke, H., Richter, H., & Wehrhan, O. 2011, A&A, 526, A68

Zhou, G., & Bayliss, D. D. R. 2012, MNRAS, 426, 2483